NASA CR-169,441

NASA-CR-169441
19830002533

A Reproduced Copy

OF

NASA CR-169, 441

Reproduced for NASA

by the

NASA Scientific and Technical Information Facility

November 1981

TAE No. 470

(NASA-CR-169441) PREDICTOR SYMBOLOGY IN COMPUTER-GENERATED PICTORIAL DISPLAYS Final Report (Technion - Israel Inst. of Tech.) 121 p HC A06/MF A01 CSCL 09B
N83-10803
Unclas
G3/61 15247

Predictor Symbology
in Computer-Generated
Pictorial Displays

by

Arthur J. Grunwald

N83-10803#

TAE No. 470

November 1981

PREDICTOR SYMBOLOGY IN COMPUTER-GENERATED PICTORIAL DISPLAYS

by

Arthur J. Grunwald

This is the final report of a research study entitled: "Analytical and Experimental Evaluation of Superimposed Predictor Symbology for Computer-Generated Real-World Displays", sponsored by the National Aeronautics and Space Administration under contract No. NASW-3302.

Contract Technical Director:
Samuel A. Morello,
Assistant Chief Flight Management Branch
Code 3610 - M.S. 246 B

Langley Research Center
Hampton, Va. 23665

ABSTRACT

The purpose of this study is the development and experimental simulator evaluation of superimposed predictor symbology in computer-generated pictorial displays. The display under investigation, is a tunnel display for the four-dimensional commercial aircraft approach-to-landing under instrument flight rules. It is investigated whether more complex predictive information such as a three-dimensional perspective vehicle symbol, predicting the future vehicle position as well as future vehicle attitude angles, contributes to a better system response, and suitable predictor laws for the predictor motions, are formulated. Methods for utilizing the predictor symbol in controlling the forward velocity of the aircraft in four-dimensional approaches,are investigated.

The simulator tests show, that the complex perspective vehicle symbol yields improved damping in the lateral response as compared to a flat two-dimensional predictor cross, but yields generally larger vertical deviations. Methods of using the predictor symbol in controlling the forward velocity of the vehicle are shown to be effective. The tunnel display with superimposed perspective vehicle symbol yields very satisfactory results and pilot acceptance in the lateral control but is found to be unsatisfactory in the vertical control, as a result of too large vertical path-angle deviations.

The research is carried out in the framework of the Terminal Configured Vehicle (TCV) program at Langley Research Center, Hampton, Va., as part of an ongoing research on integrated advanced display concepts for the future commercial aircraft flight-deck. The development and quantitative simulator

evaluation of the predictive information, has been carried out at the Flight Control Laboratory of the Technion - Haifa, Israel. In parallel, all developments are implemented in the tunnel display software package at Langley Research Center, for operation in the TCV research cockpit, and in a later stage, for operation in the TCV B-737 research aircraft. At Langley Research Center, a qualitative simulator evaluation has been carried out.

TABLE OF CONTENTS

TABLE OF CONTENTS (Cont'd)

LIST OF FIGURES

LIST OF FIGURES (Cont'd)

LIST OF FIGURES (Cont'd)

LIST OF TABLES

LIST OF SYMBOLS

A	System matrix
a_ℓ, a_v	inertial accelerations of vehicle perpendicular to vehicle path in locally level and in locally vertical plane, respectively, ft/sec^2
$a^i_{x_b}, a^i_{y_b}, a^i_{z_b}$	inertial accelerations of vehicle along x_b-axis, y_b-axis, and z_b-axis, respectively, ft/sec^2
$a^m_{x_b}, a^m_{y_b}, a^m_{z_b}$	accelerations measured by sensors along x_b-axis, y_b-axis and z_b-axis, respectively, ft/sec^2
a_x	forward acceleration of vehicle, due to engine thrust, ft/sec^2
a_1, a_2	break-frequencies of control input and gust disturbance spectra, respectively, rad/sec
B	control input matrix
b	half the diagonal of perspective vehicle symbol fuselage, ft
col [ ]	column vector
cov (x)	auto-covariance of $x(t)$
D, D_0	actual and nominal predictor distance, ft
$E_{a \to b}$	Euler matrix for rotational transformation from system a to system b, where a and b can be i, b, e or p
g	acceleration due to gravity, ft/sec^2
I	identity matrix
I_{xx}, I_{yy}, I_{zz}	vehicle moments of inertia about x_b-axis, y_b-axis, and z_b-axis, respectively, slug-ft^2
J_{xz}	vehicle product of inertia in $x_b z_b$ plane, slug-ft^2

LIST OF SYMBOLS (Cont'd)

L, M, N	total rolling, pitching and yawing moments about center of gravity of vehicle, lbs-ft
m	vehicle mass, slug
P_i	partition matrix i
P, Q, R	total vehicle angular velocity about x_b-axis, y_b-axis, and z_b-axis, respectively, rad/sec
p, q, r	perturbed vehicle angular velocity about x_b-axis, y_b-axis, and z_b-axis, respectively, rad/sec
p_g	roll gust disturbance input, respectively, rad/sec
r_w	wash-out filter state of yaw-rate on rudder feedback, rad/sec
$\text{row}_n[A]$	n-th row of matrix A
S	travelled distance of vehicle, ft
s	Laplace operator
sc ( )	deviation score for entry maneuvers, ft
T	prediction time for lateral/vertical control, sec
T_v	prediction time for velocity control, sec
$T_{s\ell}, T_{sv}$	lateral or vertical settling time, sec
t	time
U_b, V_b, W_b	components of $\vec{V}$ along x_b-axis, y_b-axis, and z_b-axis, respectively, ft/sec
U_0, V_0, W_0	nominal trim value of U_b, V_b and W_b, respectively, ft/sec
u, v, w	perturbed values of U_b, V_b and W_b respectively, ft/sec

LIST OF SYMBOLS (cont'd)

u_g, v_g, w_g	gust disturbance inputs in x_b-axis, y_b-axis, and z_b-axis direction, respectively, ft/sec
$\underline{u}$	vector of control inputs
$\underline{v}_g$	vector of lateral gust disturbance inputs
$\vec{V}, V$	vehicle velocity vector and magnitude, ft/sec
V_0	commanded vehicle velocity
W	disturbance input matrix
X, Y, Z	total external forces, acting on vehicle along x_b-axis, y_b-axis, and z_b-axis, respectively, lbs
x_b, y_b, z_b	orthogonal body-axis coordinate system, with x_b-axis pointing towards front of vehicle, y_b-axis, pointing to right, and z_b-axis pointing downwards
x_i, y_i, z_i	orthogonal inertial coordinate system, with x_i-axis pointing to north, y_i-axis to east and z_i-axis downwards
x_e, y_e, z_e	orthogonal eye-coordinate system, with eye at origin and x_e-axis pointing forward away from observer, y_e-axis pointing to right and z_e-axis pointing upward (aligned with body coordinate system)
x_p, y_p, z_p	orthogonal object coordinate system, with x_p-axis pointing forward y_p-axis pointing to right and z_p-axis pointing upward
$\underline{x}$	state vector
y_d, z_d	lateral or vertical deviation from trajectory, ft
y_{d_p}, z_{d_p}	lateral or vertical predicted deviation from trajectory, ft

LIST OF SYMBOLS (Cont'd)

β	vehicle sideslip angle
Γ, Λ, Ξ	first, second and third integral of transition matrix, respectively
$\Delta y_d, \Delta \chi$	additions to basic predictor law for lateral deviation and path angle, respectively
$\delta_{a_s}, \delta_{r_s}, \delta_{e_s}$	aeleron, rudder and elevator deflection, respectively, rad
δ_{th_s}	specific engine thrust variation due to throttle displacement, ft/sec^2
δ_a, δ_e	lateral or vertical control commands, rad
δ_{th}	manual throttle displacement in units of specific engine thrust, ft/sec^2
ε	control error
ζ	damping ratio
λ_ℓ, λ_v	lateral or vertical displacement of vehicle symbol on screen, in screen coordinates
ν	arc of circular path, between present and predicted vehicle position, rad
τ	time shift
τ_{d_1}, τ_{d_2}	time-constants of decay for predicted control and disturbance inputs, respectively, sec
Φ	transition matrix
$\Phi_{ii}(s)$	spectral density of process i
χ, ξ	lateral or vertical path angle, rad

LIST OF SYMBOLS (Cont'd)

ψ,θ,φ	yaw, pitch and roll attitude angles, rad
ω_n	natural frequency, rad/sec

SUBSCRIPTS:

ℓ,v	lateral or vertical
p	predicted
b,i,e,p	body, inertial, eye and object coordinate system, respectively

SUPERSCRIPTS:

T	transpose
$*$, $**$	matrix generated with A^* and A^{**} respectively, see Eqs. (A.79) and (A.80)

STABILITY DERIVATIVE NOTATION:

$B_A = \frac{1}{C}\frac{\partial B}{\partial A}\Big|_{\text{trim}}$ where B can be X,Y,Z,L,M,N, and A can be u,v,w,p,q,r,δ_a, $\delta_r,\delta_e,\delta_{th}$, and C is m for X,Y, and Z; C is I_{xx} for L, C is I_{yy} for M, and C is I_{zz} for N.

I. INTRODUCTION

Computer-generated pictorial displays facilitate the integration of control information in a format, analog to the through-the-windshield visual field. The tunnel display, in which the three-dimensional approach path is displayed perspectively as a winding and descending "tunnel-in-the-sky" is useful in particular for following complicated curved trajectories. In previous work [1], (1980), the tunnel display was successfully implemented to the steep and curved helicopter approach-to-landing under instrument flight rules. It is shown in Ref. [1] that pictorial displays, without further augmentation, yield impaired system damping due to the lack of peripheral visual cues. It is also shown, that superimposed predictor symbology furnishes the system with the necessary damping cues.

This research deals with the implementation of the tunnel display to the fixed-wing commercial aircraft approach-to-landing and with the exploration and development of more complex predictive information. In a curved approach, the trajectory curvature constitutes the main forcing function to the pilot/vehicle system and is responsible for a large part of the pilot activity. The predictive information serves the pilot in coping with this forcing function. Two predictor laws are considered: (1) a non-linear, basic predictor law, based on a circular future vehicle path which is formulated such that it enables following steady curves of the trajectory with zero steady-state error in the lateral deviation and (2) a linear, more sophisticated full-state predictor law which provides a more accurate prediction but yields a steady-state error in steady curves. A linear/non-linear predictor law is formulated which combines both the advantage of a zero steady-state error given by the basic predictor law, with the advantage of a more accurate prediction given by the full-state predictor law.

In addition to the future vehicle position, displayed by a flat two-dimensional predictor cross, the three dimensional perspective vehicle symbol also displays the future vehicle attitude angles. Since the intercept angle between the vehicle and tunnel trajectory is equivalent with the rate of deviation from the trajectory, the display of the future attitude angle is expected to contribute to the system damping.

In addition to providing the necessary damping cues, the perspective vehicle symbol is utilized in controlling the forward velocity of the aircraft in four-dimensional approaches. This is accomplished by using the changes in predictor distance, resulting from changes in forward velocity as a control cue. The advantage of using the perspective vehicle symbol for controlling the forward velocity is that all control information, necessary for lateral, vertical and velocity control remains concentrated in the central area of the display.

II. DESCRIPTION OF THE DISPLAY

Tunnel with Perspective Vehicle Symbol

The basic tunnel display configuration for the 4-D approach-to-landing, is shown in Fig. 1. The winding and descending three-dimensional approach path is presented to the pilot as a tunnel-in-the-sky, which is inertially fixed in space. In order to follow the desired approach path, the pilot must keep the vehicle inside the tunnel. The image shown in Fig. 1 is analog to the "through-the-windshield" visual field and shows the horizon (a) and the tunnel image with cornerlines (b). The tunnel cross-section is constant and square and of 300 ft width and remains at all time upright with respect to inertial space and thus parallel to the horizon. Analog to the natural visual field, a left bank is visualized by a clockwise rotation of the image about the monitor center and a nose-up pitch motion is visualized by a vertical downwards displacement of the image, perpendicular to the horizon.

Basically, the square tunnel elements are drawn at 200 ft intervals. However, to prevent clutter, all elements are omitted in this configuration, and only the interconnecting cornerlines are shown. These lines are of 200 ft length and the points at whch these lines are connected, appear as bright spots. While moving through the tunnel these spots highly contribute to the impression of forward motion.

Superimposed on the tunnel image is the perspective vehicle symbol (c). The center of gravity of the vehicle symbol indicates the predicted vehicle location, τ seconds in advance, and the angular orientation of the symbol indicates the predicted attitude angles of the vehicle. This predictor symbol is located at a distance D ahead of the vehicle, where D is predicted from the actual vehicle velocity, vehicle states and control inputs, T seconds in the future. The wing-span of the vehicle symbol is identical to the tunnel width, i.e. 300 ft., which is about three times as large as the wing-span of the actual aircraft. The bars (d) are positioned on the vertical axis of the vehicle symbol, and serve as a vertical reference. The distance between these bars is identical to the height of the square, i.e. 300 ft. In contrast to the tunnel image, the vehicle symbol is not a "wire-frame" structure. A wire-frame symbol, in which all lines are visible, is ambiguous and can equally well be interpreted as pointing towards the observer, as well as away from the observer. An unambiguous vehicle symbol is obtained by removing the "hidden lines" from the vehicle symbol fuselage. An efficient technique for removing the hidden lines is given in the appendix.

The four corner "tick-marks" (e) indicate a cross-section of the tunnel, which moves along, ahead of the vehicle, at the same distance D as the predictor symbol. The solid square (f) is a cross-section of the tunnel as well but is positioned at distance $D_0 = T/V_0$ ahead, where V_0 is the desired velocity. Since the solid square corresponds to the desired velocity and the corner tick-marks to the actual velocity, the velocity of the vehicle in 4-D approaches is controlled by matching the tick-marks to the solid square. In addition, an increase in velocity and thus an increase in predictor distance, manifests as an apparent thrinking in size of the predictor symbol and a decrease in velocity manifests as an apparent growing in size of the predictor symbol. In order to augment the difference between the tick-marks and the solid square, the tick-marks are drawn at three times the intensity of the solid square. Furthermore, the tick-marks are blinked at a 3 Hz frequency, when the velocity error exceeds a 5 ft/sec threshold.

A digital read-out of the vehicle velocity (g) is displayed in the bottom center of the display. In Fig. 2 a-c this display configuration is shown for $D_0 = 900$, $D_0 = 1500$ and $D_0 = 2000$ ft.

Tunnel with Two-Dimensional Predictor Cross.

The tunnel display with a flat two-dimensional predictor cross is shown in Fig. 3 a-c for three nominal predictor distances. The height and width of the cross are identical to the tunnel square, i.e. 300 ft. The center of the cross is identical with the center of gravity of the perspective vehicle symbol. However, in contrast to the perspective symbol, the predictor cross remains at all times upright with respect to the display and thus does not display the future attitude angles of the vehicle.

Roll-Stabilized Tunnel

In Fig. 4 the roll-stabilized tunnel display is shown. In contrast to the roll-version of the display, the horizon and tunnel image remain at all times level on the display and the roll-motion is visualized by banking the vehicle symbol. A disadvantage of this configuration is that the vehicle symbol displays the predicted bank-angle rather than the actual bank-angle. The bank-angle information is correct in the steady state only, since then the predicted and actual bank-angle are identical.

Banked Tunnel

In Fig. 5 a configuration of the roll-stabilized tunnel display is shown, in which the tunnel elements are banked in curves. The trajectory bank-angle corresponds to the bank-angle which is required in a coordinated turn at the desired vehicle velocity. Thus, the trajectory bank-angle provides a bank-angle command. Both in level flight, as well as in a steady turn, the actual bank-angle will be identical to the commanded trajectory bank-angle and the wings of the perspective vehicle symbol, will be parallel to the base of the tunnel square.

In Fig. 6 the roll-version of the banked tunnel is shown. In a steady turn both the wings of the vehicle symbol as well as the square will be parallel to the base of the monitor. In this situation, the inclined horizon provides the only actual bank-angle information.

In Fig. 7 the roll-version of the banked tunnel is shown for a tunnel width of 450 ft. The perspective vehicle symbol and tunnel cross-section are enlarged accordingly.

III. EXPERIMENTAL EVALUATION

A. OBJECTIVES OF THE EXPERIMENTAL PROGRAM

The objectives of the experimental program are:

(1) To compare the performance of the tunnel display with a 3-D perspective vehicle symbol with the one with a flat 2-D predictor cross.

(2) To evaluate the use of the perspective vehicle symbol with velocity tick-marks for controlling the velocity of the aircraft.

(3) To evaluate a more complex full-state predictor law.

(4) To investigate the effect of the tunnel width.

(5) To evaluate the effect of displaying the commanded bank-angle by banking the tunnel elements in curves.

(6) To compare the roll-version with roll-stabilized version.

B. EXPERIMENTAL SYSTEM

The experimental program was carried out at the Flight-Control Laboratory of the Technion, Haifa, Israel. During the summer of 1981 all developments were implemented in the tunnel software package at Langley Research Center, Hampton, Virginia, for operation in the Terminal Configured Vehicle (TCV) research cockpit. At Langley Research Center preliminary qualitative simulator tests were carried out.

A functional diagram of the experimental system at the Technion is shown in Fig. 8. The vehicle response was computed in two parts: Linear computations, such as velocities and angular rates in the body coordinate system, were carried out by analog simulation, and non-linear computations, such as transformations from body to intertial system as well as the computation of the vehicle path were carried out digitally. Two EAI-580 hybrid-analog computers served for simulating the linear part of the lateral and vertical dynamics, disturbance input shaping, as well as simulating engine dynamics, servo-actuators and stability augmentation system. Analog random processes for the distrubance inputs, were generated by a Hewlett-Packard HOI-3722-A noise generator. The analog signals were converted to digital by a RTP 7431/30 analog-to-digital converter. All the digital computations were performed by a Data General Corporation Eclipse computer with a 16-bit word length and 128-K extended memory. Vehicle path computations were performed in floating point with 32-bit precision. The integration timing was controlled by a real-time clock, and the analog system was fully slaved to the digital system. About 80% of the Eclipse Central Processing Unit (CPU) capability was devoted to the generation of the images of the various display configurations. Optimised, special programming techniques were developed, based on efficient assembly written subroutines, using 16-bit fixed point arithmatics, for obtaining a sufficiently fast update rate. The generated images, digitally coded in a sequence of move/draw commands, were translated into analog voltages by a Hewlett Packard HP-1350A graphics translator, for drawing the stroke-written image on a Hewlett Packard HP-1310A cathode ray tube, with electrostatic deflection system measuring 19 in. diagonally. Vehicle motions, thus presented to the pilot, were utilized in generating the control commands which, in their turn, were imparted to the analog computers.

Control manipulators consisted of a two-axis spring-loaded control stick and an unloaded throttle control lever. The range of the two-axis control stick was from +2 to -2 cm and the maximum spring torque was 0.3 Nm, for both axes. A forward stick displacement created a pitch motion and a lateral stick displacement a roll motion. Rudder pedals were not present and turn coordination was carried out by the stability augmentation system. The range of the throttle control lever was from +8 to -8 cm.

Recorded time-histories of vehicle motions, control commands and disturbances were recorded on-line in extended memory of the CPU, and memorized after each run on a 100 megabyte magnetic disk. The memorized time-histories were retrieved off-line for further reduction. Condensed results, such as run averages and scores were tabulated and printed on a line-printer; time-histories and graphs, were plotted on the CRT screen and photographed for documentation. All condensed results were permanently stored on magnetic tape.

C. DESCRIPTION OF THE EXPERIMENTS

The experiments were concerned with the approach-to-landing in the range from 30,000 to 1,000 ft from the touch-down point. A plan view of the desired trajectory is shown in Fig. 9 and the vertical descent profile along the trajectory is shown in Fig. 10. The commanded velocity V_0 was set at 243.6 ft/sec over the complete approach path. A description of the two types of experiments that were conducted is given hereafter.

1. Trajectory following in the presence of random lateral and vertical gust disturbances; The subjects were instructed to minimize the lateral and vertical deviations from the trajectory with minimum control effort. Each run started from initial location 7 with an initial lateral deviation of 200 ft to the left

of the trajectory, a vertical deviation of 100 ft below the trajectory and zero intercept angle. Thus, control action was required from the subject, immediately after starting the simulation run, to bring the vehicle back on the trajectory. The lateral gust disturbance components v_g and p_g and the longitudinal gust disturbance components u_g and w_g were generated by passing band-limited white noise with a band-limit of 1.5 Hz, through first-order shaping filters. The RMS value of v_g was 13.5 ft/sec, of p_g 0.086 rad/sec, of u_g was 9.0 ft/sec and of w_g was 12.2 ft/sec, and the break frequency of all shaping filters was 0.2 rad/sec.

Each run lasted 128 seconds, during which the means and auto-covariances of deviations, state variables and control commands, were computed.

2. Entering the trajectory from a random chosen, unknown location outside the trajectory: The experiment attempted to simulate a sudden confrontation with the situation of being located outside the trajectory. The subjects were instructed to bring the vehicle back on the desired trajectory, as fast as possible, as smooth as possible and with minimum control effort. Gust disturbances were not present in this experiment. In order to prevent the subject from knowing his initial position before the start of a simulation run, the display was initially blanked and was made visible only immediately after starting the simulation run.

Each run started randomly from one of the 6 initial locations shown in Fig. 9. For all locations the initial lateral deviation was 2,000 ft to the left or to the righ of the trajectory and the initial vertical deviation was 300 ft above or below the trajectory. The initial intercept angle was set between 0 and 60 degrees.

Each entry run lasted 38.4 seconds during which the following performance scores were computed. 1. The lateral settling time $T_{s\ell}$ defined as the time from the start of the run to the moment the lateral deviation settles within a ±100 ft settling tolerance about the desired trajectory and the vertical settling time T_{sv}, for which the settling tolerance is ±75 ft. 2. The means and auto-convariances of deviations, state variables and control commands. 3. The lateral deviation score, defined as the averaged absolute value of the lateral deviation, computed between $t = T_1$ and $t = T_2$, where $T_1 = 10$ sec and $T_2 = 38.4$ sec, according to:

$$sc(y_d) = \frac{1}{(T_2-T_1)} \int_{t_1=T_1}^{T_2} |y_d| dt \qquad (1)$$

The vertical deviation score was computed in the same way as the lateral one. The lateral and vertical deviation scores were chosen to be averaged absolute values rather than averaged squared values, in order to prevent these scores from being dominated by the large initial deviation. For the same reason the averaging process only started at $t = T_1$ sec. T_1 is chosen to be about 25% less than the best possible settling time.

D. RESULTS

Four subjects participated in the experimental program. Apart from subject A, all subjects were male. Subjects A, C and D were Aeronautical Engineering students with no prior flight or simulator training, and subject B an Aeronautical Engineer with extensive simulator experience. Each subject participated in 2-3 2-hours/week simulator sessions. All subjects reached a stable well-trained level after 6 weeks of training. Subject motivation was largely enhanced by using a reward system, based on a general performance score, which was displayed to the subject at the end of each run. This score was composed of the weighted sum of mean-squared deviations and control commands. The reward, given in the form of extra pay, was determined by the performance level which was reached and maintained during the session.

The results of the four subjects are treated separately and are summarized in Tables I-V. The results for each experimental condition represents the average and standard deviation of a set of six or more repetitions.

D.1 Results of Trajectory Following

Comparison of the 3-D perspective vehicle symbol with flat 2-D predictor cross.

The lateral results of the four subjects are shown in Figs. 11-14. Both for the perspective vehicle symbol, as well as for the predictor cross, the lateral deviation was found to increase strongly with the predictor distance *D*, whereas the roll activity and lateral stick activity were found to decrease strongly. The contribution of the perspective vehicle symbol was found in particular in the significantly lower roll-activity, for all four subjects and almost over the complete range of *D*, which proves that the perspective vehicle symbol contributes to the system damping. On the other hand, the perspective vehicle symbol yielded a somewhat larger lateral deviation. In the vertical control these effects were less pronounced. The vertical results of the four subjects are shown in Figs. 15-18 and indicate that also the vertical deviation strongly increased with D. The perspective vehicle symbol yielded a somewhat larger vertical deviation than the predictor cross, which might be attributed to the fact that the vehicle symbol with its complex shape is harder to match to the tunnel square.

Time histories of single runs of subject B, for the perspective vehicle symbol and for the 2-D predictor cross, are compared in Figs. 19-24. Figs. 19 and 20 clearly demonstrate the lower roll activity as well as lateral stick activity for the perspective vehicle symbol at $D_0 = 1{,}500$ and $D_0 = 900$ ft. At $D_0 = 2{,}000$ the difference is less pronounced, probably because the lateral motion of the vehicle symbol provides sufficient damping cues, see Fig. 21.

The time-histories of the vertical control, shown in Figs. 22-24, indicate larger vertical deviations for the perspective vehicle symbol, whereas the pitch and stick activity are the same as for the predictor cross.

Results of manual velocity control

The results of auto-throttle control and manual velocity control by means of velocity tick-marks, are shown in Figs. 11-18. Neither in the lateral, nor in the vertical control did the results for the manual throttle differ significantly from the results for the auto-throttle, which proves that velocity control could be carried out without affecting the tunnel following performance. For comparison, manual velocity control was carried out by means of the digital velocity read-out, shown in Fig. 1. In this experiment the predictor distance was kept constant at $D = D_0$ regardless of the variations in velocity. In contrast with velocity control by means of the tick-marks, velocity control by means of the digital read-out yielded a markedly deteriorated tunnel following performance, as seen by the significantly larger roll-activity and lateral and vertical deviations, but also a significantly larger velocity error auto-covariance and throttle activity. These findings are confirmed by the time-histories shown in Figs. 25-27. The large overshoots in velocity error and throttle displacement shown in Fig. 27 clearly demonstrate the lack of damping for velocity control with the digital read-out.

Results of the banked tunnel.

The banked tunnel was investigated, both in the roll-version, as well as in the roll-stabilized version. The performance of the roll-version of the banked tunnel was very similar to results of the straight tunnel, see Tables I-IV. The subjects commented, that in the roll-version, the bank-angle command information, provided by the tunnel elements banked in curves, did not really contribute to the following performance, and was ignored in most cases. Furthermore, the bank-angle command was only correct after entering a steady, coordinated turn. The incorrect bank-angle command in transients to curved sections was found confusing.

The roll-stabilized version of the banked tunnel yielded generally larger lateral deviations and roll-activity, than the roll-version, see Tables I-IV. This was attributed to the fact that the actual bank-angle, which in the roll-version is displayed by the inclination of the horizon, is no longer available in the roll-stabilized version. The predicted bank-angle, displayed by the vehicle symbol was clearly not sufficient. These results are confirmed by comparing the time-histories in Fig. 28 for the roll-stabilized banked tunnel, with the time-histories in Fig. 20 and 23 for the roll-version of the straight tunnel. Subjectopinion of the roll-stabilized version of the banked tunnel was less favourable than the one of the roll-version of the banked tunnel.

The effect of the tunnel width.

The results of the tunnel of 450 ft width varied between the subjects, see Tables I-IV. For subject B the roll-activity was significantly lower and the lateral deviation significantly larger for the 450 ft tunnel than for the 300 ft tunnel. Also for subject A the roll-activity was lower for the 450 ft tunnel, but the lateral deviation was the same. However, both subjects A and B showed a lower predicted lateral deviation for the 450 ft tunnel, which indicates that the subjects devoted more attention to the lateral error between vehicle symbol and tunnel square. Also subject C showed a lower roll-activity for the 450 ft tunnel, and smaller lateral deviation. The subjects commented that generally the 450 ft tunnel was easier to control than the 300 ft tunnel.

Results of the full-state predictor law.

The full-state predictor law yielded slightly larger roll-activities and slightly larger lateral deviations than the basic circular path law. This might be attributed to the fact that in the full-state law the bank-angle rate component of the bank-angle prediction, is much smaller than in the basic law, see Eqs. (A. 96) and (A. 97) of the Appendix. However, subject opinion was more in favour of the full-state predictor law, since disturbingly rapid roll-motions found with the basic law, were missing.

D.2 Results of Trajectory Entry

The entry experiment was conducted in a series of six runs. For each run the initial location was chosen at random and without replacement from the set of six initial locations given in Fig. 9. Significant differences between the scores were observed, for the various initial locations. In order to rate the general entry performance, a series score was computed by averaging the results of the 6 runs in each series. For each display configuration at least 6 series of runs were performed. The experimental results are summarized in Table V and Figs. 29-32 and represent the average and standard deviation of sets of at least 6 series-scores.

The roll-activity and lateral stick activity tended to be lower for the perspective vehicle symbol than for the 2-D predictor cross. Note the difference in control strategy between the subjects: in contrast to subjects C and D, subjects A and B show less control activity on the account of a larger lateral score, see Fig. 29.

The vertical results in Fig. 30, clearly show a larger vertical score for the perspective vehicle symbol, which might be explained by the fact that the perspective symbol is harder to match to the tunnel square. Time-histories of single entries are shown in Figs. 31 and 32. No significant difference in control strategy between the perspective vehicle symbol and the 2-D predictor cross are noticed.

D.3 Results of Preliminary Simulator Tests at Langley Research Center

In the qualitative evaluation at Langley Research Center the tunnel with perspective vehicle symbol and basic circular path predictor law, was investigated. In most runs, no atmospheric disturbances were present. The pilot subjects found the perspective vehicle symbol more difficult to familiarize with, than the flat 2-D predictor cross. After familiarization with the display, the predicted pitch and yaw attitude angles, were found useful. However, the predicted bank-angle was found to be confusing since it was composed of both actual bank-angle as well as bank-angle rate. It was found preferable to bring the bank-angle rate portion of the prediction to zero and to display the actual bank-angle only. Note that for the full-state predictor law, the bank-angle rate portion of the bank-angle prediction is considerably smaller than for the basic predictor law, see Eqs. (A.96) and (A.97) of the Appendix. The pilot's rejection of the bank-angle rate portion of the prediction, thus confirms that the first order bank-angle prediction of Eq. (A.34) is not sufficient.

The following parameters were varied: (1) Nominal predictor distance D_0, (2) Tunnel width, (3) Predictor size and (4) Trajectory curvature. At a nominal airspeed of 130 knots, the most suitable predictor distance was between 900 and 1,250 ft. A tunnel width of 450 ft and a perspective vehicle symbol with a wing span of 80% of the tunnel width, was found adequate.

Two trajectories were tested: a strongly curved path yielding steady state bank-angles of about 27.2 degrees and a moderately curved path, yielding steady state bank-angles of about 16.6 degrees. Both for the strongly curved path, as well as for the moderately curved path, the perspective vehicle symbol yielded an adequate performance. However, the maximum bank-angle for the strongly curved path was too large to be acceptable in actual flight.

Manual velocity control by means of velocity tick-marks proved successful. Accurate velocity control was obtained without overshoots and with minimal throttle activity. The manual velocity control did neither significantly increase pilot workload, nor affect the tunnel-following performance.

The banked tunnel was investigated, both for the roll-version, as well as for the roll-stabilized version. The roll-stabilized version was found preferable due to the fact that the bank-angle command was directly perceived as the inclination of the tunnel elements with respect to the stabilized horizon, and thus only with respect to the monitor frame as well. In contrast with the simulations at the Technion in which the predicted bank-angle was displayed, at the Langley version the actual bank angle was available, since the bank-angle rate portion of the prediction was set to zero. Favourable opinion was given to the fact that in a steady coordinated turn the wings of the perspective vehicle symbol were parallel to the tunnel square.

Two main problems were encountered: (1) The vertical control was too inaccurate and yielded unacceptably large vertical path-angle variations; (2) In the lateral control transients to and from curved sections of the path were too sudden.

The reasons for the unsatisfactory vertical control are two-fold: (a) Since a contact analog display is used, horizontal and vertical picture scales are identical, i.e., ±45 degrees of visual angle. The visual angle which is satisfactory in the lateral control, is too insensitive in the vertical control. However, a reduced vertical visual angle is not possible since it would seriously distort the image. (b) The path-angle is not explicitly displayed.

Pilots commented, that although the lateral control was very satisfactory in straight sections as well as in steady curves, the transients from straight to curved sections were too sudden. This resulted from the fact that the curvature along the trajectory was varied in steps, without transients from one section to the other.

IV. CONCLUSIONS AND SUGGESTIONS FOR FURTHER RESEARCH

1. The perspective vehicle symbol requires a longer time to familiarize with than the 2-D predictor cross.
2. The perspective vehicle symbol yields a smaller roll-activity and thus contributes to the lateral system damping.
3. The perspective vehicle symbol yields generally larger vertical deviations.
4. The perspective vehicle symbol with velocity tick-marks enables accurate velocity control, without overshoots, with moderate throttle activity and without increasing the pilot workload or affecting the tunnel following performance.
5. A tunnel width of 450 ft and perspective vehicle symbol with a wingspan of 80% of the tunnel width yields the best pilot acceptance.
6. The full-state predictor law yields a better pilot acceptance than the basic circular path law, in particular with regard to the bank-angle prediction.
7. The vertical control in the present display configuration is too inaccurate and yields too large vertical path-angle variations. Future research efforts should be directed to the augmentation of the display with superimposed symbology, explicitly displaying the vertical path-angle in the correct scaling. The symbology should be located such, that it does neither interfere with the lateral control, nor clutter with existing symbology and yet is located as centrally as possible on the display.
8. The banked tunnel in the present configuration, is only effective in a steady coordinated turn. Incorrect bank-angle commands in transients are

found confusing. Future developments should deal with the definition of a higher-order continuous function for the trajectory curvature and commanded bank-angle. This function should be custom-taylored to the average vehicle response, in order to enable the pilot to follow the trajectory through straight, transient and curved sections by matching the actual bank-angle to the commanded bank-angle.

V. APPENDIX

A. VEHICLE MODEL

The lateral and longitudinal dynamics are assumed to be fully decoupled. The linearized lateral equations of motion of the vehicle, for small deviations from the nominal trim condition, are given by:

$$\begin{bmatrix} \dot\beta \\ \dot p \\ \dot\varphi \\ \dot r \end{bmatrix} = \begin{bmatrix} Y_v & 0 & g/U_0 & -1 \\ L'_\beta & L'_p & 0 & L'_r \\ 0 & 1 & 0 & 0 \\ N'_\beta & N'_p & 0 & N'_r \end{bmatrix} \begin{bmatrix} \beta \\ p \\ \varphi \\ r \end{bmatrix} + \begin{bmatrix} Y^*_{\delta_a} & Y^*_{\delta_r} \\ L'_{\delta_a} & L'_{\delta_r} \\ 0 & 0 \\ N'_{\delta_a} & N'_{\delta_r} \end{bmatrix} \begin{bmatrix} \delta_{a_s} \\ \delta_{r_s} \end{bmatrix} +$$

$$+ \begin{bmatrix} -Y_v & 0 \\ -L'_\beta & -L'_p \\ 0 & 0 \\ -N'_\beta & -N'_p \end{bmatrix} \begin{bmatrix} \beta_g \\ p_g \end{bmatrix} \qquad \text{(A.1)}$$

where: $Y^*_\delta = Y_\delta/U_0$; $\beta_g = v_g/U_0$

and the "primed" derivatives L'_i and N'_i are given by

$$L'_i = \frac{L_i + N_i J_{xz}/I_{xx}}{1 - J_{xz}{}^2/(I_{xx} I_{zz})} \qquad N'_i = \frac{N_i + L_i J_{xz}/I_{zz}}{1 - J_{xz}{}^2/(I_{xx} I_{zz})} \qquad \text{(A.2a,b)}$$

where i can be β, p, r, δ_a, δ_r.

In this study, the stability derivatives of a DC-8 aircraft are chosen, in the approach-to-landing, trimmed at a nominal airspeed of 243.5 ft/sec and with flaps extended to 35 degrees. The dimensional stability derivatives are derived from Ref. [2] and given in Table VI.

The lateral stability is largely improved by a lateral stability augmentation system including a roll-rate on aeleron feedback, a yaw-rate on rudder feedback with wash-out and a sideslip on rudder feedback. Aeleron and rudder servo actuators are modelled by a first-order lag with a 10. rad/sec break frequency. The equations of motion of the control system, including servo actuators, are given by:

$$\dot{\delta}_{a_s} = -10.0\delta_{a_s} + 10.0\, e_a \qquad (A.3)$$

$$\dot{\delta}_{r_s} = -10.0\delta_{r_s} + 10.0\, e_r \qquad (A.4)$$

where e_a and e_r are the inputs to the servo actuators given by:

$$e_a = 1.0p + \delta_a \qquad (A.5)$$

$$e_r = -8.0\beta + 8.0\, r_w \qquad (A.6)$$

where r_w is the state of the wash-out filter, given by

$$\dot{r}_w = -1.0r_w + \dot{r} \qquad (A.7)$$

and δ_a is the command input to the system, originating from a lateral control stick motion. Turn coordination is accomplished by means of the sideslip on rudder feedback and the rudder pedals are not used.

The linearized longitudinal equations of motion of the vehicle, for small deviations from the nominal trim condition are given by:

$$\begin{bmatrix} \dot{u} \\ \dot{w} \\ \dot{q} \\ \dot{\theta} \end{bmatrix} = \begin{bmatrix} X_u & X_w & 0 & -g \\ Z_u & Z_w & U_0 & 0 \\ M'_u & M'_w & M'_q & 0 \\ 0 & 0 & 1 & 0 \end{bmatrix} \begin{bmatrix} u \\ w \\ q \\ \theta \end{bmatrix} + \begin{bmatrix} X_{\delta_e} & 1 \\ Z_{\delta_e} & 0 \\ M'_{\delta_e} & 0 \\ 0 & 0 \end{bmatrix} \begin{bmatrix} \delta_{e_s} \\ \delta_{th_s} \end{bmatrix} + \begin{bmatrix} -X_u & -X_w \\ -Z_u & -Z_w \\ -M'_u & -M'_w \\ 0 & 0 \end{bmatrix} \begin{bmatrix} u_g \\ w_g \end{bmatrix} \tag{A.8}$$

where: $M'_u = M_u + M_{\dot{w}} Z_u \;;\; M'_w = M_w + M_{\dot{w}} Z_w$

$$M'_q = M_q + M_{\dot{w}} U_0 \;;\; M'_{\delta_e} = M_{\delta_e} + M_{\dot{w}} Z_{\delta_e} \tag{A.9a-d}$$

The dimensional stability derivatives are given in Table VI.

The longitudinal stability is augmented by a pitch rate on elevator feedback and an angle-of-attack on elevator feedback. The elevator servo is modelled as a first order lag and the equations of motion of the control system are given by:

$$\dot{\delta}_{e_s} = -10.0\ \delta_{e_s} + 10.0\ e_e \tag{A.10}$$

where: $e_e = 6.0\ q + 0.05\ w + \delta_e$ (A.11)

Throttle and engine dynamics are modelled by a first order lag with a time constant of 10 seconds. The auto-throttle includes a feedback of velocity error and of forward acceleration. The equations of motion of the auto-throttle system including engine lag are given by:

$$\dot{\delta}_{th_s} = -0.1\ \delta_{th_s} + 0.1\ e_{th} \tag{A.12}$$

where: $e_{th} = -0.05\ u - 0.5\ a_x$ (A.13)

For manual throttle control e_{th} is directly connected to the throttle, so that $e_{th} = \delta_{th}$.

In order to compute the vehicle path, the components of $\vec{V}$ in the body coordinate system, U_b, V_b, W_b have to be transformed in the components of $\vec{V}$ in the inertial coordinate system $\dot{x}_i$, $\dot{y}_i$, $\dot{z}_i$ according to:

$$\begin{bmatrix} \dot{x}_i \\ \dot{y}_i \\ \dot{z}_i \end{bmatrix} = E_{b\to i} \begin{bmatrix} U_b \\ V_b \\ W_b \end{bmatrix} \tag{A.14}$$

$$\text{where} \quad E_{b\to i} \overset{\Delta}{=} [E_{i\to b}]^T \tag{A.15}$$

is the transformation matrix for rotation from body to inertial system, which is the transpose of the Euler matrix $E_{i\to b}$ for rotation from inertial to body system. The Euler matrix is composed of a successive yaw, pitch and roll rotation, in that order according to:

$$E_{i\to b} \overset{\Delta}{=} [E_\varphi][E_\theta][E_\psi] \tag{A.16}$$

where:

$$E_\varphi \overset{\Delta}{=} \begin{bmatrix} 1 & 0 & 0 \\ 0 & \cos\varphi & \sin\varphi \\ 0 & -\sin\varphi & \cos\varphi \end{bmatrix}; \quad E_\theta \overset{\Delta}{=} \begin{bmatrix} \cos\theta & 0 & -\sin\theta \\ 0 & 1 & 0 \\ \sin\theta & 0 & \cos\theta \end{bmatrix};$$

$$E_\psi \overset{\Delta}{=} \begin{bmatrix} \cos\psi & \sin\psi & 0 \\ -\sin\psi & \cos\psi & 0 \\ 0 & 0 & 1 \end{bmatrix} . \tag{A.17a-c}$$

The vehicle path is obtained by integration of $\dot{x}_i$, $\dot{y}_i$ and $\dot{z}_i$.

The relation between the body rotations p, q, r and the Euler angle rates $\dot{\varphi}$, $\dot{\theta}$, $\dot{\psi}$ is given by:

$$\begin{bmatrix} p \\ q \\ r \end{bmatrix} = \begin{bmatrix} \dot{\varphi} \\ 0 \\ 0 \end{bmatrix} + [E_\varphi] \begin{bmatrix} 0 \\ \dot{\theta} \\ 0 \end{bmatrix} + [E_\varphi][E_\theta] \begin{bmatrix} 0 \\ 0 \\ \dot{\psi} \end{bmatrix} \qquad \text{(A.18)}$$

and the inverse relations are given by:

$$\begin{aligned} \dot{\varphi} &= p + q \tan\theta \sin\varphi + r \tan\theta \cos\varphi \\ \dot{\theta} &= q \cos\varphi - r \sin\varphi \\ \dot{\psi} &= r(\cos\varphi/\cos\theta) + q(\sin\varphi/\cos\theta) \end{aligned} \qquad \text{(A.19a-c)}$$

The Euler angles are obtained by integration of $\dot{\varphi}$, $\dot{\theta}$ and $\dot{\psi}$. For relatively small values of θ and φ, Eqs. (A.19a-c) become:

$$\begin{aligned} \dot{\varphi} &= p \\ \dot{\theta} &= q \\ \dot{\psi} &= r \end{aligned} \qquad \text{(A.20a-c)}$$

B. PREDICTOR LAWS

B. Predictor Laws Based on a Circular Predicted Vehicle Path

The predicted vehicle path is assumed to be tangential to the velocity vector of the vehicle, $\vec{V}$. The projections of the predicted vehicle path on the $x_i y_i$ locally level plane and on the $x_i z_i$ locally vertical plane, are hereafter referred to as the lateral and vertical vehicle path, respectively. The vehicle path is computed from the lateral and vertical path accelerations, which are derived hereafter.

The translatory equations of motion of the vehicle are given by:

$$\begin{aligned} \dot{U}_b + QW_b - RV_b + g \sin \Theta \quad &= \frac{1}{m} X = a^m_{x_b} \\ \dot{V}_b + RU_b - PW_b - g \cos \Theta \sin \Phi &= \frac{1}{m} Y = a^m_{y_b} \\ \dot{W}_b + PV_b - QU_b - g \cos \Theta \cos \Phi &= \frac{1}{m} Z = a^m_{z_b} \end{aligned} \qquad \text{(A.21a-c)}$$

where $a^m_{x_b}$, $a^m_{y_b}$ and $a^m_{z_b}$ constitute the specific forces measured by accelerometers in x_b, y_b and z_b body axis direction, respectively. The inertial accelerations in body axis direction are given by:

$$\begin{aligned} a^i_{x_b} &= \dot{U}_b + QW_b - RV_b \\ a^i_{y_b} &= \dot{V}_b + RU_b - PW_b \\ a^i_{z_b} &= \dot{W}_b + PV_b - QU_b \end{aligned} \qquad \text{(A.22a-c)}$$

From Eqs.(A.21) and Eqs. (A.22) it follows that the inertial accelerations in body axis direction can be computed from the measured accelerations by:

$$
\begin{aligned}
a^{i}_{x_b} &= a^{m}_{x_b} - g \sin \theta \\
a^{i}_{y_b} &= a^{m}_{y_b} + g \cos \theta \sin \varphi \\
a^{i}_{z_b} &= a^{m}_{z_b} + g \cos \theta \cos \varphi
\end{aligned}
\qquad \text{(A.23a-c)}
$$

The lateral and vertical path accelerations a_ℓ and a_v are then obtained by:

$$a_\ell = a^{i}_{y_b} \cos \varphi - a^{i}_{z_b} \sin \varphi \qquad \text{(A.24)}$$

$$a_v = a^{i}_{y_b} \sin \varphi + a^{i}_{z_b} \cos \varphi \qquad \text{(A.25)}$$

Assuming the lateral and vertical path accelerations remain constant over the prediction span, a circular lateral and vertical vehicle path is obtained. The instantaneous lateral and vertical path-angle rates $\dot{\chi}$ and $\dot{\xi}$ are computed from:

$$\dot{\chi}(t) = a_\ell(t)/V \quad \text{and} \quad \dot{\xi}(t) = a_v(t)/V \qquad \text{(A.26a,b)}$$

respectively. The situation for the horizontal path is shown in Fig. 33. The actual path-angle and lateral deviation are denoted by χ and y_d respectively, and the predicted path-angle and predicted lateral deviation by χ_p and y_{d_p}, respectively. For relatively small angles of ψ, β and χ, the predicted path angle and lateral deviation, T seconds in the future, are given by:

$$\chi_p(t) = \chi(t) + \nu(t) \qquad \text{(A.27)}$$

$$y_{d_p}(t) = y_d(t) + D\,\chi(t) + D\,\frac{\nu(t)}{1 + \sqrt{1-\nu(t)^2}} \qquad \text{(A.28)}$$

where $\nu(t) = T\,\dot{\chi}(t)$ (A.29) and D is the predictor distance for a prediction T seconds in the future. For constant V the distance D is given by $D = TV$. Note that the lateral displacement of the vehicle symbol on the display screen is given by the visual angle at which the symbol is seen in the $x_b y_b z_b$ body coordinate system. The lateral visual angle λ_ℓ is given by:

$$\lambda_\ell(t) = \chi(t) + \frac{\nu(t)}{1 + \sqrt{1-\nu(t)^2}} \qquad (A.30)$$

Eqs. (A.29) and (A.30) shows that the variables necessary for positioning the vehicle symbol on the display, are the path angle and path-angle rate only.

For small χ, actual path-angle and lateral deviation are related by:

$$y_d(t) = \chi(t)/V \qquad (A.31)$$

Substitution of Eqs. (A.31) and (A.29) in Eqs. (A.27) and (A.28) yields after linearlization:

$$\chi_p(t) = \chi(t) + T\,\dot{\chi}(t) \qquad (A.32)$$

$$y_{d_p}(t) = y_d(t) + T\,\dot{y}_d(t) + \frac{1}{2}T^2\,\ddot{y}_d(t) \qquad (A.33)$$

which are Taylor series expansions, until the first and second derivative. Similarly, the predicted bank-angle φ_p can be approximated by:

$$\varphi_p(t) = \varphi(t) + T\,\dot{\varphi}(t) \qquad (A.34)$$

The circular predicted vehicle path given by Eqs. (A.27) and (A.28) is useful in particular in following constantly curved sections of the trajectory.

In the steady state, the radius of the vehicle path will be equal to the radius of the trajectory which enables a zero steady-state error in the lateral deviation.

The equations for the vertical vehicle path are identical to Eqs. (A.27) and (A.28). Since constantly curved sections do not exist in the vertical profile of the trajectory, the linear approximations of Eqs.(A.32) and (A.33) will be sufficient for the vertical vehicle path.

B.2 Predictor Laws for Forward Velocity Control

For a given prediction time T, the predictor distance D can be computed from the present states of the longitudinal dynamics and from the present control commands. Since the engine dynamics and velocity control are of a much lower natural frequency than the short-period dynamics, the computation of D can be simplified. The engine dynamics are represented by a first-order lag with time-constant $1/c$ seconds, given by:

$$\dot{a}_x = -ca_x + k\,\delta_{th} \tag{A.35}$$

where a_x is the forward acceleration, due to engine thrust and δ_{th} is the throttle position setting. The forward velocity U is the integral of a_x, and the travelled distance S is the integral of U. The state equation for the simplified velocity control system is given by:

$$\begin{bmatrix} \dot{a}_x \\ \dot{U} \\ \dot{S} \end{bmatrix} = \begin{bmatrix} -c & 0 & 0 \\ 1 & 0 & 0 \\ 0 & 1 & 0 \end{bmatrix} \cdot \begin{bmatrix} a_x \\ U \\ S \end{bmatrix} + \begin{bmatrix} k \\ 0 \\ 0 \end{bmatrix} \delta_{th} \tag{A.36}$$

or written shortly as:

$$\dot{\underline{x}}_t(t) = A_t \, \underline{x}_t(t) + B_t \, \delta_{th}(t) \tag{A.37}$$

Assuming δ_{th} remains constant over the prediction span, a linear prediction, τ seconds in the future, from the present time t onwards is given by:

$$\underline{x}_t(t+\tau) = \Phi_t(\tau) \, \underline{x}_t(t) + \Gamma_t(\tau) \, B_t \, \delta_{th}(t) \tag{A.38}$$

where $\Phi_t(\tau)$ is the transition matrix at τ and

$$\Gamma_t(\tau) = \int_{\sigma=0}^{\tau} \Phi_t(\sigma) d\sigma \tag{A.39}$$

where

$$\Phi_t(\tau) = \begin{bmatrix} e^{-c\tau} & 0 & 0 \\ -\frac{1}{c}\left(e^{-c\tau} - 1\right) & 1 & 0 \\ \frac{1}{c^2}\left(e^{-c\tau} + c\tau - 1\right) & \tau & 1 \end{bmatrix} \tag{A.40}$$

and

$$\Gamma_t(\tau) = \begin{bmatrix} -\frac{1}{c}\left(e^{-c\tau} - 1\right) & 0 & 0 \\ \frac{1}{c^2}\left(e^{-c\tau} + c\tau - 1\right) & \tau & 0 \\ -\frac{1}{c^3}\left(e^{-c\tau} - \frac{c^2\tau^2}{2} + c\tau - 1\right) & \frac{\tau^2}{2} & \tau \end{bmatrix} \tag{A.41}$$

The travelled distance at $(t+\tau)$ is given by:

$$S(t+\tau) = \frac{1}{c^2}\left(e^{-c\tau} + c\tau - 1\right) a_x(t) + \tau\, U(t) +$$

$$+ S(t) - \frac{k}{c^3}\left(e^{-c\tau} - \frac{c^2\tau^2}{2} + c\tau - 1\right) \delta_{th}(t) \qquad \text{(A.42)}$$

For $\tau = T$ the predictor distance D is given by:

$$D = S(t+T) - S(t) \qquad \text{(A.43)}$$

Expanding the exponential term in Eq. (A.42) until the third derivative and substituting Eq. (A.42) in Eq. (A.43) yields:

$$D = T\, U(t) + \left(\frac{T^2}{2} - c\,\frac{T^3}{6}\right) a_x(t) + \frac{T^3}{6}\, k\, \delta_{th}(t) \qquad \text{(A.44)}$$

The vehicle symbol with velocity tick-marks will be positioned at distance D ahead, whereas the solid reference square at distance $D_0 = T\, U_0$ ahead, where U_0 is the desired velocity, see Fig. 1. The velocity U is brought to the desired value U_0 by bringing the distance between D and D_0 to zero. Thus the error for velocity control is defined as:

$$\varepsilon = D_0 - D \qquad \text{(A.45)}$$

and the structure of the control system is shown in Fig. 34a.

The effect of variations in U are strongly observed in apparent changes in size of the predictor symbol. Thus, an increase in U yields an increase in D, which is manifested in an apparent shrinking in size of the vehicle symbol. On the other hand, a decrease in U yields an apparent increase in size of the vehicle symbol. Eq. (A.44) also shows than an increase in engine thrust due to a forward throttle displacement, results in a simultaneous forward motion of the vehicle symbol, so that throttle displacement and vehicle symbol motion are in the same direction.

Note that, apart from a change in apparent symbol size, the location of the vehicle symbol on the image is not affected by variations in predictor distance. This location depends on the visual angle λ_ℓ only which does not depend on D, see Eq. (A.30).

The diagram of Fig. 34a is further simplified in Fig. 34b, which shows the existence of a second order lead-term in the feedback path, given by:

$$D(s) = \frac{T^3}{6}\left(s^2 + \frac{3}{T}s + \frac{6}{T^2}\right) U(s) \qquad \text{(A.46)}$$

The zeros of Eq. (A.46) have a natural frequency which is inverse proportional to T according to $\omega_n = 2.45/T$ rad/sec and a fixed damping ratio of $\zeta = 0.61$. Since the pilot response is much faster than the system response, the pilot transfer function can be considered as a simple gain K_p. For sufficiently large values of K_p, the closed loop system poles will be located at the zeros of Eq. (A.46), and will be the dominant system poles. A small value of T yields a well damped, fast response, whereas a large value of T yields a sluggish response. However, a fast response will be at the account of considerably increased throttle activity. A value of T should be chosen which yields a satisfactory response with still acceptable throttle activity.

Since the dynamics of the velocity control system are of a much lower natural frequency than the lateral and vertical dynamics, the value of T, optimized for velocity control will probably be too large for the lateral and vertical control. Fig. 34c shows the realization of a system in which the prediction time for velocity control differs from the prediction time for lateral/vertical control. The prediction time for velocity control is denoted by T_v and the prediction time for lateral/vertical control is denoted by T. Like in the previous cases the solid reference square is again positioned at $D_0 = T\,U_0$. However, the deviation $d = D_0 - D$ between the solid square and the tick-marks, is computed by means of prediction time T_v, Adequate results are obtained for $T_v = 2T$.

B.3 Full-State Predictor Laws

The full state predictor law is derived for the lateral predictor motions only. The derivation is valid for the vertical predictor motions as well. The lateral dynamics with stability augmentation system engaged, are derived in Appendix A. For simplicity, the yaw-rate wash-out filter and servo activator dynamics are replaced by unity gains. The augmented lateral system is given by:

$$\dot{\underline{x}}_0 = A_0\underline{x}_0 + B_0\underline{u} + W_0\underline{v}_g \qquad \text{(A.47)}$$

where A_0 is the system matrix, B_0 the control input matrix and W_0 the disturbance input matrix of dimensions $(m \times m)$, $(m \times n)$ and $(m \times k)$, respectively, and

$$\underline{x}_0 \overset{\Delta}{=} \mathrm{col}[\beta, p, \varphi, r]; \quad \underline{u} \overset{\Delta}{=} \delta_a \; ; \quad \text{and} \quad \underline{v}_g \overset{\Delta}{=} \mathrm{col}[\beta_g, r_g] \qquad \text{(A.48a-c)}$$

For small angular deviations from a straight reference trajectory, the heading angle ψ and lateral deviation y_d are obtained by integration of:

$$\dot{\psi} = r \qquad \text{(A.49)}$$

and $$\dot{y}_d = V(\psi + \beta) \tag{A.50}$$

Adding Eqs.(A.49) and (A.50) to Eq. (A.1) yields the following augmented system:

$$\left[\begin{array}{c}\dot{\beta}\\ \dot{p}\\ \dot{\varphi}\\ \dot{r}\\ \hline \dot{\psi}\\ \dot{y}_d\end{array}\right] = \left[\begin{array}{cccc|cc} \multicolumn{4}{c|}{A_0} & \multicolumn{2}{c}{\underline{0}} \\ \hline 0 & 0 & 0 & 1 & 0 & 0\\ V & 0 & 0 & 0 & V & 0\end{array}\right] \left[\begin{array}{c}\beta\\ p\\ \varphi\\ r\\ \hline \psi\\ y_d\end{array}\right] + \left[\begin{array}{c}B_0\\ \hline \underline{0}\end{array}\right]\underline{u} + \left[\begin{array}{c}W_0\\ \hline \underline{0}\end{array}\right]\underline{v}_g \tag{A.51}$$

Defining

$$\underline{x}_1 \overset{\Delta}{=} \mathrm{col}[\psi, y_d] \tag{A.52}$$

Eq. (A.51) can be written as:

$$\left[\begin{array}{c}\dot{\underline{x}}_0\\ \hline \dot{\underline{x}}_1\end{array}\right] = \left[\begin{array}{c|c}A_0 & \underline{0}\\ \hline P_1 & P_2\end{array}\right] \left[\begin{array}{c}\underline{x}_0\\ \hline \underline{x}_1\end{array}\right] + \left[\begin{array}{c}B_0\\ \hline \underline{0}\end{array}\right]\underline{u} + \left[\begin{array}{c}W_0\\ \hline \underline{0}\end{array}\right]\underline{v}_g \tag{A.53}$$

where P_1 and P_2 are partition matrices of dimension $(2 \times m)$ and (2×2), respectively. Eq. (A.53) can be written shortly as:

$$\dot{\underline{x}} = A\underline{x} + B\underline{u} + W\underline{v}_g \tag{A.54}$$

where $$\underline{x} \overset{\Delta}{=} \left[\begin{array}{c}\underline{x}_0\\ \hline \underline{x}_1\end{array}\right] \tag{A.55}$$

A linear prediction τ seconds in the future, from the present time t onwards, is given by:

$$\underline{x}(t+\tau) = \Phi(\tau)\underline{x}(t) + \int_{\sigma=0}^{\tau} \Phi(\tau)B\underline{u}(t+\tau)d\sigma + \int_{\sigma=0}^{\tau} \Phi(\tau)W\underline{v}_g(t+\tau)d\sigma \qquad \text{(A.56)}$$

where $\Phi(\tau)$ is the transition matrix at τ of the system of Eq. (A.54). The prediction of Eq. (A.56) consists of three parts: the first term at the right-hand side constitutes the homogeneous system response, the second term constitutes the forced motion due to control commands and the third term constitutes the forced motion due to external disturbances.

Assuming $\underline{u}(t)$ and $\underline{v}_g(t)$ remain constant over the prediction span, Eq. (A.56) can be simplified as:

$$\underline{x}(t+\tau) = \Phi(\tau)\underline{x}(t) + \Gamma(\tau)B\underline{u}(t) + \Gamma(\tau)W\underline{v}_g(t) \qquad \text{(A.57)}$$

where $\Gamma(\tau)$ is the first integral of $\Phi(\tau)$ according to:

$$\Gamma(\tau) = \int_{\sigma=0}^{\tau} \Phi(\sigma)d\sigma \qquad \text{(A.58)}$$

$\Phi(\tau)$ and $\Gamma(\tau)$ are given by the series expansions:

$$\Phi(\tau) = I + A\tau + A^2 \frac{\tau^2}{2!} + \ldots + A^n \frac{\tau^n}{n!} + \ldots \qquad \text{(A.59)}$$

$$\Gamma(\tau) = I\tau + A \frac{\tau^2}{2!} + A^2 \frac{\tau^3}{3!} + \ldots + A^{n-1} \frac{\tau^n}{n!} + \ldots \qquad \text{(A.60)}$$

Expanding the system matrix A by means of Eqs. (A.59) and (A.60) yields:

$$\Phi(\tau) = \left[\begin{array}{c|c} \Phi_0(\tau) & \underline{0} \\ \hline P_1\Gamma_0(\tau) + P_2P_1\Lambda_0(\tau) & I + P_2\tau \end{array}\right] \tag{A.61}$$

and

$$\Gamma(\tau) = \left[\begin{array}{c|c} \Gamma_0(\tau) & \underline{0} \\ \hline P_1\Lambda_0(\tau) + P_2P_1\Xi_0(\tau) & I\tau + P_2 \dfrac{\tau^2}{2} \end{array}\right] \tag{A.62}$$

where Φ_0 is the transition matrix of A_0 and Γ_0, Λ_0 and Ξ_0 are the first, second and third integrals of Φ_0, respectively and are given by the following series expansions:

$$\Phi_0(\tau) = I + A_0\tau + A_0^2 \frac{\tau^2}{2!} + \ldots + A_0^n \frac{\tau^n}{n!} + \ldots \tag{A.63}$$

$$\Gamma_0(\tau) = I\tau + A_0 \frac{\tau^2}{2!} + A_0^2 \frac{\tau^3}{3!} + \ldots + A_0^{n-1} \frac{\tau^n}{n!} + \ldots \tag{A.64}$$

$$\Lambda_0(\tau) = I \frac{\tau^2}{2!} + A_0 \frac{\tau^3}{3!} + A_0^2 \frac{\tau^4}{4!} + \ldots + A_0^{n-2} \frac{\tau^n}{n!} + \ldots \tag{A.65}$$

$$\Xi_0(\tau) = I \frac{\tau^3}{3!} + A_0 \frac{\tau^4}{4!} + A_0^2 \frac{\tau^5}{5!} + \ldots + A_0^{n-3} \frac{\tau^n}{n!} + \ldots \tag{A.66}$$

From Eqs. (A.63)-(A.66) the following relations can be derived:

$$\Lambda_0(\tau) = A_0\Xi_0(\tau) + I \frac{\tau^2}{2} \tag{A.67}$$

$$\Gamma_0(\tau) = A_0\Lambda_0(\tau) + I\tau \tag{A.68}$$

$$\Phi_0(\tau) = A_0\Gamma_0(\tau) + I \tag{A.69}$$

Substitution of Eq. (A.68) in the lower left partition of Eq. (A.61) yields:

$$\Phi(\tau) = \left[\begin{array}{c|c} \Phi_0(\tau) & \underline{0} \\ \hline P_3\Lambda_0(\tau) + P_1\tau & I + P_2\tau \end{array}\right] \tag{A.70}$$

and substitution of Eq. (A.67) in the lower left partition of Eq. (A.62) yields:

$$\Gamma(\tau) = \left[\begin{array}{c|c} \Gamma_0(\tau) & \underline{0} \\ \hline P_3\Xi_0(\tau) + P_1 \dfrac{\tau^2}{2} & I\tau + P_2 \dfrac{\tau^2}{2} \end{array}\right] \tag{A.71}$$

where P_3 is a matrix of dimension $(2 \times m)$ given by:

$$P_3 = P_1A_0 + P_2P_1 \tag{A.72}$$

Evaluating Eq. (A.57) with Eqs. (A.55) and Eqs. (A.70) and (A.71) yields the prediction of $\underline{x}_1$:

$$\begin{aligned} \underline{x}_1(t+\tau) = {} & P_3\Lambda_0(\tau)\underline{x}_0(t) + P_1\tau\underline{x}_0(t) + (I + P_2\tau)\underline{x}_1(t) + \\ & + P_3\Xi_0(\tau)B_0\underline{u}(t) + P_1 \frac{\tau^2}{2} B_0\underline{u}(t) + \\ & + P_3\Xi_c(\tau)W_0\underline{v}_g(t) + P_1 \frac{\tau^2}{2} W_0\underline{v}_g(t) \end{aligned} \tag{A.73}$$

Provided $\underline{x}_0(t)$ and $\underline{x}_1(t)$ are known exactly, the first terms on the right-hand side of Eq. (A.56) can be computed exactly. However, the remaining terms depend on the future values of $\underline{u}$ and $\underline{v}_g$ which are not known. With respect to the future values of u and v_g, three assumptions can be made which are shown in Fig. 35:

(1) $\underline{u}$ and $\underline{v}_g$ remain constant over the prediction span; (2) $\underline{u}$ and $\underline{v}_g$ are set to zero; (3) $\underline{u}$ and $\underline{v}_g$ decay exponentially over the prediction span,

according to:

$$\underline{u}(t+\tau) = \underline{u}(t)\ e^{-\tau/\tau_{d_1}} \qquad (A.74)$$

$$\underline{v}_g(t+\tau) = \underline{v}_g(t)\ e^{-\tau/\tau_{d_2}} \qquad (A.75)$$

where τ_{d_1} and τ_{d_2} are the time-constants of the decay. It is clear that τ_{d_1} or $\tau_{d_2} \to \infty$ is identical with assumption (1) and also that τ_{d_1} or $\tau_{d_2} \to 0$ is identical with assumption (2). Assuming $\underline{u}(t)$ and $\underline{v}_g(t)$ can be approximated by first-order Markov processes with spectral densities:

$$\Phi_{uu}(s) = \frac{1}{(a_1-s)(a_1+s)} \quad ; \quad \Phi_{v_g v_g}(s) = \frac{1}{(a_2-s)(a_2+s)} \qquad (A.76,77)$$

then the optimal prediction according to Wiener-Hopf is given exactly by Eqs.(A.74) and (A.75), where $\tau_{d_1} = 1/a_1$ and $\tau_{d_2} = 1/a_2$. Thus the time-constant of decay is determined by the break frequency of the Markov process.

Substituting Eqs.(A.74) and (A.75) into Eq. (A.56) yields:

$$\underline{x}(t+\tau) = \Phi(\tau)\underline{x}(t) + \Gamma^*(\tau)B\underline{u}(t) + \Gamma^{**}(\tau)W\underline{v}_g(t) \qquad (A.78)$$

where Γ^* and Γ^{**} are expanded according to Eq. (A.60) but with the matrix A replaced by

$$A^* = [A - a_1 I] \qquad (A.79)$$

and

$$A^{**} = [A - a_2 I] \qquad (A.80)$$

respectively.

The prediction of $\underline{x}_1$, subject to decaying control and disturbance inputs, is then given by:

$$\begin{aligned}\underline{x}_1(t+\tau) = {} & P_3\Lambda_0(\tau)\underline{x}_0(t) + P_1\tau\underline{x}_0(t) + (I+P_2\tau)\underline{x}_1(t) + \\ & + P_3^*\Xi_0^*(\tau)B_0\underline{u}(t) + P_1\frac{\tau^2}{2}B_0\underline{u}(t) + \\ & + P_3^{**}\Xi_0^{**}(\tau)W_0\underline{v}_g(t) + P_1\frac{\tau^2}{2}W_0\underline{v}_g(t)\end{aligned} \tag{A.81}$$

where the $^{*)}$ and $^{**)}$ superscripts indicate that the corresponding matrix is generated with:

$$A_0^* = [A_0 - a_1 I] \tag{A.82}$$

and $$A_0^{**} = [A_0 - a_2 I] \tag{A.83}$$

respectively.

In Appendix B.1 it is shown, that linearization of the circular path yields a Taylor series expansion, until the second derivative. A prediction of $\underline{x}_1$ based on a Taylor series expansion is given by:

$$\underline{x}_{1_p}(t) = \underline{x}_1(t) + \tau\dot{\underline{x}}_1(t) + \frac{\tau^2}{2!}\ddot{\underline{x}}_1(t) \tag{A.84}$$

Differentiating the lower half of Eq. (A.53) with respect to t and substituting in Eq. (A.84) and using Eq. (A.72) yields:

$$\begin{aligned}\underline{x}_{1_p}(t) = {} & (I+\tau P_2)\underline{x}_1(t) + P_1\tau\underline{x}_0(t) + \frac{\tau^2}{2!}P_3\underline{x}_0(t) + \\ & + \frac{\tau^2}{2!}P_1B_0\underline{u}(t) + \frac{\tau^2}{2!}P_1W_0\underline{v}_g(t)\end{aligned} \tag{A.85}$$

The difference between the two prediction methods is defined as:

$$\Delta\underline{x}_1(t+\tau) \overset{\Delta}{=} \underline{x}_1(t+\tau) - \underline{x}_{1_p}(t) \tag{A.86}$$

Subtracting Eq. (A.85) from Eq. (A.81) and substituting Eq. (A.67) yields:

$$\Delta\underline{x}_1(t+\tau) = P_3 A_0 \Xi_0(\tau)\underline{x}_0(t) + P_3^{*}\Xi_0^{*}(\tau)B_0\underline{u}(t) +$$

$$+ P_3^{**}\Xi_0^{**}(\tau)W_0\underline{v}_g(t) \tag{A.87}$$

Eq. (A.87) yields predictions for the heading angle ψ and the lateral deviation, y_d. However, it was found more useful to provide the lateral path-angle χ rather than the heading angle, so that the vehicle symbol is at all times tangential to the vehicle path. A combined linear/non-linear predictor law can be formulated by replacing the term $\frac{\tau}{2T}\ddot{x}_1(t)$ in Eq. (A.84) by a circular path. At $\tau = T$ the predictions for path-angle and lateral deviation are given by:

$$\chi(t+T) = \chi(t) + T\dot{\chi}(t) + \Delta\chi(t+T) \tag{A.88}$$

$$y_d(t+T) = y_d(t) + D\chi(t) + D\frac{T\dot{\chi}(t)}{1+\sqrt{1-[T\dot{\chi}(t)]^2}} + \Delta y_d(t+T) \tag{A.89}$$

Eqs. (A.88) and (A.89) are identical with Eqs. (A.27) and (A.28) of the circular path prediction with the addition of the terms $\Delta\chi(t+T)$ and $\Delta y_d(t+T)$. The addition for the lateral deviation follows from Eq. (A.87) and is given by:

$$\Delta y_d(t+T) = row_2[P_3 A_0 \Xi_0(T)]\underline{x}_0(t) +$$

$$+ row_2[P_3^{*}\Xi_0^{*}(T)B_0]\underline{u}(t) +$$

$$+ row_2[P_3^{**}\Xi_0^{**}(T)W_0]\underline{v}_g(t) \tag{A.90}$$

where $row_2[\ldots]$ denotes the second row of matrix $[\ldots]$. The addition for the path-angle is obtained by using the relation:

$$\Delta\chi(t+\tau) = \frac{1}{V}\frac{\partial}{\partial\tau}\,[\Delta y_d(t+\tau)] \tag{A.91}$$

Differentiating Eq. (A.87) with respect to τ and substituting $\tau = T$ yields:

$$\begin{aligned}\Delta\chi(t+T) = \frac{1}{V}\Big\{&\mathrm{row}_2\,[P_3A_0\Lambda_0(T)]\underline{x}_0(t) + \\ &+ \mathrm{row}_2\,[P_3^*\Lambda_0^*(T)B_0]\underline{u}(t) + \\ &+ \mathrm{row}_2\,[P_3^{**}\Lambda_0^{**}(T)W_0]\underline{v}_g(t)\Big\}\end{aligned} \tag{A.92}$$

The linear/non-linear predictor law given by Eqs. (A.88), (A.89) and Eqs. (A.90) and (A.92) combines the advantage of a circular path predictor law, i.e., the zero steady-state error in constantly curved sections, with the advantage of the sophisticated full-state predictor law of providing a more accuracte prediction.

The prediction for the bank-angle follows directly from Eqs. (A.78), (A.55) and (A.48a) and is given by:

$$\varphi(t+T) = \mathrm{row}_3[\Phi_0(T)]\underline{x}_0(t) + \mathrm{row}_3[\Gamma_0^*(T)B_0]\underline{u}(t) + \mathrm{row}_3[\Gamma_0^{**}(T)W_0]\underline{v}_g(t) \tag{A.93}$$

B.4 Numerical Solutions of Predictor Laws

The lateral vehicle dynamics with SAS engaged and servo actuator and wash-out dynamics considered as unity gains, are given by the following matrices:

$$A_0 = \begin{bmatrix} -0.302 & 0.0 & 0.132 & -0.810 \\ -2.832 & -1.677 & 0.0 & 2.059 \\ 0.0 & 1.0 & 0.0 & 0.0 \\ 3.869 & -0.177 & 0.0 & -3.377 \end{bmatrix}$$

and

$$B_c = \begin{bmatrix} 0.0 \\ -0.726 \\ 0.0 \\ -0.053 \end{bmatrix} .$$

For T = 6 sec and V = 243.5 ft/sec the transition matrix and integral matrices are given by:

$$\Phi_c = \begin{bmatrix} -0.0191 & 0.0510 & 0.0906 & 0.0360 \\ 0.0049 & -0.0134 & -0.0234 & -0.0093 \\ -0.1766 & 0.4711 & 0.8359 & 0.3324 \\ -0.0224 & 0.0597 & 0.1059 & 0.0421 \end{bmatrix}$$

$$\Gamma_0 = \begin{bmatrix} 0.6851 & 0.2870 & 0.5323 & 0.0001 \\ -0.1766 & 0.4711 & -0.1641 & 0.3324 \\ -1.2420 & 2.7950 & 5.4960 & 1.9040 \\ 0.8008 & 0.2864 & 0.5871 & 0.2663 \end{bmatrix}$$

$$\Lambda_0 = \begin{bmatrix} 4.027 & 0.772 & 1.494 & -0.495 \\ -1.242 & 2.795 & -0.504 & 1.904 \\ -3.815 & 7.930 & 17.01 & 5.187 \\ 4.441 & 0.653 & 1.564 & 1.031 \end{bmatrix}$$

$$\Xi_0 = \begin{bmatrix} 11.30 & 1.377 & 2.775 & -1.723 \\ -3.815 & 7.930 & -0.987 & 5.187 \\ -7.466 & 14.91 & 34.58 & 9.344 \\ 11.83 & 0.968 & 2.768 & 2.779 \end{bmatrix}$$

The matrix P_3 is computed with Eq. (A.72) and is given by:

$$P_3 = \begin{bmatrix} 3.869 & -0.177 & 0.0 & -3.377 \\ -73.46 & 0.0 & 32.19 & 46.36 \end{bmatrix}$$

When assuming δ_a remains constant over the prediction span, then $\tau_{a_1} \to \infty$ and $a_1 = 0$ so that $\Lambda_0^* = \Lambda_0$, and substituting the previous values in Eq. (A.90) and Eq. (A.91) yields:

$$\Delta\psi_d(t+6) = 1110.\ \beta + 228.8\ p - 69.0\ \varphi - 583.4\ r - 337.0\ \delta_a \tag{A.94}$$

and

$$\Delta y(t+6) = 1.59\ \beta + 0.337\ p - 0.115\ \varphi - 0.840\ r - 0.737\ \delta_a \tag{A.95}$$

The first order roll-prediction of Eq. (A.34) is given by:

$$\varphi_p(t) = 1.0\ \varphi + 6.0\ p \tag{A.96}$$

and the full-state roll prediction of Eq. (A.93) is given by

$$\varphi(t+T) = -0.1766\ \beta + 0.4711\ p + 0.8359\ \varphi + 0.332\ r - 2.136\ \delta_a \qquad (A.97)$$

Fig. 36 shows the coefficient of δ_a in the computation of Δy_d, as a function of T and for various values of τ_{d_1}. Fig. 36 shows, that the curves can be closely approximated by quadratic functions, which might considerably simplify on-line on-board computations. Fig. 37 shows these curves for the coefficient of δ_a in the computation of χ. Also the curves in Fig. 37 can be approximated by linear or quadratic functions.

C. ALGORITHMS FOR COMPUTING THE TRANSITION AND INTEGRAL MATRICES

The computation of the transition matrix and integral matrices starts with the computation of the third integral matrix $\Xi_0(\tau)$, by means of the series expansion of Eq. (A.66). The expansion is continued until the norm of the n-th term is sufficiently small. The second integral matrix $\Lambda_0(\tau)$ is obtained by substituting $\Xi_0(\tau)$ into Eq. (A.67), the first integral matrix $\Gamma_0(\tau)$ is obtained by substituting $\Lambda_0(\tau)$ into Eq. (A.68) and finally the transition matrix $\Phi_0(\tau)$ is obtained by substituting $\Gamma_0(\tau)$ into Eq. (A.69).

Computational difficulties may arise for large values of τ, resulting in overflow before the series converges. For the computation of $\Phi_0(\tau)$ this difficulty can be overcome by subdividing τ in N intervals $\Delta\tau$ according to: $\tau = N\Delta\tau$, and using the relation:

$$\Phi_0(\tau) \overset{\Delta}{=} \Phi_0(N\Delta\tau) = \{\Phi_0(\Delta\tau)\}^N \qquad (A.98)$$

However, this relation is not valid for the integral matrices, and the correct expressions are derived hereafter.

Given the homogeneous system equation of order m:

$$\dot{\underline{z}}_0 = A_0 \underline{z}_0 \tag{A.99}$$

The first, second and third integrals of $\underline{z}_0$ are defined as:

$$\dot{\underline{z}}_1 \triangleq \underline{z}_0 \quad ; \quad \dot{\underline{z}}_2 \triangleq \underline{z}_1 \quad ; \quad \dot{\underline{z}}_3 \triangleq \underline{z}_2 \tag{A.100a-c}$$

and an augmented system of order $4m$ is defined as:

$$\begin{bmatrix} \dot{\underline{z}}_0 \\ \hline \dot{\underline{z}}_1 \\ \hline \dot{\underline{z}}_2 \\ \hline \dot{\underline{z}}_3 \end{bmatrix} = \left[\begin{array}{c|c|c|c} A_0 & \underline{0} & \underline{0} & \underline{0} \\ \hline I & \underline{0} & \underline{0} & \underline{0} \\ \hline \underline{0} & I & \underline{0} & \underline{0} \\ \hline \underline{0} & \underline{0} & I & \underline{0} \end{array}\right] \begin{bmatrix} \underline{z}_0 \\ \hline \underline{z}_1 \\ \hline \underline{z}_2 \\ \hline \underline{z}_3 \end{bmatrix} \tag{A.101}$$

or shortly written as:

$$\dot{\underline{z}} = A\underline{z} \tag{A.102}$$

The transition matrix Φ is obtained by expanding A according to Eq. (A.59), and is given by:

$$\Phi(\tau) = \left[\begin{array}{c|c|c|c} \Phi_0(\tau) & \underline{0} & \underline{0} & \underline{0} \\ \hline \Gamma_0(\tau) & I & \underline{0} & \underline{0} \\ \hline \Lambda_0(\tau) & I\tau & I & \underline{0} \\ \hline \Xi_0(\tau) & I\frac{\tau^2}{2!} & I\tau & I \end{array}\right] \tag{A.103}$$

where the first partition column contains the required matrices. The relation, given in Eq. (A.98) is applied to the augmented system matrix of Eq. (A.103) and thus $\Phi(\Delta\tau)$ is raised to the power N by $(N-1)$ repeated multiplications. The n-th multiplication yields a matrix, from which the first column partition contains the following expressions:

$$\Phi_0^{n+1} = \Phi_0^n \Phi_0 \qquad \text{(A.104)}$$

$$\Gamma_0^{n+1} = \Gamma_0^n \Phi_0 + \Gamma_0 \qquad \text{(A.105)}$$

$$\Lambda_0^{n+1} = \Lambda_0^n \Phi_0 + n\tau\Gamma_0 + \Lambda_0 \qquad \text{(A.106)}$$

$$\Xi_0^{n+1} = \Xi_0^n \Phi_0 + \frac{n^2\tau^2}{2!}\Gamma_0 + n\tau\Lambda_0 + \Xi_0 \qquad \text{(A.107)}$$

where:

$$\Phi_0^n \overset{\Delta}{=} \Phi_0(n\Delta\tau) \quad ; \quad \Gamma_0^n \overset{\Delta}{=} \Gamma_0(n\Delta\tau) \quad \text{etc.} \qquad \text{(A.108a,b)}$$

and

$$\Phi_0 \overset{\Delta}{=} \Phi_0^1 \overset{\Delta}{=} \Phi_0(\Delta\tau) \quad ; \quad \Gamma_0 \overset{\Delta}{=} \Gamma_0^1 \overset{\Delta}{=} \Gamma_0(\Delta\tau) \quad \text{etc.} \qquad \text{(A.109a,b)}$$

The algorithm starts with subdividing τ into N sufficiently small intervals $\Delta\tau$. Next, Ξ_0, Λ_0, Γ_0 and Φ_0 are computed by means of the expansion of Eq. (A.66) and by means of Eqs. (A.67), (A.68) and (A.69). These matrices are substituted in Eqs. (A.104)-(A.107) to obtain the value of the matrices at $n = 2$ or $(2\Delta\tau)$.

The results are used in the next iteration to obtain the values at $n = 3$ or $(3\Delta\tau)$. Thus, starting with $n = 1$ the process is repeated until $n = N-1$, which finally yields the values of the matrices at $\tau = N\Delta\tau$

D. COMPUTER-GRAPHICS METHOD FOR DRAWING THE 3-D PERSPECTIVE VEHICLE SYMBOL

A vehicle symbol, which is generated as a "wire-frame" structure is ambiguous because it is not clear whether the vehicle symbol is pointing towards or away from the observer. In order to obtain an unambiguous vehicle symbol, the hidden lines should be removed from the image. However, commonly used algorithms for removing hidden lines, require considerable computational efforts which might unfavorably affect the update rate.

An alternative fast method has been developed to remove hidden lines from the image without requiring additional CPU time. Although the vehicle symbol chosen in this program has a square and constant fuselage cross-section this method applies to any, not necessarily constant cross-section. The hidden-line removal is restricted to the fuselage structure. Thus the fuselage appears "solid" but the wings and tail still appear transparent. In spite of these restrictions a clear and unambiguous image is obtained with minimal computational efforts.

The basic vehicle symbol structure is defined by a set of coordinates in the object coordinate system x_p, y_p, z_p, in between which straight lines are drawn, see Fig. 38. The coordinates are given in Table VII. The image is observed in the eye coordinate system (aligned with the body coordinate system) with the observer's eye at its origin, see Fig. 39. Thus each coordinate in the object coordinate system is transformed into a coordinate in the eye coordinate system according to:

$$\begin{bmatrix} x_e \\ y_e \\ z_e \end{bmatrix} = \begin{bmatrix} & & \\ & E_{p\to e} & \\ & & \end{bmatrix} \begin{bmatrix} x_p \\ y_p \\ z_p \end{bmatrix} + \begin{bmatrix} dx_e \\ dy_e \\ dz_e \end{bmatrix} \qquad (A.110)$$

where dx_e, dy_e, dz_e is the location of the center of gravity of the vehicle symbol in the eye coordinate system and

$$E_{p\rightarrow e} \triangleq E_{\varphi_p} E_{\theta_p} E_{\psi_p} \tag{A.111}$$

is the Euler matrix for rotation from object to eye coordinate system given by Eqs. (A.16) and (A.17a-c). The symbol image is obtained by projecting the $x_e y_e z_e$ coordinates on an image plane in front of the observer and perpendicular to the x_e axis. The limits of this image plane are from +45 to -45 degrees horizontally and vertically. In order to draw the image, the coordinates on the image plane have to be interconnected by lines. The pattern in which the coordinates are connected is defined by a list of move/draw instructions. Each instruction is a coordinate number, which can have a positive or a negative sign. A positive sign indicates that the CRT beam moves from its previous location to the specified coordinate while drawing a visible line (draw) and a negative sign indicates a shift to the specified coordinate with the CRT beam blanked (move). The first location in the list contains a count of the total number of move/draws. Special treatment is required for lines from which one or both coordinates fall outside the limits of the image plane. In that case, the line is only partially visible and the intersections of these lines with the image plane borders have to be computed (clipping). An efficient algorithm is implemented for handling this problem.

In order to determine which lines of the predictor fuselage are visible, the position of the observer's eye in the object coordinate system is to be computed according to:

$$\begin{bmatrix} dx_p \\ dy_p \\ dz_p \end{bmatrix} = - \begin{bmatrix} \\ E_{e\to p} \\ \\ \end{bmatrix} \begin{bmatrix} dx_e \\ dy_e \\ dz_e \end{bmatrix} \tag{A.112}$$

where $E_{e\to p}$ is the Euler matrix for rotation from eye to object coordinate system and

$$E_{e\to p} = \{E_{p\to e}\}^T \tag{A.113}$$

This transformation is shown in Fig. 39. The minus sign indicates that if the displacement of the vehicle position in the eye coordinate system is positive, the displacement of the eye position in the object system should be negative. Since $E_{p\to e}$ was already computed previously, its transpose is readily availabe and the transformation of Eq. (A.112) can be carried out with minimal computational effort. Seen from behind, the observer's eye can be located either above or below each one of the four planes applied through the fuselage sides, see Fig. 40. These planes are given by:

for right upper side A : $z_p + y_p = b$ (A.114)

for left lower side C : $z_p + y_p = -b$ (A.115)

for left upper side D : $z_p - y_p = b$ (A.116)

for right lower side B : $z_p - y_p = -b$ (A.117)

where b is half the diagonal of the fuselage cross-section. Altogether, there are nine areas in which the eye position can be located. In each of these areas different lines of the fuselage will be visible. A four-bit code determines the area in which the eye position is located. In order to compute this code, four tests are made and accordingly, the appropriate bit in the code is set in the following way:

above righ-upper : $dz_p + dy_p > b$ bit 0001 is set
below left-lower : $dz_p + dy_p < -b$ bit 0010 is set
above left-upper : $dz_p - dy_p > b$ bit 0100 is set
below right-lower: $dz_p - dy_p < -b$ bit 1000 is set

For each one of the nine areas, an individual move/draw list is defined which only draws the lines visible in that particular area. All the individual move/draw lists are stored sequentially in one area of the memory.

According to the value of the code, the appropriate move/draw list is referenced through an address table which, for each code, contains the address of the first location of the required list. If the code remains zero, none of the fuselage sides are visible and the image is completed after drawing the always visible parts of the image, e.i., wings, tail and rear surface of fuselage. A flow-chart of the computational method is shown in Fig. 41. The move/draw lists are given in Table VIII, and the address table in Table IX.

The method can be applied equally well to a fuselage with a non-square cross-section. For example, for a triangular cross-section the total number of areas, in which the eye position can be located is 7 and each area is labelled by a 3-bit code. For a hexagonal cross-section there are 19 possible areas, which are labelled by a 6 bit code and for an octagonal cross-section, there are 33 possible areas, labelled by an 8 bit code.

The vehicle symbol with hexagonal cross-section, is defined in Fig. 42 and the coordinates given in Table X. The possible areas in which the eye position can be located, are shown in Fig. 43. In order to compute the 6-bit code, six tests are made and the appropriate bit is set as follows:

for $dz_p + \frac{1}{\sqrt{3}} dy_p > b$ (above A) bit 000 001 is set

for $dz_p + \frac{1}{\sqrt{3}} dy_p < -b$ (below D) bit 000 010 is set

for $dz_p - \frac{1}{\sqrt{3}} dy_p > b$ (above F) bit 000 100 is set

for $dz_p - \frac{1}{\sqrt{3}} dy_p < -b$ (below C) bit 001 000 is set

for $dy_p > \frac{1}{2} \sqrt{3}\, b$ (right of B) bit 010 000 is set

for $dy_p < -\frac{1}{2} \sqrt{3}\, b$ (left of E) bit 100 000 is set

where b is half the diagonal of the hexagon.

The codes for the 17 areas are shown in Fig. 43, and the corresponding move/draw lists and address table are given in Tables XI and XII respectively. It is clear that a more complex fuselage cross-section will primarily increase the storage requirements for the move/draw lists, and, to a much lesser extend affect CPU requirements.

VI REFERENCES

1. Grunwald, A.J., Robertson, J.B., and Hatfield, J.J., "Evaluation of a Computer-Generated Perspective Tunnel Display for Flight-Path Following," NASA TP 1736, December 1980.

2. McRuer, D., Ashkenas, I., and Graham, D., "Aircraft Dynamics and Automatic Control," Princeton University Press, 1973, pp. 711-717.

TABLE I. RESULTS OF TRAJECTORY FOLLOWING: SUBJECT A.

	"Straight" Tunnel; Width: 300 ft; Roll Version									"Banked" Tunnel		
	2-D Predictor			3-D Predictor				Manual Throttle 3-D Predictor D_0 = 1500 ft		3-D Predictor D_0 = 1500 ft		
	D_0 = 900 ft	D_0 = 1500 ft	D_0 = 2000 ft	D_0 = 900 ft	D_0 = 1500 ft	D_0 = 2000 ft	"Full" State Predictor Law D_0=1500 ft	"tick" Marks	Digital Read-Out	Width: 300 ft	Width: 450 ft	Width: 300 ft
										Roll-Version		Roll Stabilized
NUMBER OF RUNS	6	6	8	6	6	8	6	6	6	8	6	6
Cov (y_{d_p}) [10^5 ft^2]	0.141 ±0.045	1.008 ±0.122	1.943 ±0.241	0.250 ±0.036	1.213 ±0.093	2.053 ±0.246	0.972 ±0.118	0.857 ±0.216	0.789 ±0.077	0.623 ±0.060	0.484 ±0.064	-
Cov (z_{d_p}) [10^4 ft^2]	0.312 ±0.066	2.001 ±0.278	4.066 ±0.649	0.759 ±0.067	2.742 ±0.187	5.108 ±0.638	2.715 ±0.391	4.269 ±1.737	3.064 ±0.591	2.010 ±0.199	2.137 ±0.261	-
Cov (y_d) [10^4 ft^2]	0.160 ±0.069	0.361 ±0.046	0.438 ±0.073	0.316 ±0.065	0.288 ±0.058	0.488 ±0.081	0.381 ±0.031	0.318 ±0.048	0.438 ±0.159	0.374 ±0.057	0.342 ±0.063	0.563 ±0.111
Cov (z_d) [10^3 ft^2]	0.331 ±0.072	0.561 ±0.123	1.093 ±0.364	0.677 ±0.184	1.042 ±0.192	1.803 ±0.307	1.270 ±0.367	1.525 ±0.348	1.198 ±0.259	1.739 ±0.557	3.461 ±0.802	0.926 ±0.230
Cov (ϕ) [rad^2]	0.142 ±0.003	0.134 ±0.001	0.123 ±0.003	0.143 ±0.006	0.136 ±0.003	0.123 ±0.003	0.134 ±0.003	0.137 ±0.003	0.141 ±0.003	0.129 ±0.004	0.126 ±0.003	0.139 ±0.003
Cov (p) [10^{-2} (rad/sec)^2]	0.814 ±0.037	0.439 ±0.056	0.468 ±0.175	0.565 ±0.105	0.410 ±0.082	0.368 ±0.053	0.463 ±0.062	0.442 ±0.028	0.456 ±0.050	0.386 ±0.063	0.333 ±0.035	0.534 ±0.077
Cov (u) [10^2 (ft/sec)^2]	-	-	-	-	-	-	-	3.860 ±3.033	2.892 ±1.184	-	-	-
Cov (δ_{th}) [10 (ft/sec^2)^2]	-	-	-	-	-	-	-	0.686 ±0.096	1.285 ±0.918	-	-	-
Cov (δa) [10^{-1} rad^2]	1.102 ±0.116	0.901 ±0.178	0.642 ±0.334	0.902 ±0.216	0.887 ±0.222	0.450 ±0.112	1.088 ±0.148	0.582 ±0.077	0.439 ±0.107	0.444 ±0.099	0.520 ±0.141	1.120 ±0.152
Cov (δe) [10^{-1} rad^2]	0.332 ±0.088	0.216 ±0.051	0.280 ±0.136	0.246 ±0.060	0.209 ±0.035	0.192 ±0.045	0.441 ±0.071	0.310 ±0.118	0.218 ±0.083	0.199 ±0.035	0.253 ±0.068	0.237 ±0.060

TABLE II. RESULTS OF TRAJECTORY FOLLOWING: SUBJECT B.

	"Straight" Tunnel; width: 300 ft, Roll Version									"Banked" Tunnel		
	2-D Predictor			3-D Predictor				Manual Throttle 3-D Predictor D_s = 1500 ft		3-D Predictor D_s = 1500 ft		
	D_s = 500 ft	D_s = 1500 ft	D_s = 2000 ft	D_s = 900 ft	D_s = 1500 ft	D_s = 2000 ft	"Full" State Predictor Law D_s=1500 ft	"Tick" Marks	Digital Read-Out	Width: 300 ft	Width: 450 ft	Width: 300 ft
										Roll-Version		Roll Stabilized
NUMBER OF RUNS	6	6	6	6	8	6	10	6	7	6	6	6
Cov (e_{y_f}) [10^3 ft^2]	0.145 ±0.052	1.071 ±0.065	2.143 ±0.235	0.266 ±0.022	0.788 ±0.273	2.253 ±0.338	0.767 ±0.142	0.772 ±0.074	0.741 ±0.110	0.670 ±0.061	0.596 ±0.093	-
Cov (ε_{y_f}) [10^4 ft^2]	0.338 ±0.099	2.694 ±0.614	5.469 ±0.824	0.721 ±0.044	2.055 ±0.543	5.980 ±0.925	2.066 ±0.326	2.835 ±0.599	3.348 ±0.477	2.073 ±0.254	1.746 ±0.228	-
Cov (e_{z}) [10^3 ft^2]	0.160 ±0.046	0.360 ±0.025	0.299 ±0.063	0.251 ±0.019	0.293 ±0.061	0.374 ±0.095	0.307 ±0.069	0.261 ±0.023	0.340 ±0.082	0.236 ±0.028	0.374 ±0.062	0.272 ±0.014
Cov (ε_{z}) [10^3 ft^2]	0.501 ±0.115	1.956 ±0.593	1.257 ±0.378	0.581 ±0.092	1.065 ±0.196	1.774 ±0.534	1.199 ±0.400	1.333 ±0.565	1.519 ±0.413	0.974 ±0.145	1.010 ±0.192	0.896 ±0.157
Cov (ϕ) [rad^2]	0.151 ±0.005	0.138 ±0.005	0.138 ±0.001	0.143 ±0.004	0.131 ±0.005	0.134 ±0.003	0.141 ±0.003	0.140 ±0.004	0.149 ±0.004	0.134 ±0.002	0.129 ±0.003	0.134 ±0.003
Cov (r) [10^{-4} (rad/sec)^2]	0.937 ±0.095	0.667 ±0.068	0.595 ±0.069	0.637 ±0.102	0.375 ±0.063	0.311 ±0.034	0.490 ±0.044	0.397 ±0.073	0.567 ±0.085	0.374 ±0.027	0.284 ±0.023	0.457 ±0.064
Cov (u) [10^4 (ft/sec)^2]	-	-	-	-	-	-	-	0.492 ±0.212	2.718 ±1.455	-	-	-
Cov ($\dot{u}$) [10 (ft/sec^2)^2]	-	-	-	-	-	-	-	0.996 ±0.240	2.733 ±0.604	-	-	-
Cov (δ_a) [10^{-1} rad^2]	1.252 ±0.165	0.930 ±0.147	1.004 ±0.327	0.908 ±0.218	0.581 ±0.325	0.725 ±0.219	0.909 ±0.223	0.841 ±0.201	0.993 ±0.170	0.687 ±0.142	0.780 ±0.160	0.991 ±0.144
Cov (δ_e) [10^{-1} rad^2]	0.416 ±0.193	0.226 ±0.052	0.488 ±0.158	0.228 ±0.030	0.234 ±0.033	0.407 ±0.156	0.387 ±0.133	0.359 ±0.093	0.495 ±0.144	0.387 ±0.133	0.498 ±0.088	0.539 ±0.129

TABLE III. RESULTS OF TRAJECTORY FOLLOWING: SUBJECT C.

	"Straight" Tunnel; Width: 300 ft; Roll Version									"Banked" Tunnel		
	2-D Predictor			3-D Predictor				Manual Throttle 3-D Predictor D_0 = 1500 ft		3-D Predictor D_0 = 1500 ft		
	D_0 = 900 ft	D_0 = 1500 ft	D_0 = 2000 ft	D_0 = 900 ft	D_0 = 1500 ft	D_0 = 2000 ft	"Full" State Predictor Law D_0=1500 ft	"Tick" Marks	Digital Read-Out	Width: 300 ft	Width: 450 ft	Width: 300 ft
										Roll-Version		Roll Stabilized
NUMBER OF RUNS	5	6	6	7	6	7	6	6	7	6	6	7
Cov (y_{d_p}) $[10^5 ft^2]$	0.085 ±0.012	0.568 ±0.087	1.646 ±0.229	0.107 ±0.048	0.681 ±0.048	1.842 ±0.249	0.941 ±0.113	0.831 ±0.057	1.065 ±0.135	0.652 ±0.035	0.716 ±0.070	-
Cov (z_{d_p}) $[10^4 ft^2]$	0.480 ±0.042	1.520 ±0.327	4.294 ±0.812	0.658 ±0.175	2.024 ±0.285	5.038 ±0.537	2.896 ±0.421	3.543 ±0.552	3.027 ±0.388	2.563 ±0.137	3.368 ±0.337	-
Cov (y_d) $[10^4 ft^2]$	0.313 ±0.076	0.231 ±0.027	0.412 ±0.154	0.223 ±0.046	0.280 ±0.068	0.505 ±0.120	0.397 ±0.048	0.265 ±0.060	0.472 ±0.124	0.326 ±0.046	0.248 ±0.024	0.486 ±0.072
Cov (z_d) $[10^3 ft^2]$	1.190 ±0.182	0.969 ±0.151	1.748 ±0.611	1.574 ±0.391	1.448 ±0.278	2.382 ±0.726	2.056 ±0.389	1.630 ±0.359	1.783 ±0.539	2.637 ±0.192	4.523 ±0.783	1.695 ±0.250
Cov (ϕ) $[rad^2]$	0.153 ±0.005	0.136 ±0.005	0.133 ±0.004	0.148 ±0.007	0.137 ±0.002	0.130 ±0.005	0.138 ±0.003	0.141 ±0.004	0.137 ±0.004	0.133 ±0.003	0.135 ±0.002	0.133 ±0.004
Cov (r) $[10^{-2}(rad/sec)^2]$	1.018 ±0.125	0.746 ±0.111	0.743 ±0.099	0.769 ±0.060	0.574 ±0.057	0.438 ±0.059	0.596 ±0.092	0.538 ±0.053	0.639 ±0.088	0.402 ±0.061	0.344 ±0.044	0.449 ±0.049
Cov (u) $[10^2(ft/sec)^2]$	-	-	-	-	-	-	-	1.390 ±0.429	2.508 ±1.431	-	-	-
Cov (δ_{th}) $[10(ft/sec^2)^2]$	-	-	-	-	-	-	-	0.476 ±0.123	1.370 ±0.725	-	-	-
Cov (δ_a) $[10^{-1}rad^2]$	0.962 ±0.145	0.704 ±0.102	0.694 ±0.124	0.846 ±0.186	0.529 ±0.087	0.516 ±0.097	1.172 ±0.264	0.589 ±0.119	1.132 ±0.297	0.452 ±0.087	0.410 ±0.072	0.824 ±0.141
Cov (δ_e) $[10^{-1}rad^2]$	0.258 ±0.078	0.214 ±0.031	0.179 ±0.035	0.262 ±0.043	0.227 ±0.077	0.241 ±0.061	0.526 ±0.102	0.262 ±0.063	0.319 ±0.076	0.199 ±0.038	0.206 ±0.030	0.187 ±0.037

TABLE IV. RESULTS OF TRAJECTORY FOLLOWING: SUBJECT 2.

	"Straight" Tunnel; Width: 300 ft; Roll Version									"Banked" Tunnel		
	2-D Predictor			3-D Predictor				Manual Throttle 3-D Predictor D_0 = 1500 ft		3-D Predictor D_0 = 1500 ft		
	D_0 = 900 ft	D_0 = 1500 ft	D_0 = 2000 ft	D_0 = 900 ft	D_0 = 1500 ft	D_0 = 2000 ft	"Full" State Predictor Law D_0=1500 ft	"Tick" Marks	Digital Read-Out	Width: 300 ft	Width: 450 ft	Width: 300 ft
										Roll-Version		Roll Stabilized
NUMBER OF RUNS	7	7	6	7	8	5	-	8	6	7	-	-
Cov (y_{d_p}) [10^3 ft^2]	0.091 ±0.014	0.530 ±0.069	1.654 ±0.255	0.140 ±0.013	0.820 ±0.108	2.011 ±0.132	-	0.771 ±0.148	1.161 ±0.064	0.670 ±0.134	-	-
Cov (z_{d_p}) [10^4 ft^2]	0.270 ±0.160	0.503 ±0.197	4.078 ±0.514	0.398 ±0.178	1.008 ±0.249	4.548 ±0.322	-	1.241 ±0.251	4.397 ±0.449	2.650 ±0.453	-	-
Cov (y_d) [10^4 ft^2]	0.231 ±0.056	0.409 ±0.125	0.254 ±0.053	0.223 ±0.027	0.319 ±0.069	0.459 ±0.025	-	0.391 ±0.058	0.470 ±0.090	0.345 ±0.089	-	-
Cov (z_d) [10^3 ft^2]	1.213 ±0.284	2.575 ±0.652	1.156 ±0.227	1.365 ±0.412	1.864 ±0.447	1.077 ±0.274	-	1.574 ±0.472	2.341 ±0.371	2.173 ±0.336	-	-
Cov (ϕ) [rad^2]	0.137 ±0.004	0.129 ±0.004	0.128 ±0.003	0.139 ±0.006	0.130 ±0.002	0.134 ±0.003	-	0.135 ±0.003	0.140 ±0.004	0.136 ±0.004	-	-
Cov (p) [10^{-2}(rad/sec)^2]	0.901 ±0.106	0.607 ±0.154	0.675 ±0.137	0.548 ±0.122	0.387 ±0.073	0.488 ±0.042	-	0.446 ±0.072	0.468 ±0.078	0.440 ±0.097	-	-
Cov (u) [10^2(ft/sec)^2]	-	-	-	-	-	-	-	0.922 0.248	2.501 1.479	-	-	-
Cov ($\ddot{h}_{dh}$) [10(ft/sec^2)^2]	-	-	-	-	-	-	-	0.851 0.177	2.447 0.595	-	-	-
Cov (δa) [10^{-1}rad^2]	1.203 ±0.158	0.727 ±0.251	0.765 ±0.167	0.687 ±0.121	0.542 ±0.062	0.549 ±0.098	-	0.602 ±0.105	0.899 ±0.304	0.546 ±0.119	-	-
Cov (δe) [10^{-1}rad^2]	0.379 ±0.070	0.336 ±0.091	0.221 ±0.029	0.445 ±0.095	0.339 ±0.052	0.193 ±0.041	-	0.327 ±0.090	0.271 ±0.073	0.237 ±0.022	-	-

ORIGINAL PAGE IS
OF POOR QUALITY

TABLE V. RESULTS OF TRAJECTORY ENTRY.

"Straight" Tunnel, Width: 300 ft; Auto-throttle; Roll-Version; D_0 = 1500 ft								
SUBJECT	A		B		C		D	
PREDICTOR	2-D	3-D	2-D	3-D	2-D	3-D	2-D	3-D
No. of Series of 6 Runs	6	6	6	7	6	6	6	6
T_{ak} $[10^2 sec]$	0.199 ±0.014	0.205 ±0.027	0.207 ±0.009	0.206 ±0.006	0.191 ±0.009	0.189 ±0.010	0.195 ±0.010	0.182 ±0.006
T_{av} $[10^2 sec]$	0.127 ±0.006	0.140 ±0.014	0.129 ±0.004	0.142 ±0.013	0.125 ±0.002	0.132 ±0.011	0.124 ±0.003	0.125 ±0.002
$ac\ (y_d)$ $[10^3 ft^2]$	0.209 ±0.038	0.211 ±0.054	0.213 ±0.019	0.216 ±0.011	0.163 ±0.018	0.155 ±0.005	0.175 ±0.016	0.167 ±0.011
$ac\ (z_d)$ $[10^2 ft^2]$	0.249 ±0.016	0.394 ±0.040	0.296 ±0.025	0.368 ±0.022	0.278 ±0.023	0.391 ±0.022	0.299 ±0.037	0.358 ±0.042
Cov (ϕ) $[rad^2]$	0.197 ±0.010	0.199 ±0.010	0.197 ±0.004	0.195 ±0.002	0.222 ±0.009	0.225 ±0.003	0.221 ±0.006	0.214 ±0.006
Cov (p) $[10^{-2}(rad/sec)^2]$	0.402 ±0.080	0.365 ±0.107	0.331 ±0.018	0.238 ±0.020	0.494 ±0.099	0.406 ±0.022	0.465 ±0.080	0.367 ±0.039
Cov (δa) $[10^{-1} rad^2]$	0.313 ±0.065	0.268 ±0.084	0.226 ±0.013	0.164 ±0.013	0.330 ±0.064	0.259 ±0.016	0.328 ±0.062	0.244 ±0.027
Cov (δe) $[10^{-2} rad^2]$	0.620 ±0.053	0.697 ±0.174	0.644 ±0.053	0.638 ±0.049	0.659 ±0.042	0.765 ±0.076	0.664 ±0.053	0.654 ±0.043

ORIGINAL PAGE IS OF POOR QUALITY

TABLE VI. STABILITY DERIVATIVES OF DC-8 AIRCRAFT IN APPROACH-TO-LANDING

Lateral	Longitudinal
Y_v = -0.113 sec^{-1}	X_u = -0.0291 sec^{-1}
$Y^*_{\delta_a}$ = 0.	X_w = 0.0629 sec^{-1}
$Y^*_{\delta_r}$ = 0.0238 sec^{-1}/rad	X_{δ_e} = 0.
L'_β = -1.328 sec^{-2}	Z_u = -0.2506 sec^{-1}
L'_p = -0.951 sec^{-1}	Z_w = -0.6277 sec^{-1}
L'_r = 0.609 sec^{-1}	Z_{δ_e} = -10.19 ft sec^{-2}/rad
L'_{δ_a} = -0.726 sec^{-2}/rad	M_u = 0. (sec ft)$^{-1}$
L'_{δ_r} = 0.1813 sec^{-2}/rad	M_w = -0.0087 (sec ft)$^{-1}$
N'_β = 0.757 sec^{-2}	$M_{\dot{w}}$ = -0.0011 ft^{-1}
N'_p = -0.124 sec^{-1}	M_q = -0.7924 sec^{-1}
N'_r = -0.265 sec^{-1}	M_{δ_e} = -1.35 sec^{-2}/rad
N'_{δ_a} = -0.0532 sec^{-2}/rad	U_0 = 243.5 ft/sec
N'_{δ_r} = -0.389 sec^{-2}/rad	W_0 = 0.
U_0 = 243.5 ft/sec	g = 32.2 ft/sec^2
g = 32.2 ft/sec^2	δ_{flap} = 35 deg.
I_x = 3,090,000 slug ft^2	
I_z = 5,580,000 slug ft^2	
J_{xz} 28,000 slug ft^2	

TABLE VII. LIST OF COORDINATES OF PERSPECTIVE VEHICLE SYMBOL WITH SQUARE FUSELAGE CROSS-SECTION.

Coordinate Number	Value in units of half the fuselage width: d			Description
	x_p	y_p	z_p	
1	8.0	1.0	0.	fuselage
2	8.0	0.	1.0	
3	8.0	-1.0	0.	
4	8.0	0.	-1.0	
5	-8.0	1.0	0.	
6	-8.0	0.	1.0	
7	-8.0	-1.0	0.	
8	-8.0	0.	-1.0	
9	-8.0	0.	4.0	vertical stabilizer
10	-7.0	0.	4.0	
11	-4.0	0.	1.0	
12	-8.0	2.5	4.0	horizontal stabilizer
13	-8.0	-2.5	4.0	
14	-5.5	0.	4.0	
15	4.0	1.0	0.	left wing
16	-3.0	6.0	0.	
17	-3.0	1.0	0.	
18	-3.0	1.0	0.	right-wing
19	-3.0	-6.0	0.	
20	4.0	-1.0	0.	
21	0.	0.	6.0	vertical tick-marks
22	0.	0.	8.0	
23	0.	0.	-6.0	
24	0.	0.	-8.0	

TABLE VIII. MOVE/DRAW CODING LIST FOR PERSPECTIVE VEHICLE SYMBOL WITH SQUARE FUSELAGE CROSS-SECTION.

Code (Binary)	Code (Decimal)	List Address in Core	M/D Count	Coding List	Description
0000	0	A	22	-6,7,8,5,6,	Rear fuselage surface
				9,10,11,	vertical stabilizer
				-14,12,13,14,	horizontal stabilizer
				-15,16,17,	right wing
				-18,19,20,	left wing
				-21,22,-23,24	z_b-axis/vertical reference
		A+22			
0000	1	A+22+1	4	-6,2,1,5	side A
0010	2	+6	4	-8,4,3,7	side C
0100	4	+11	4	-7,3,2,6	side D
1000	8	+16	4	-5,1,4,8	side B
1001	9	+21	7	-6,2,1,4,8,-5,1	side A,B
1010	10	+29	7	-5,1,4,3,7,-8,4	side B,C
0110	6	+37	7	-8,4,3,2,6,-7,3	side C,D
0101	5	+45	7	-7,3,2,1,5,-6,2	side D,A

TABLE IX. ADDRESS TABLE FOR SQUARE FUSELAGE CROSS-SECTION.

Code	Address Location Move/Draw List in Core							
0-7	A*)	B**)+1	B+6	0***)	B+11	B+45	B+37	0
8-15	B+16	B+21	B+29	0****)	0	0	0	0

*) A is the address in core of the first location of list 0.

**) B = A + C where C is the move/draw count of list 0.

***) An address value 0 indicates that no move/draw list exists for this value of the code.

****) For code 11-15 no move/draw lists exist and this part of the table might be ommited, provided $0 \leqslant \text{CODE} \leqslant 10$.

TABLE X. LIST OF COORDINATES OF PERSPECTIVE VEHICLE SYMBOL WITH HEXAGONAL FUSELAGE CROSS-SECTION

Coordinate Number	Value in Units of Half the Fuselage Width: d			Description
	x_p	y_p	z_p	
1	8.0	1.0	-0.58	fuselage
2	8.0	1.0	0.58	
3	8.0	0.	1.15	
4	8.0	-1.0	0.58	
5	8.0	-1.0	-0.58	
6	8.0	0.	-1.15	
7	-8.0	1.0	-0.58	
8	-8.0	1.0	0.58	
9	-8.0	0.	1.15	
10	-8.0	-1.0	0.58	
11	-8.0	-1.0	-0.58	
12	-8.0	0.	-1.15	
13	-8.0	0.	4.0	vertical stabilizer
14	-7.0	0.	4.0	
15	-4.0	0.	1.15	
16	-8.0	2.5	4.0	horizontal stabilizer
17	-8.0	-2.5	4.0	
18	-5.5	0.	4.0	
19	4.0	1.0	-0.58	left wing
20	-3.0	6.0	-0.58	
21	-3.0	1.0	-0.58	
22	-3.0	1.0	-0.58	right wing
23	-3.0	-6.0	-0.58	
24	4.0	-1.0	-0.58	
25	0.	0.	6.0	vertical tick-marks
26	0.	0.	8.0	
27	0.	0.	-6.0	
28	0.	0.	-8.0	

ORIGINAL PAGE IS
OF POOR QUALITY

TABLE XI. MOVE/DRAW CODING LIST FOR PERSPECTIVE VEHICLE SYMBOL WITH HEXAGONAL FUSELAGE CROSS-SECTION.

Code (Binary)	Code (Decimal)	List Address in Core	M/D Count	Coding List	Description
000 000	0	A A+24	24	-9,10,11,12,7,8,9, 13,14,15, -16,17,18,16, -19,20,21, -22,23,24, -25,26,-27,28	rear fuselage surface vertical stabilizer horizontal stabilizer right wing left wing z_D-axis/vertical reference
000 001	1	A+24+1	4	-9,3,2,8	side A
000 010	2	+6	4	-12,6,5,11	side D
000 100	4	+11	4	-10,4,3,9	side F
001 000	8	+16	4	-7,1,6,12	side C
010 000	16	+21	4	-8,2,1,7	side B
100 000	32	+26	4	-11,5,4,10	side E
010 001	17	+31	7	-9,3,2,1,7,-8,2	side A,B
011 000	24	+39	7	-8,2,1,6,12,-7,1	side B,C
001 010	10	+47	7	-7,1,6,5,11,-12,6	side C,D
100 010	34	+55	7	-12,6,5,4,10,-11,5	side D,E
100 100	36	+63	7	-11,5,4,3,9,-10,4	side E,F
000 101	5	+71	7	-10,4,3,2,8,-9,3	side F,A
011 001	25	+79	10	-9,3,2,1,6,12,-8,2,-1,7	side A,B,C
011 010	26	+90	10	-8,2,1,6,5,11,-7,1,-6,12	side B,C,D
101 010	42	+101	10	-7,1,6,5,4,10,-12,6,-5,11	side C,D,E
100 110	38	+112	10	-12,6,5,4,3,9,-11,5,-4,10	side D,E,F
100 101	37	+123	10	-11,5,4,3,2,8,-10,4,-3,9	side E,F,A
010 101	21	+134	10	-10,4,3,2,1,7,-9,3,-2,8	side F,A,B

TABLE XII. ADDRESS TABLE FOR HEXAGONAL FUSELAGE CROSS-SECTION.

Code	Address Location Move/Draw List in Core							
0 - 7	A*)	B+1**)	B+6	0***)	B+11	B+71	0	0
8 - 15	B+16	0	B+47	0	0	0	0	0
16 - 23	B+21	B+31	0	0	0	B+134	0	0
24 - 31	B+39	B+79	B+90	0	0	0	0	0
32 - 39	B+26	0	B+55	0	B+63	B+123	B+112	0
40 - 47	0	0	B+101	0****)	0	0	0	0
48 - 55	0	0	0	0	0	0	0	0
56 - 63	0	0	0	0	0	0	0	0

*) A is the address in core of the first location of list 0.

**) B = A + C where C is the move/draw count of list 0.

***) an address value 0 indicates that no move/draw list exists for this value of the code.

****) for code 43-63 no move/draw lists exist and this part of the table might be ommitted, provided 0 ≤ CODE ≤ 42.

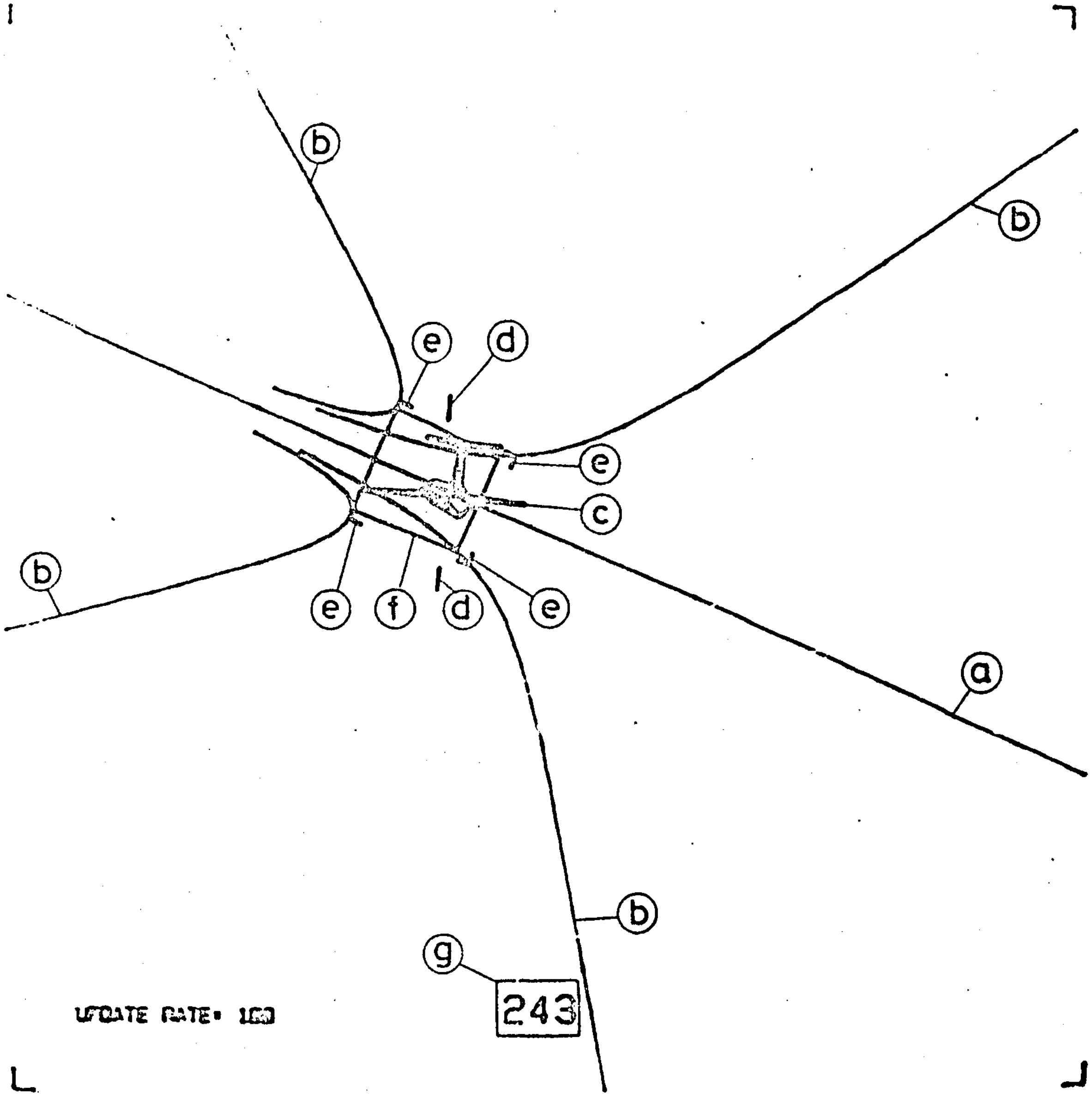

FIGURE 1. TUNNEL DISPLAY WITH PERSPECTIVE VEHICLE SYMBOL.

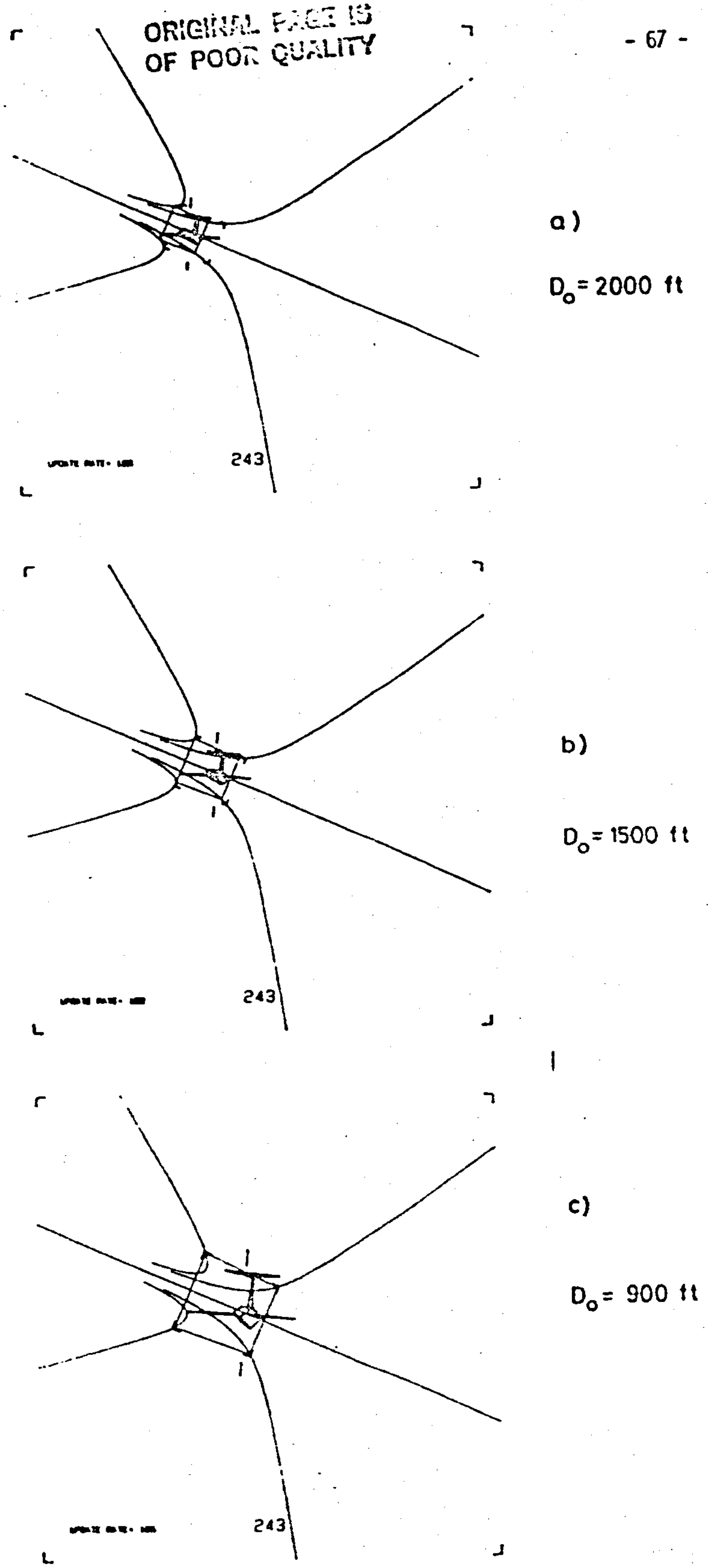

FIGURE 2. TUNNEL DISPLAY WITH PERSPECTIVE VEHICLE SYMBOL AT VARIOUS PREDICTOR DISTANCES:
(A) D_o = 2000 ft. (B) D_o = 1500 ft. (C) D_o = 900 ft.

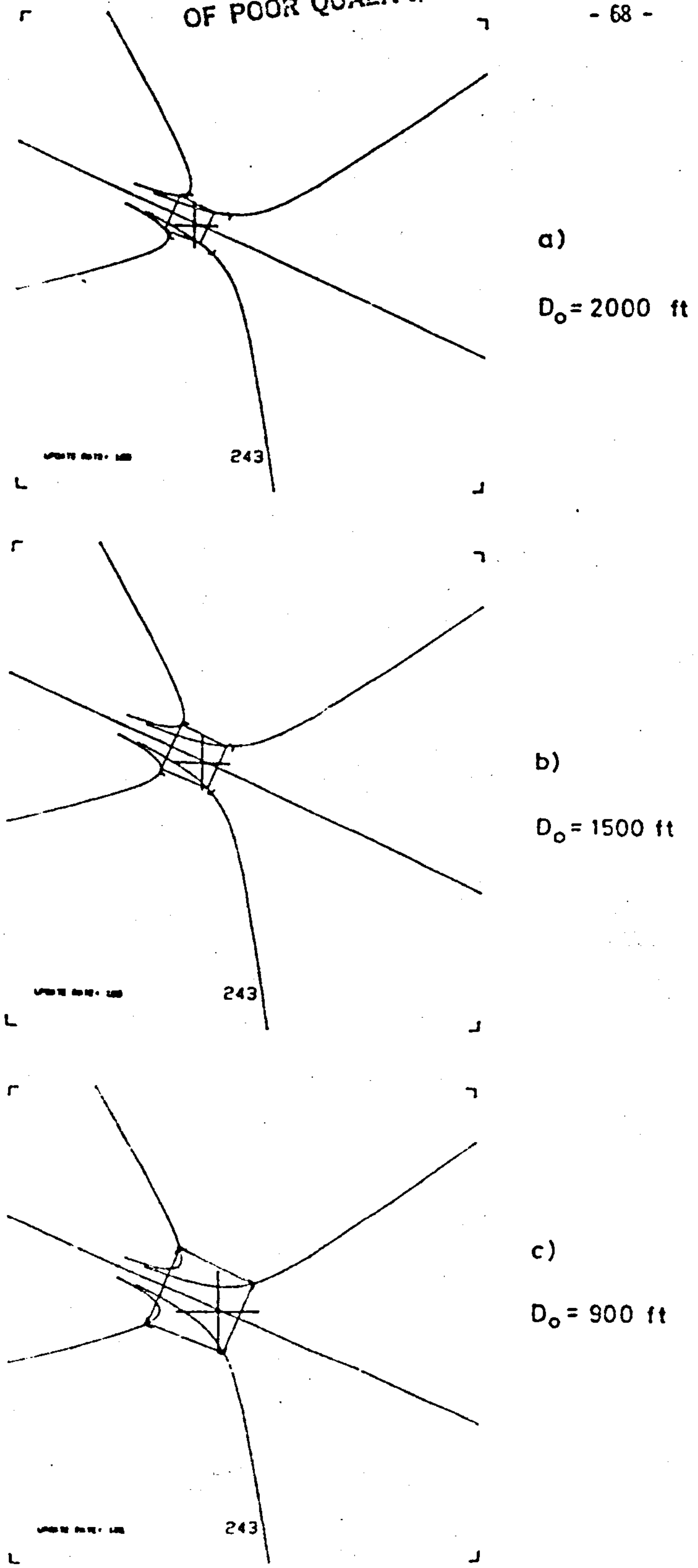

FIGURE 3. TUNNEL DISPLAY WITH TWO-DIMENSIONAL PREDICTOR CROSS AT VARIOUS PREDICTOR DISTANCES:

(A) D_o = 2000 ft, (B) D_o = 1500 ft, (C) D_o = 900 ft.

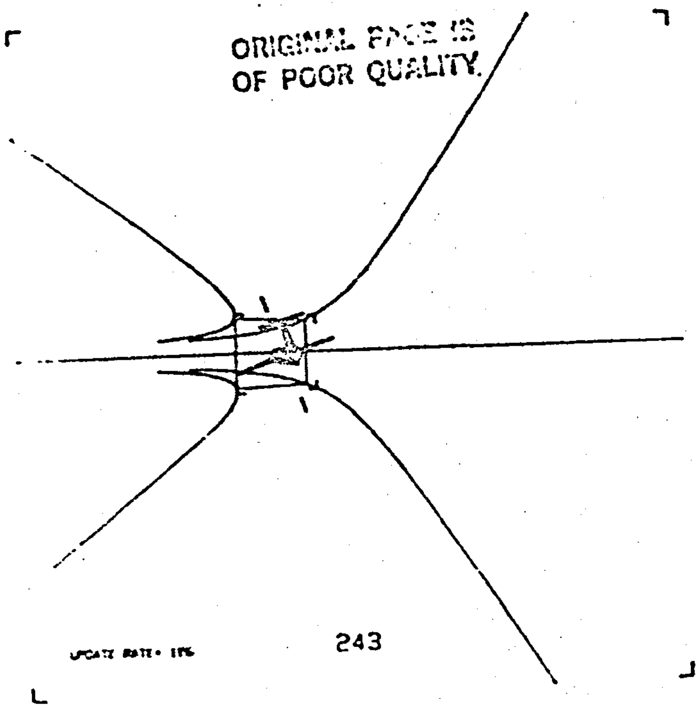

FIGURE 4. Roll-stabilized tunnel display.

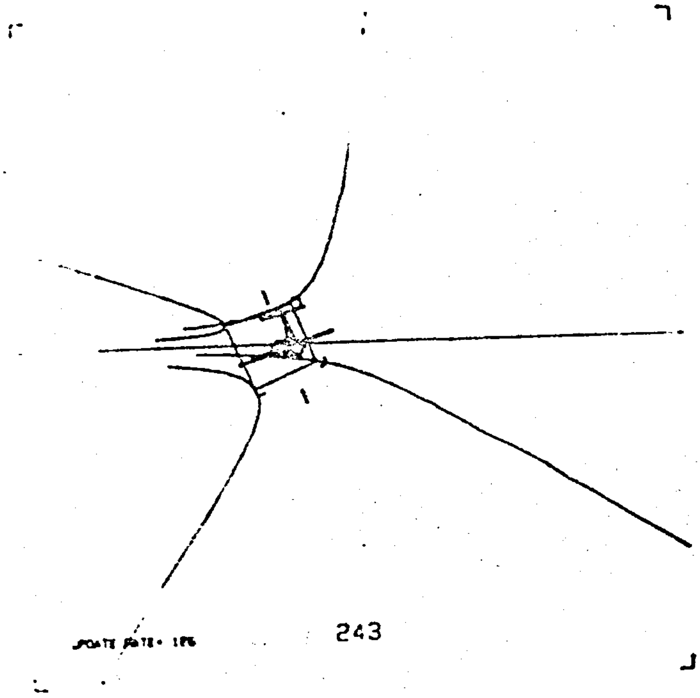

FIGURE 5. Banked tunnel; roll-stabilized version.

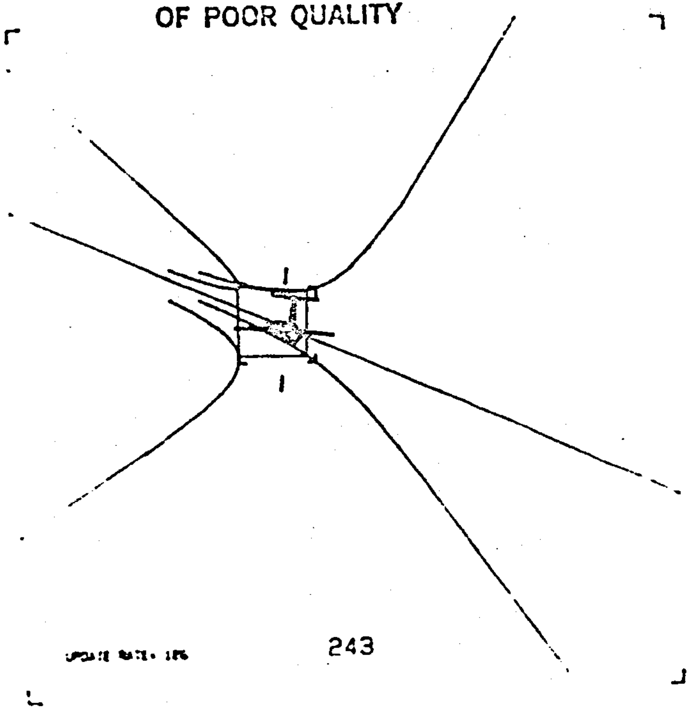

FIGURE 6. Banked tunnel; roll-version; width 300 ft.

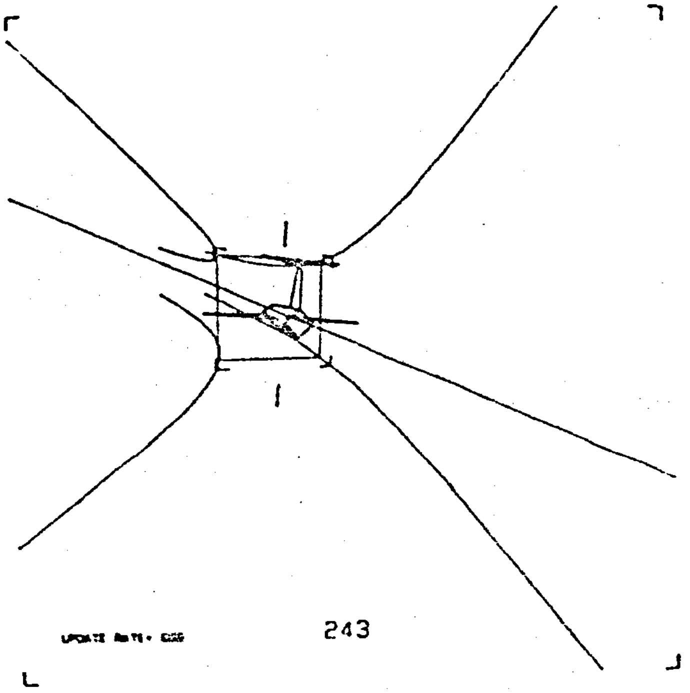

FIGURE 7. Banked tunnel; roll-version; width 450 ft.

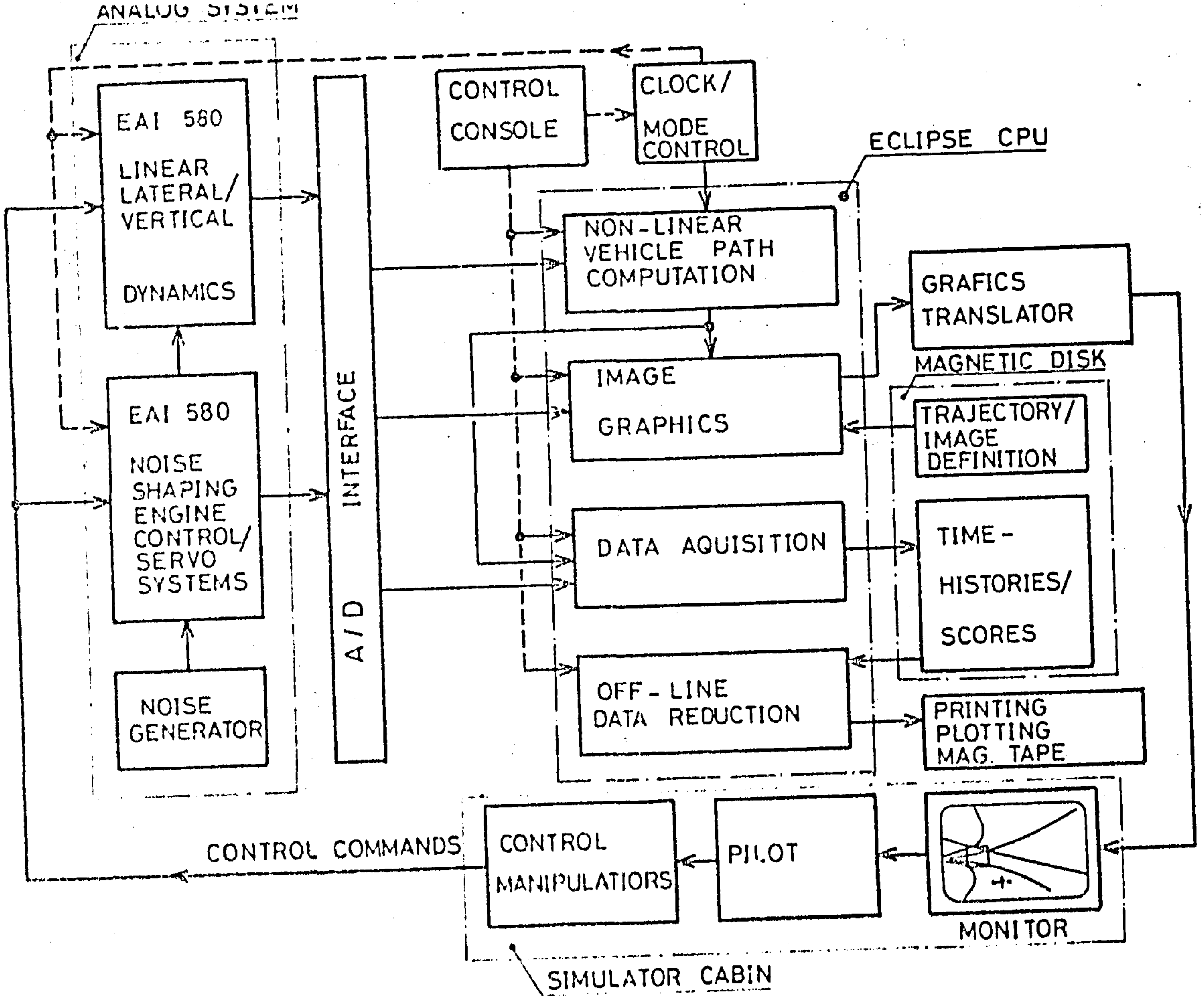

FIGURE 8. FUNCTIONAL DIAGRAM OF EXPERIMENTAL SYSTEM.

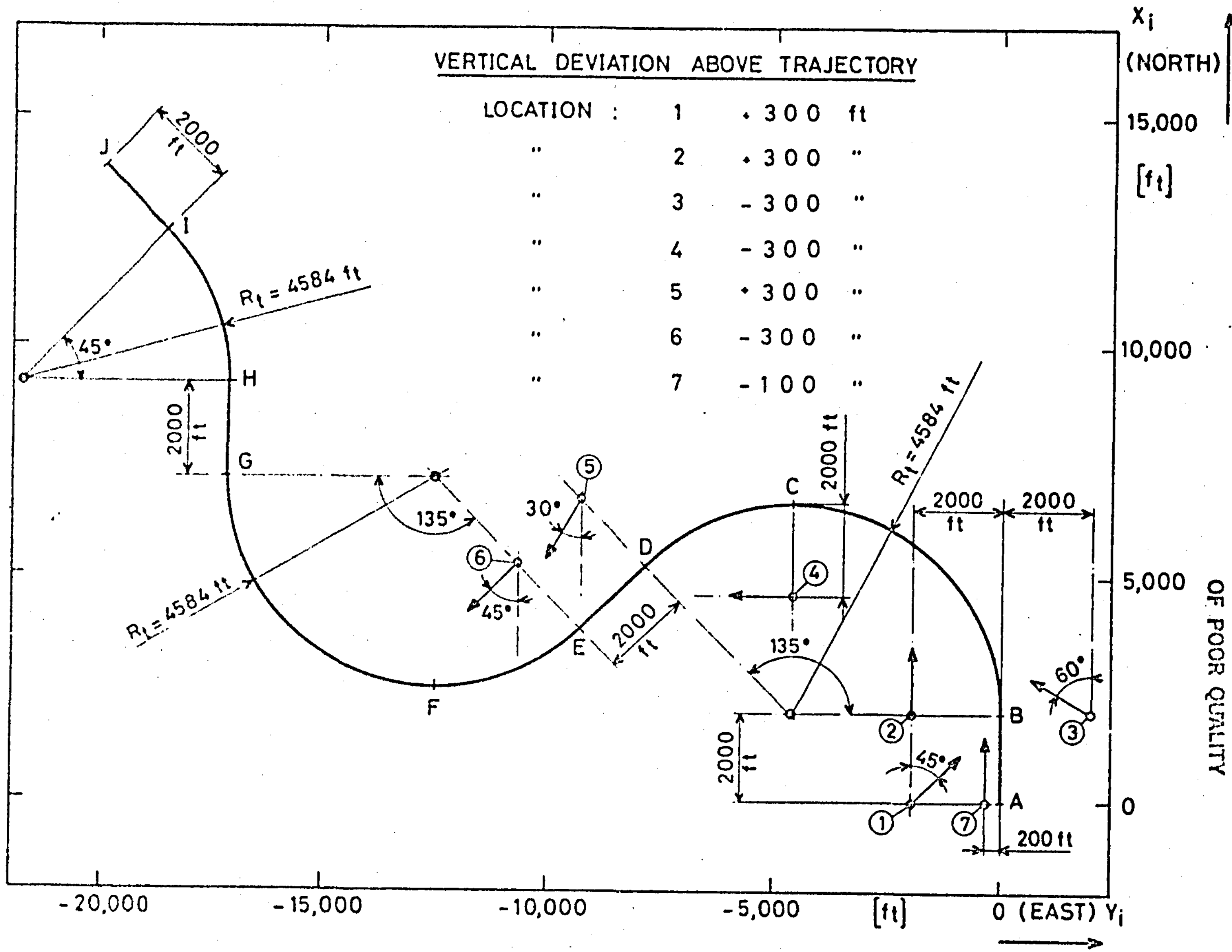

VERTICAL DEVIATION ABOVE TRAJECTORY

LOCATION		
LOCATION :	1	+ 300 ft
"	2	+ 300 "
"	3	- 300 "
"	4	- 300 "
"	5	+ 300 "
"	6	- 300 "
"	7	- 100 "

FIGURE 9. PLAN VIEW OF DESIRED TRAJECTORY.

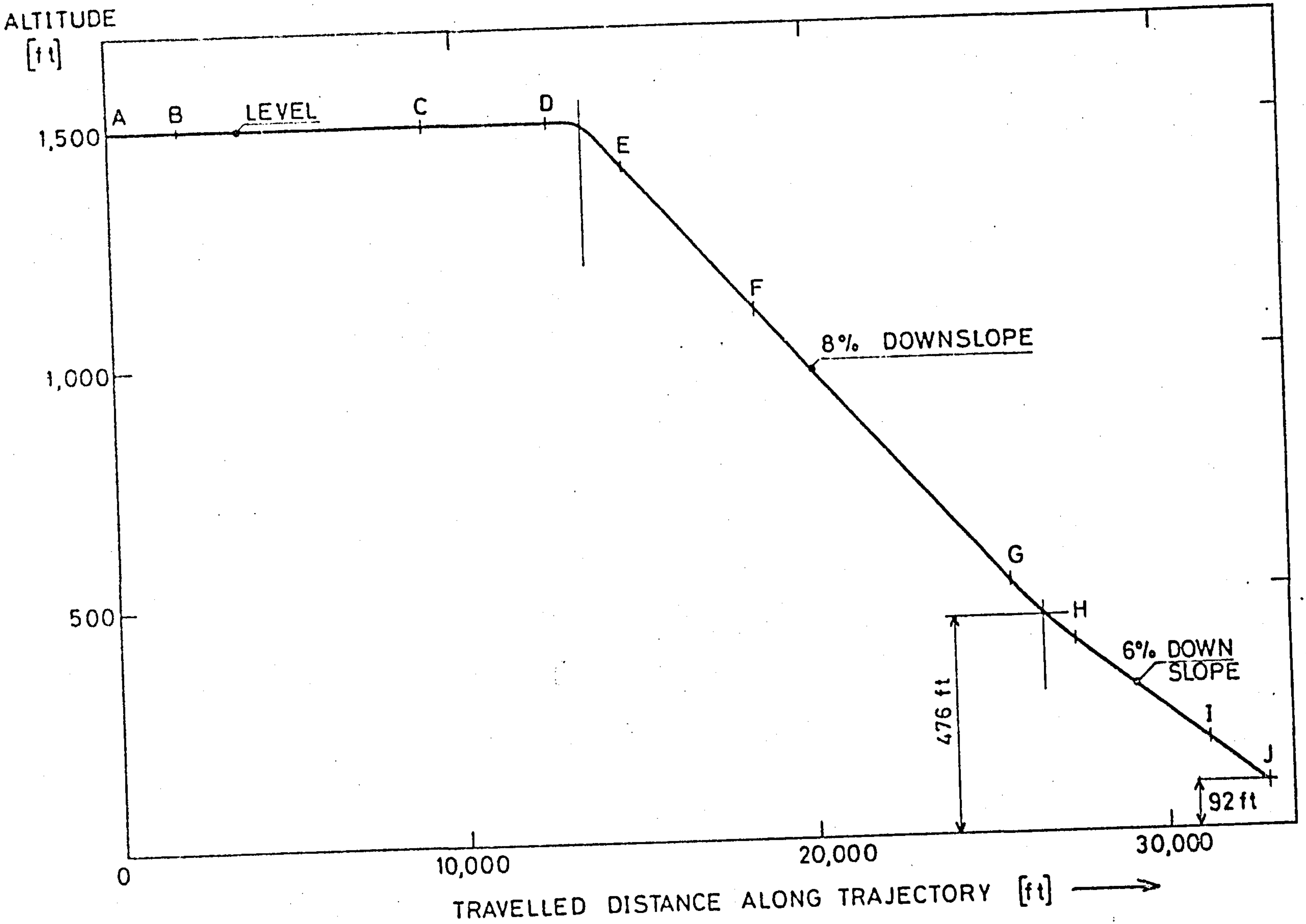

FIGURE 10. DESCENT PROFILE OF DESIRED TRAJECTORY.

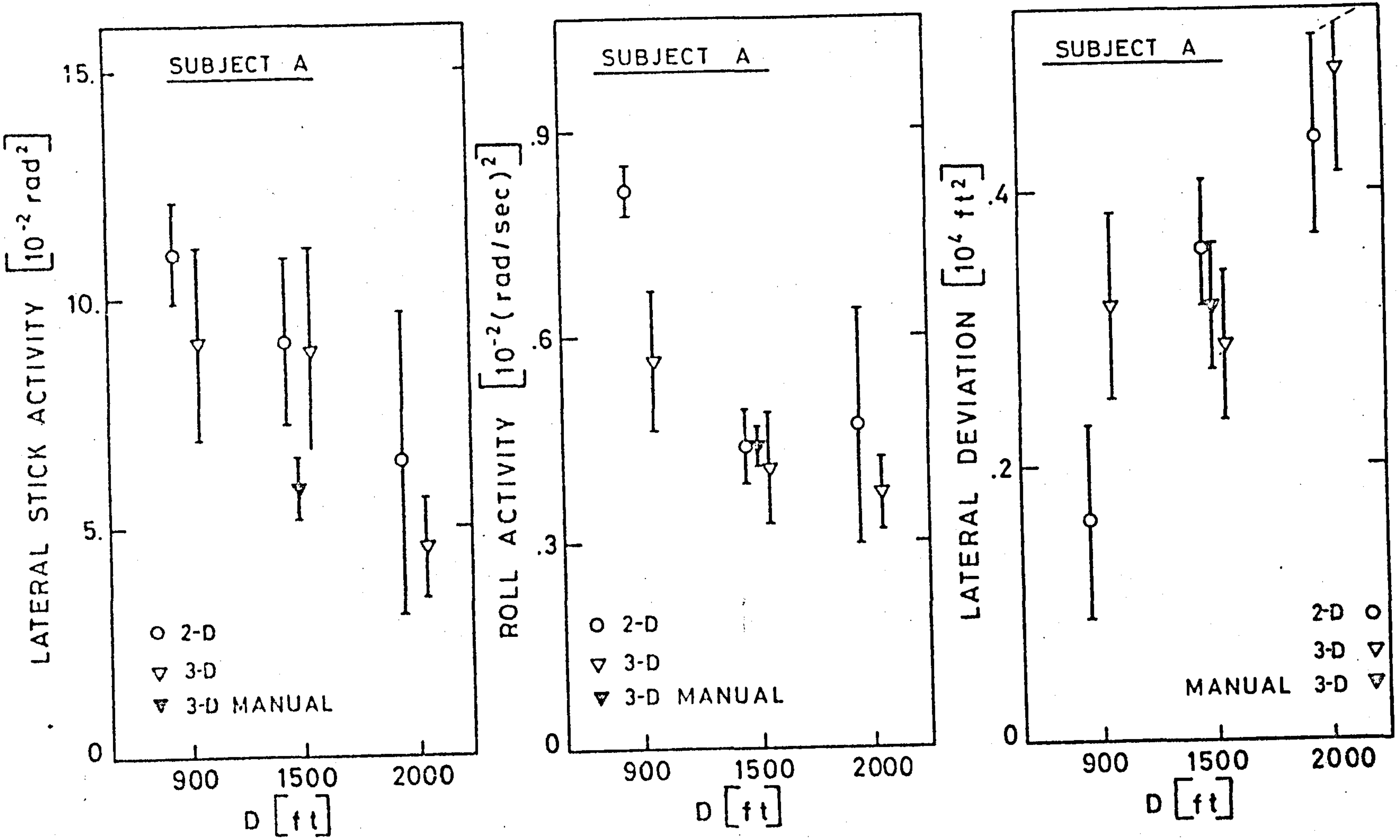

FIGURE 11. LATERAL RESULTS OF TRAJECTORY FOLLOWING; SUBJECT A.

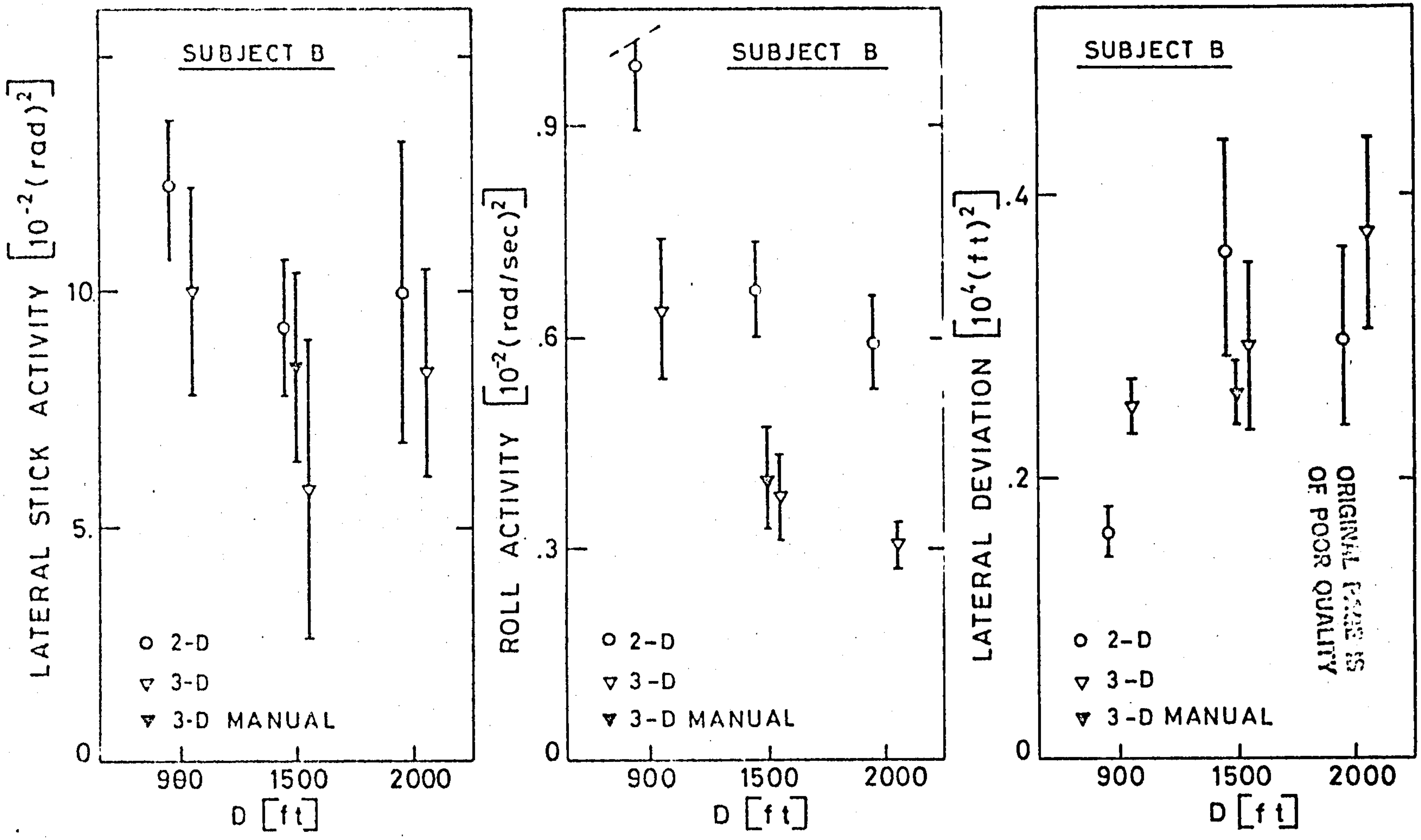

FIGURE 12. LATERAL RESULTS OF TRAJECTORY FOLLOWING; SUBJECT B.

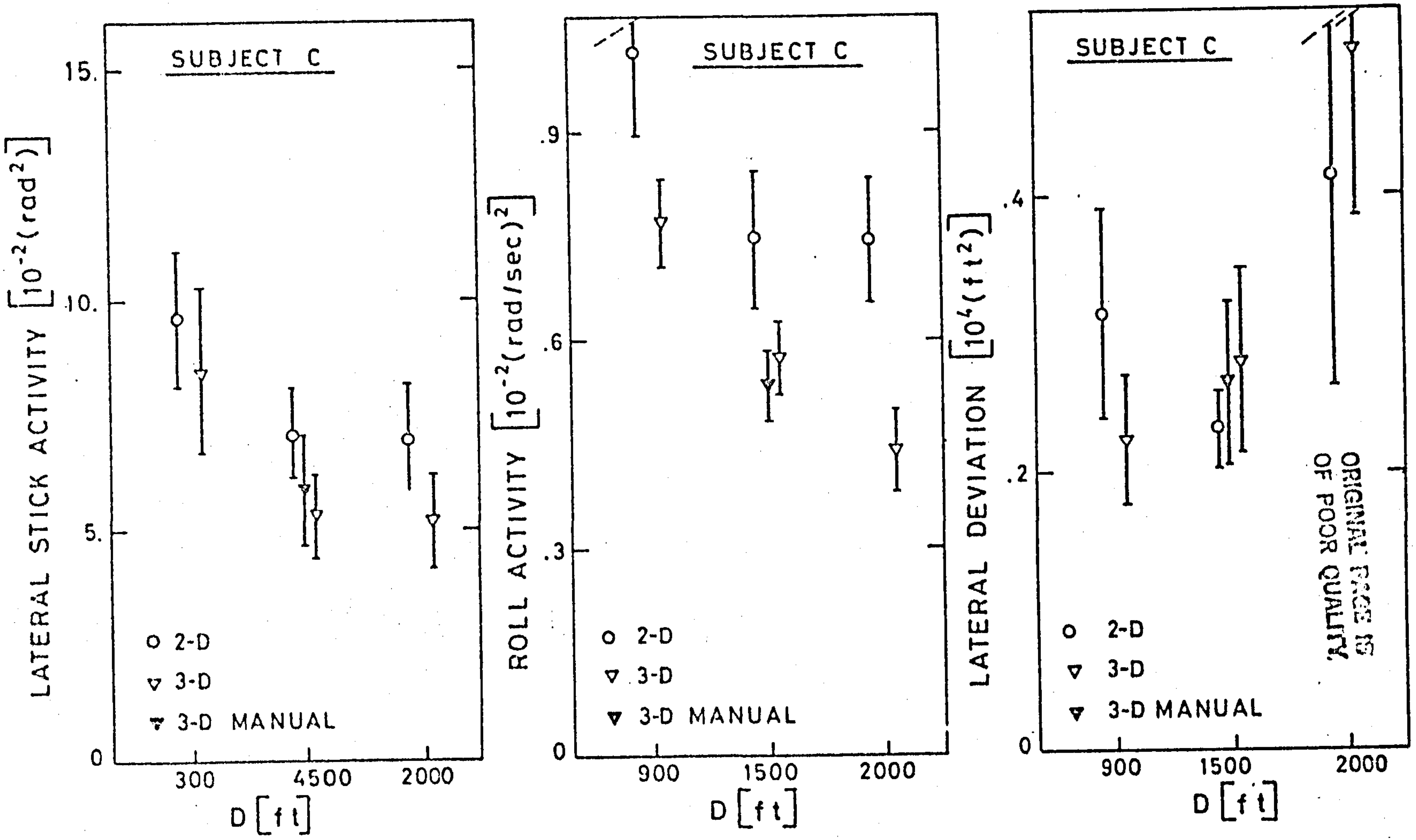

FIGURE 13. LATERAL RESULTS OF TRAJECTORY FOLLOWING; SUBJECT C.

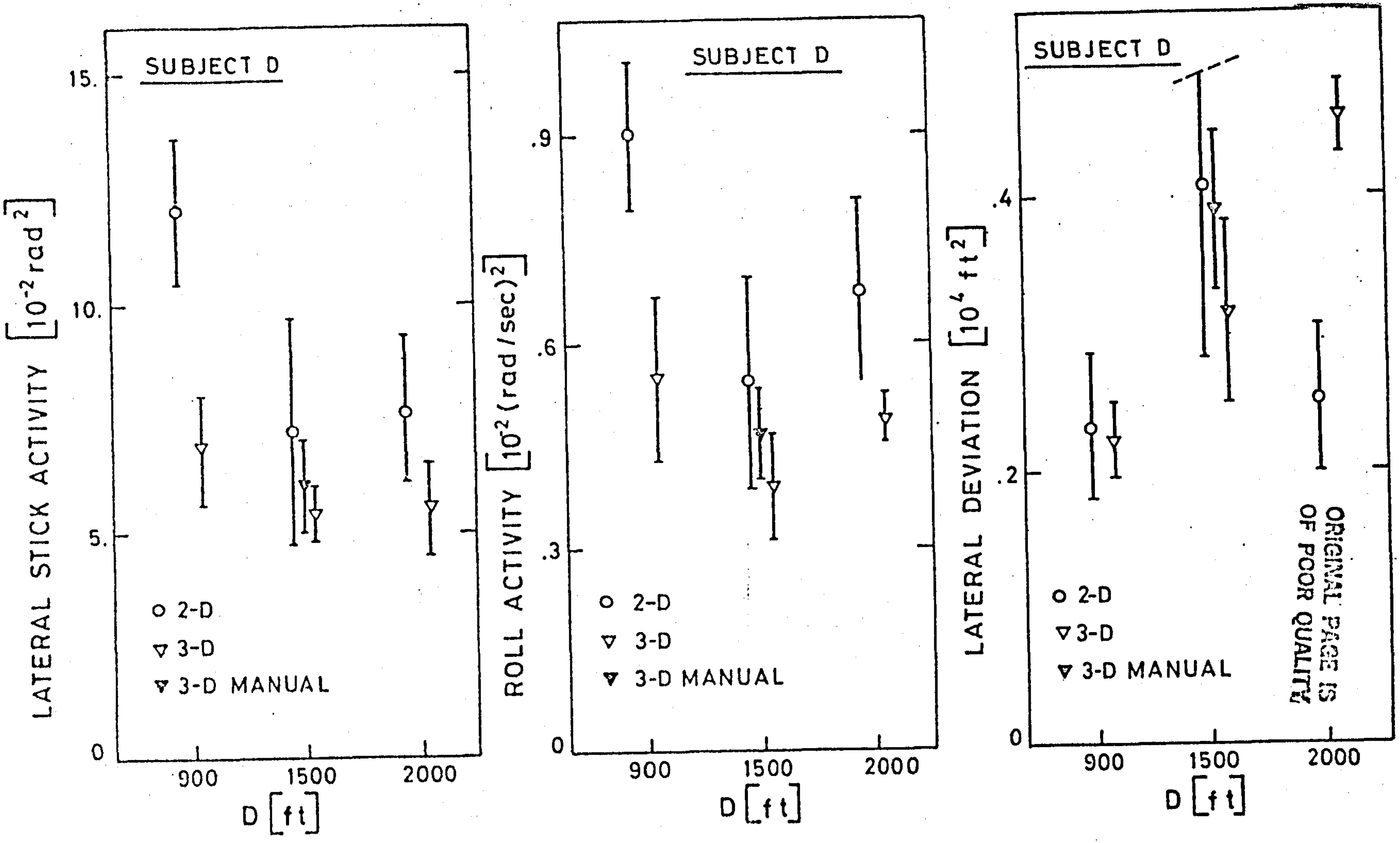

FIGURE 14. LATERAL RESULTS OF TRAJECTORY FOLLOWING; SUBJECT D.

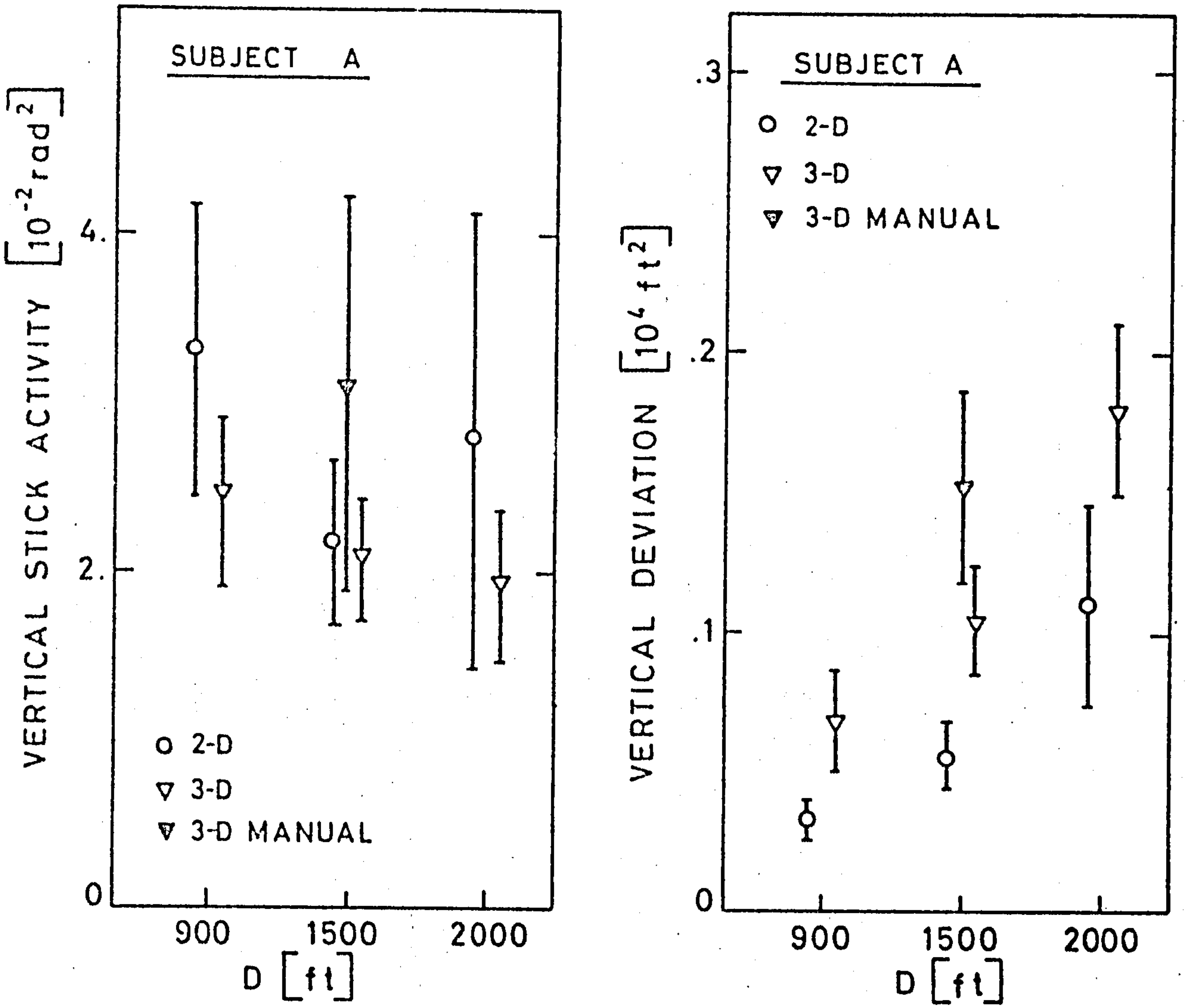

FIGURE 15. Vertical results of trajectory following; subject A.

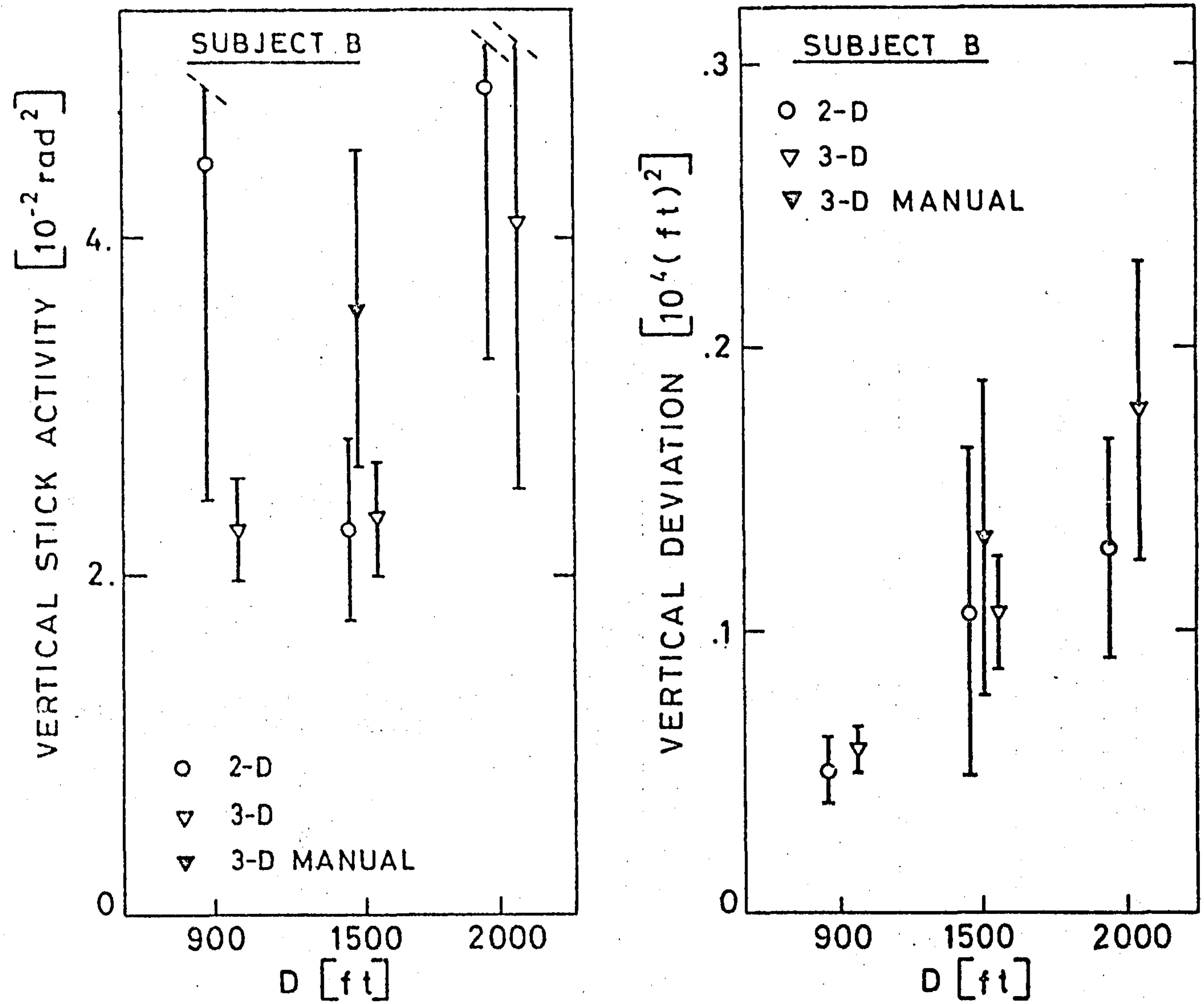

FIGURE 16. Vertical results of trajectory following; subject B.

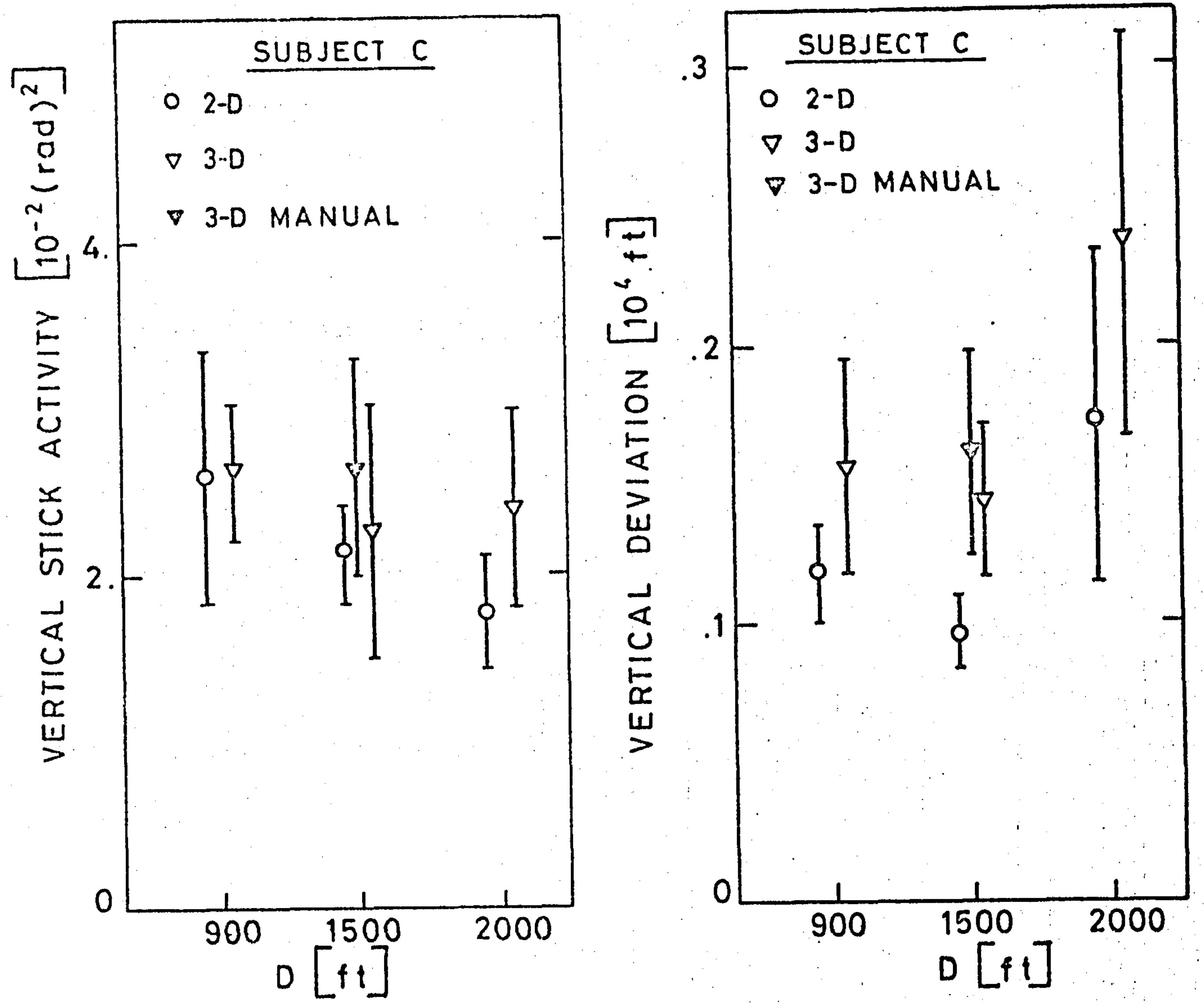

FIGURE 17. Vertical results of trajectory following; subject C.

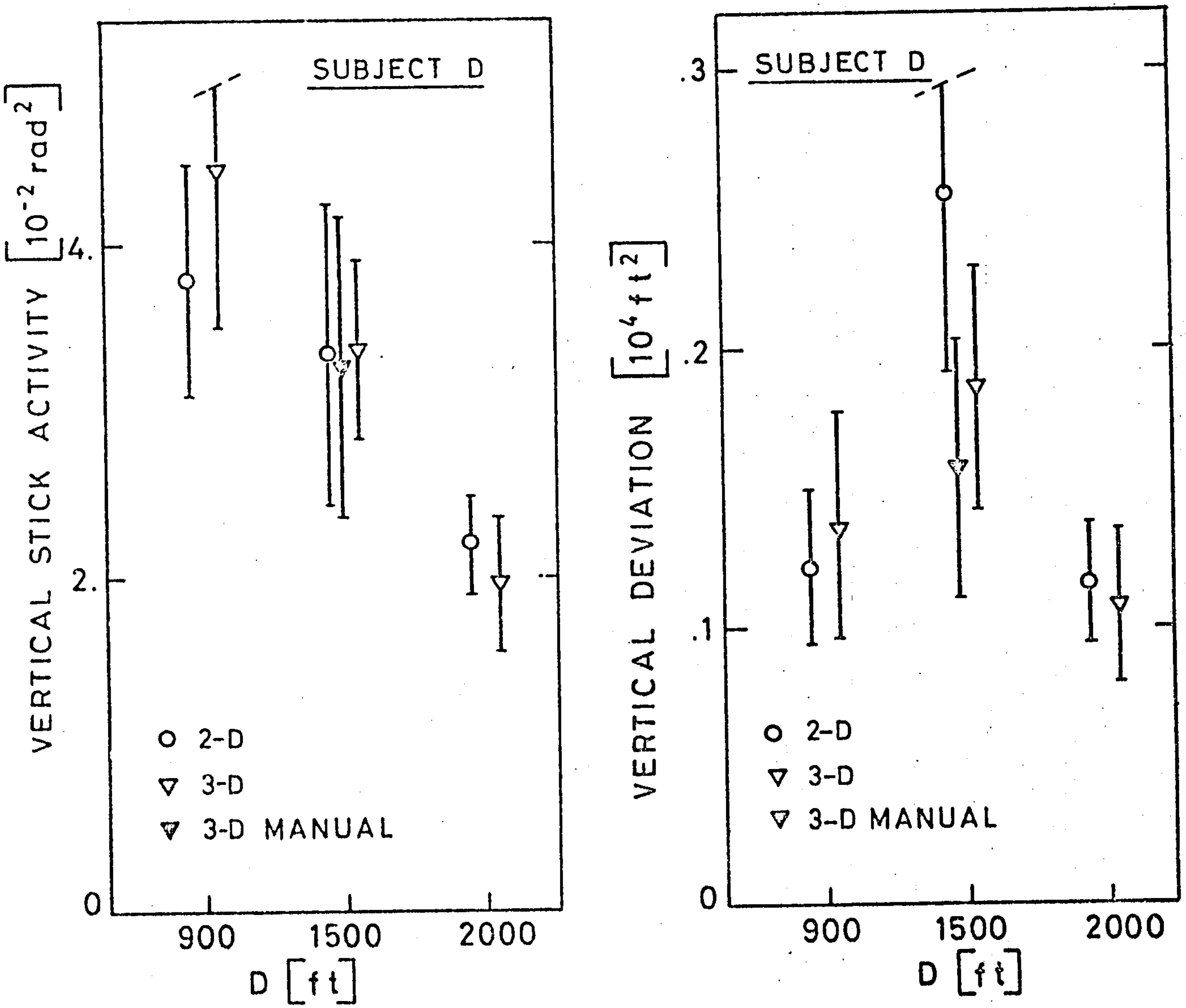

FIGURE 18. Vertical results of trajectory following; subject D.

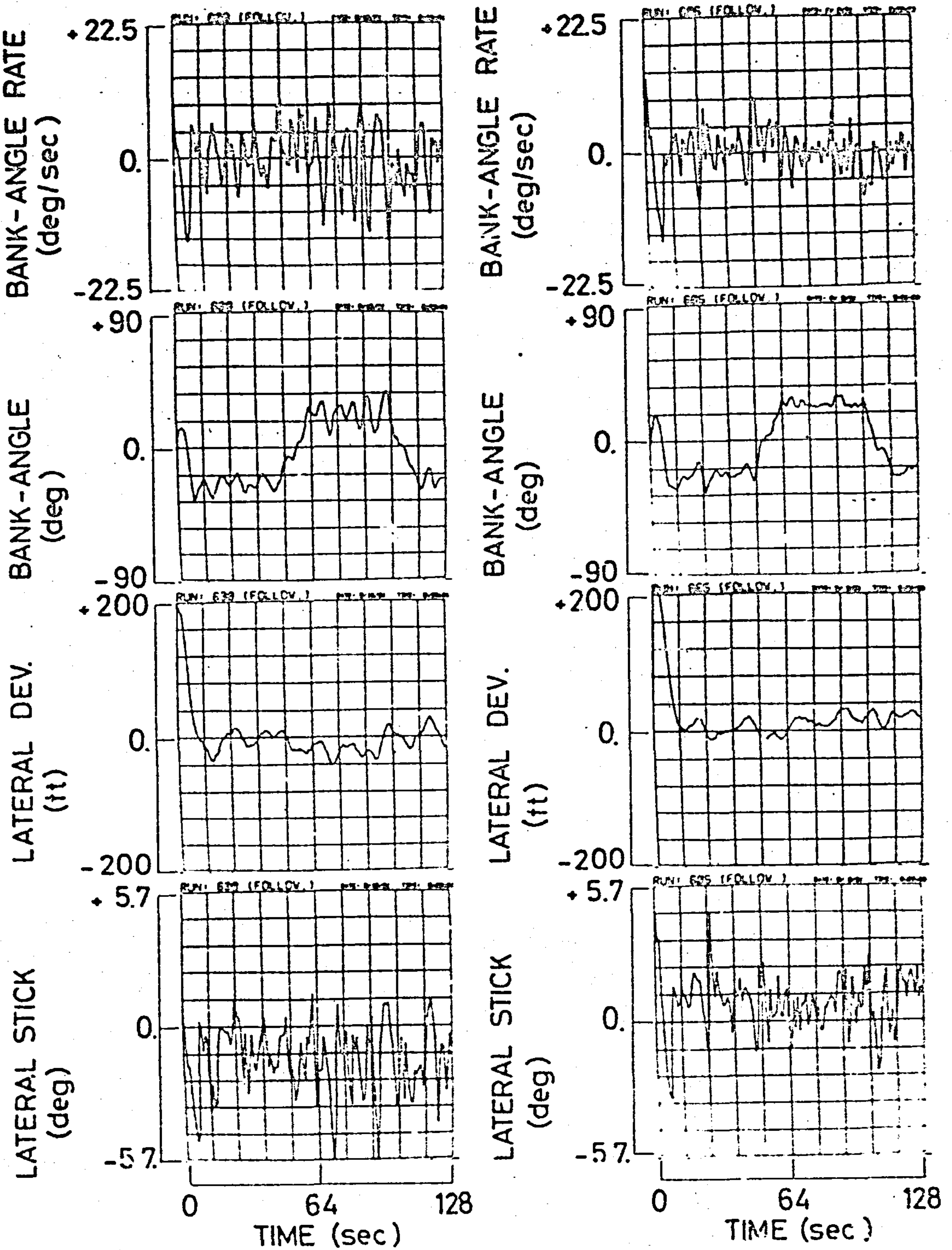

2-D PREDICTOR
D_0 = 900 ft

3-D PREDICTOR
D_0 = 900 ft

FIGURE 19. TIME-HISTORIES OF LATERAL RESPONSE FOR TRAJECTORY FOLLOWING; 3-D PERSPECTIVE SYMBOL COMPARED WITH 2-D PREDICTOR CROSS;

D_0 = 900 ft; SUBJECT B.

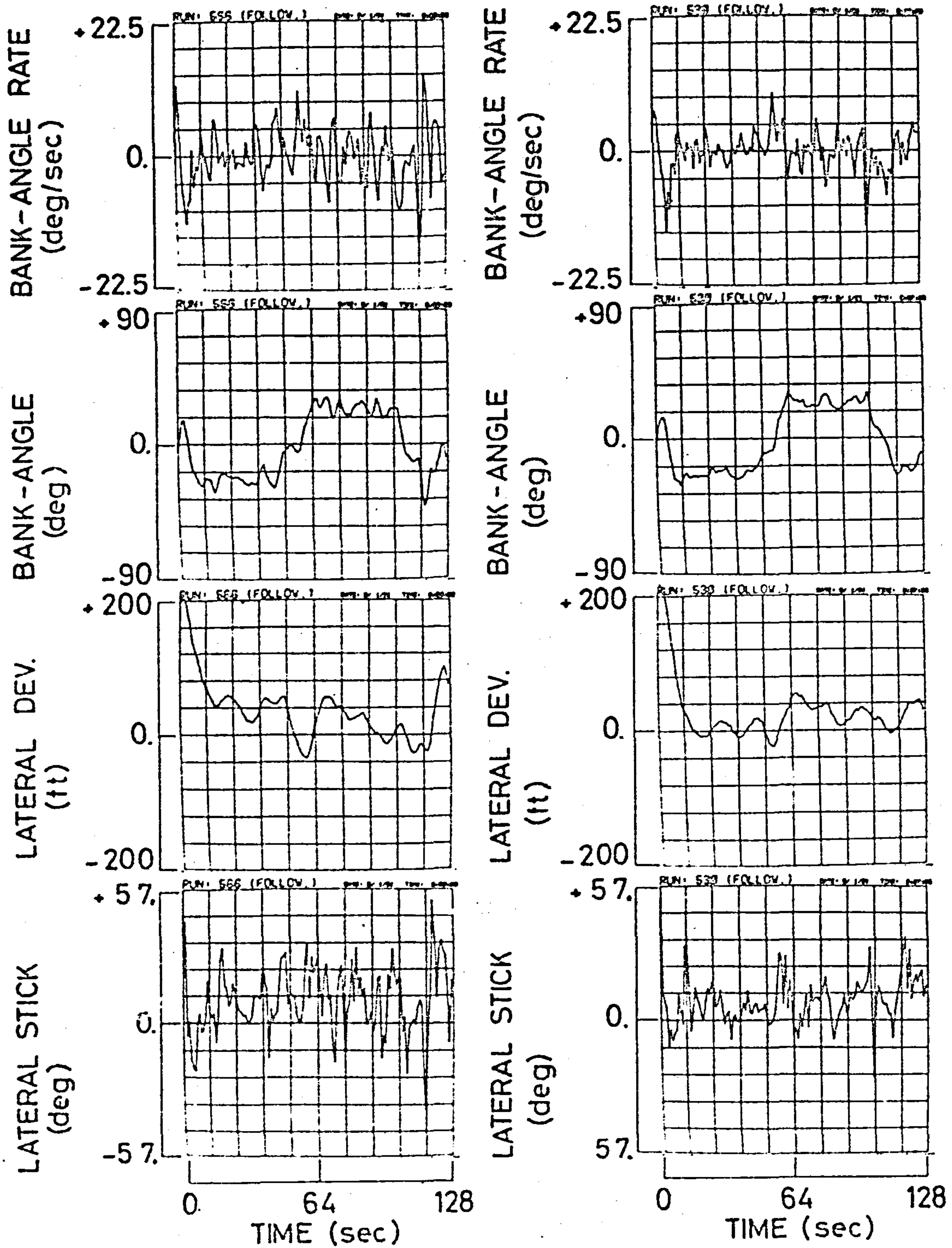

2-D PREDICTOR
D_o = 1500 ft

3-D PREDICTOR
D_o = 1500 ft

FIGURE 20. TIME-HISTORIES OF LATERAL RESPONSE FOR TRAJECTORY FOLLOWING; 3-D PERSPECTIVE SYMBOL COMPARED WITH 2-D PREDICTOR CROSS;

D_0 = 1500 ft; SUBJECT B.

C-2

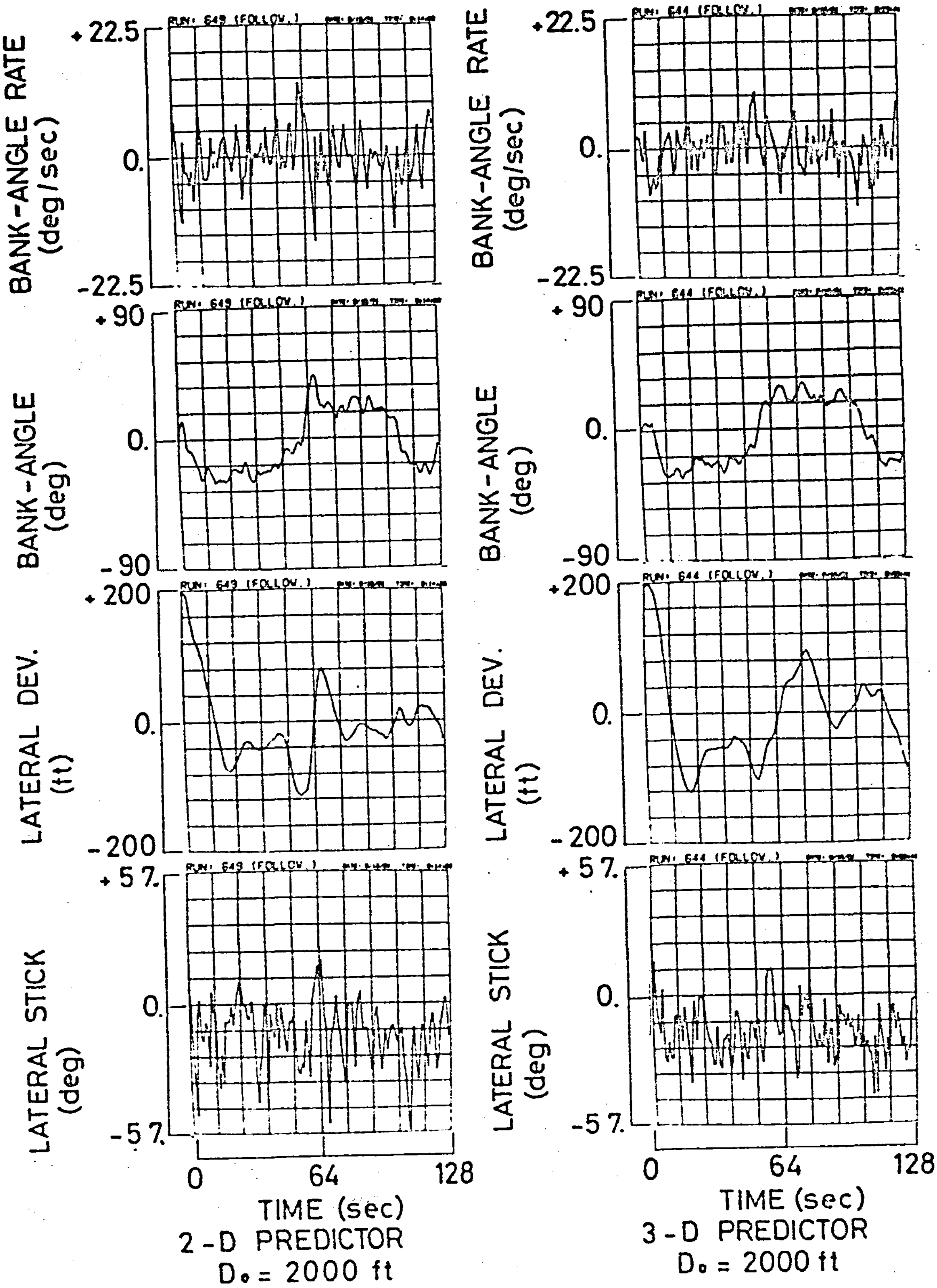

FIGURE 21. TIME-HISTORIES OF LATERAL RESPONSE FOR TRAJECTORY FOLLOWING; 3-D PERSPECTIVE SYMBOL COMPARED WITH 2-D PREDICTOR CROSS; D_0 = 2000 ft; SUBJECT B.

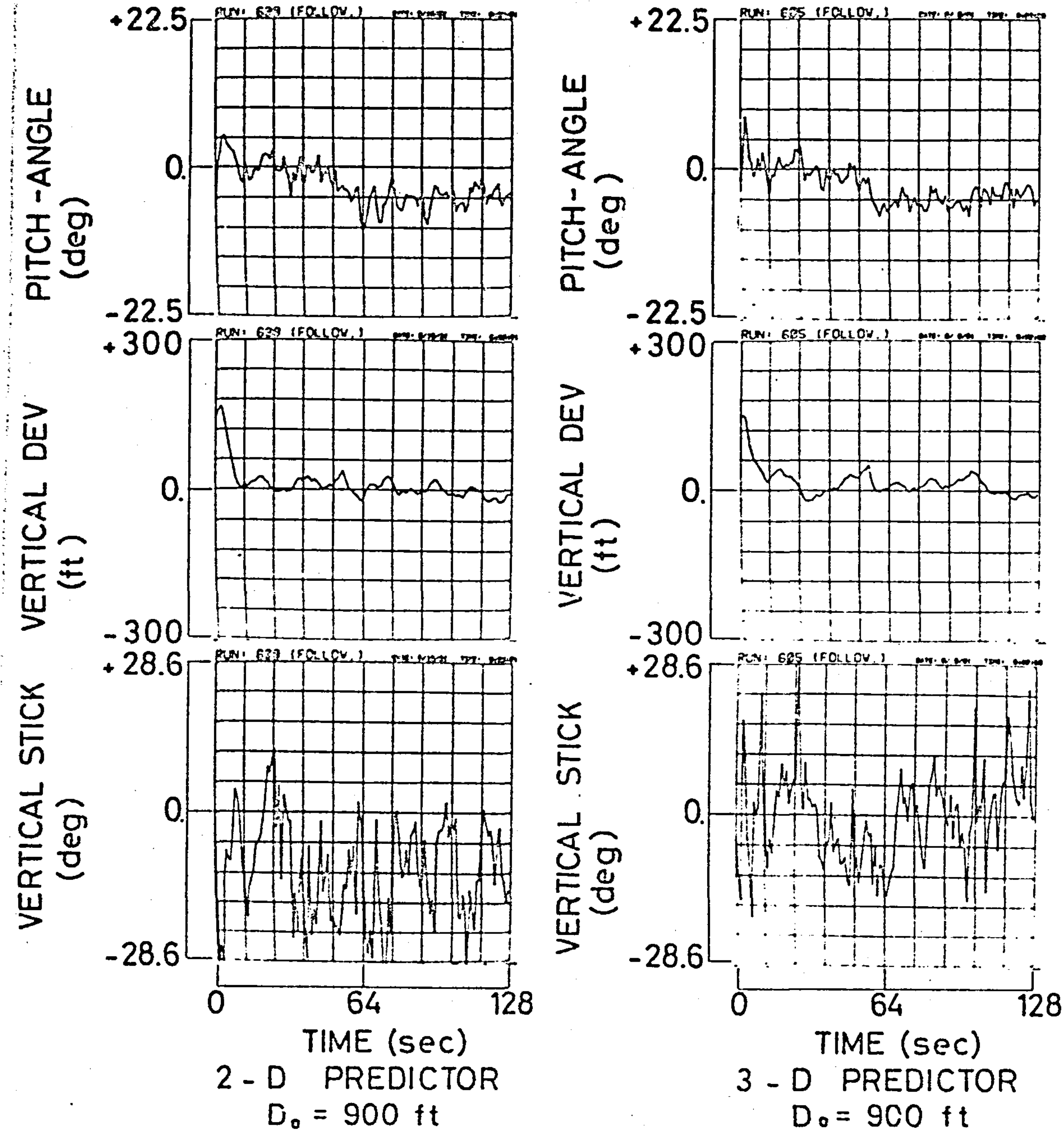

FIGURE 22. TIME-HISTORIES OF VERTICAL RESPONSE FOR TRAJECTORY FOLLOWING; 3-D PERSPECTIVE SYMBOL COMPARED WITH 2-D PREDICTOR CROSS;

D_0 = 900 ft; SUBJECT B.

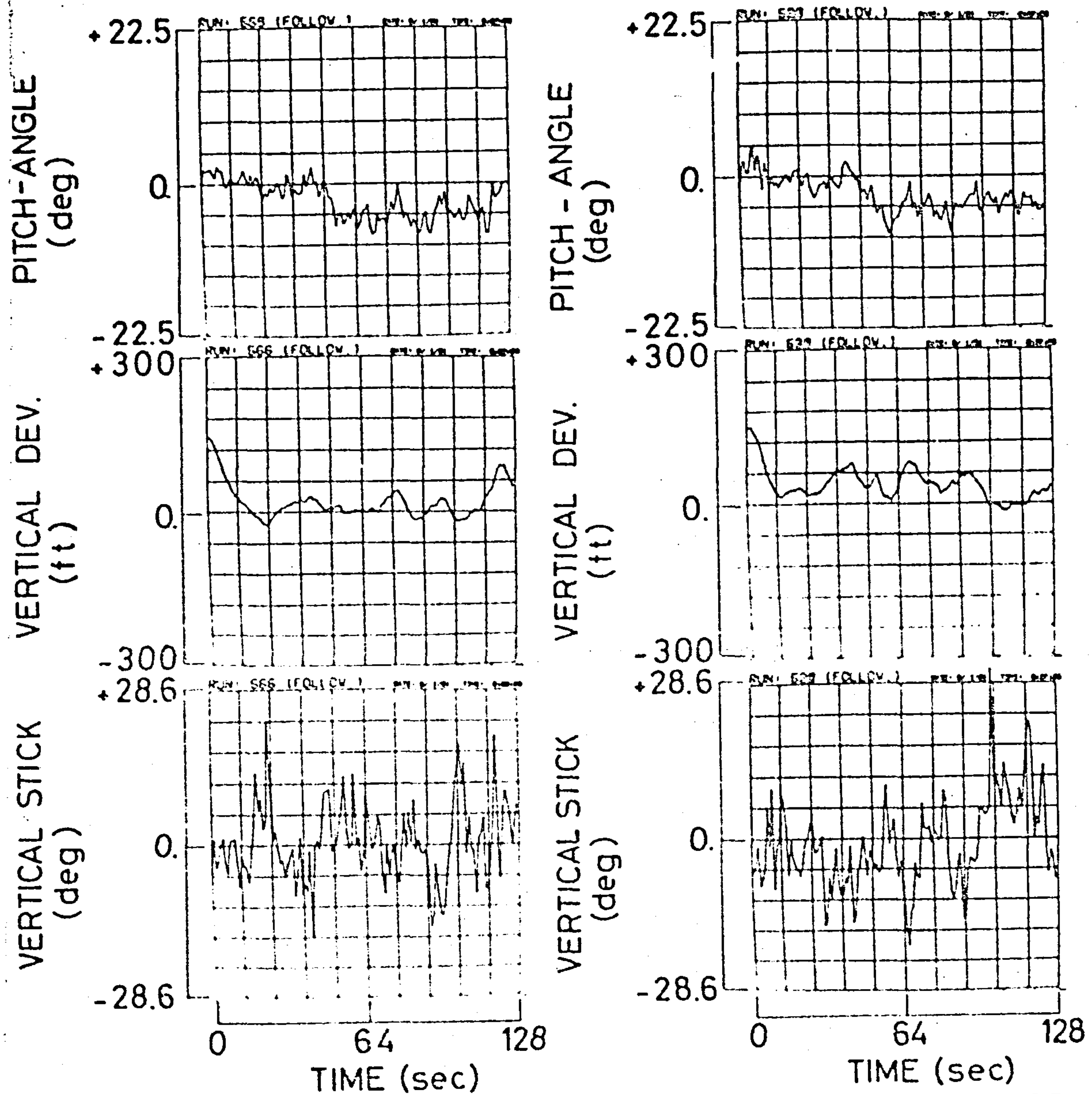

2 - D PREDICTOR
$D_o = 1500$ ft

3 - D PREDICTOR
$D_o = 1500$ ft

FIGURE 23. TIME-HISTORIES OF VERTICAL RESPONSE FOR TRAJECTORY FOLLOWING; 3-D PERSPECTIVE SYMBOL COMPARED WITH 2-D PREDICTOR CROSS; D_o = 1500 ft; SUBJECT B.

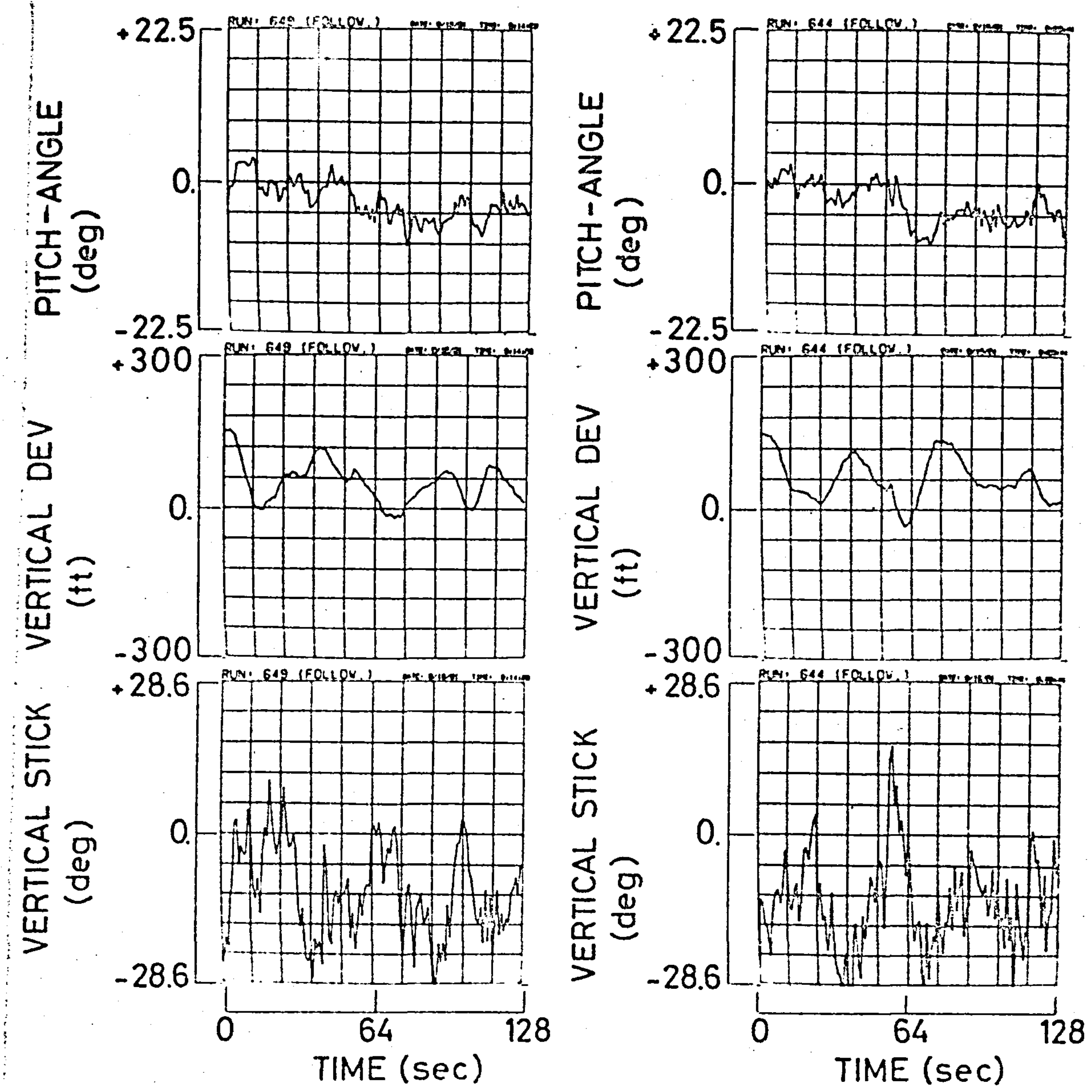

2 - D PREDICTOR
D_0 = 2000 ft

3 - D PREDICTOR
D_0 = 2000 ft

FIGURE 24. TIME-HISTORIES OF VERTICAL RESPONSE FOR TRAJECTORY FOLLOWING; 3-D PERSPECTIVE SYMBOL COMPARED WITH 2-D PREDICTOR CROSS;

D_0 = 2000 ft; SUBJECT B.

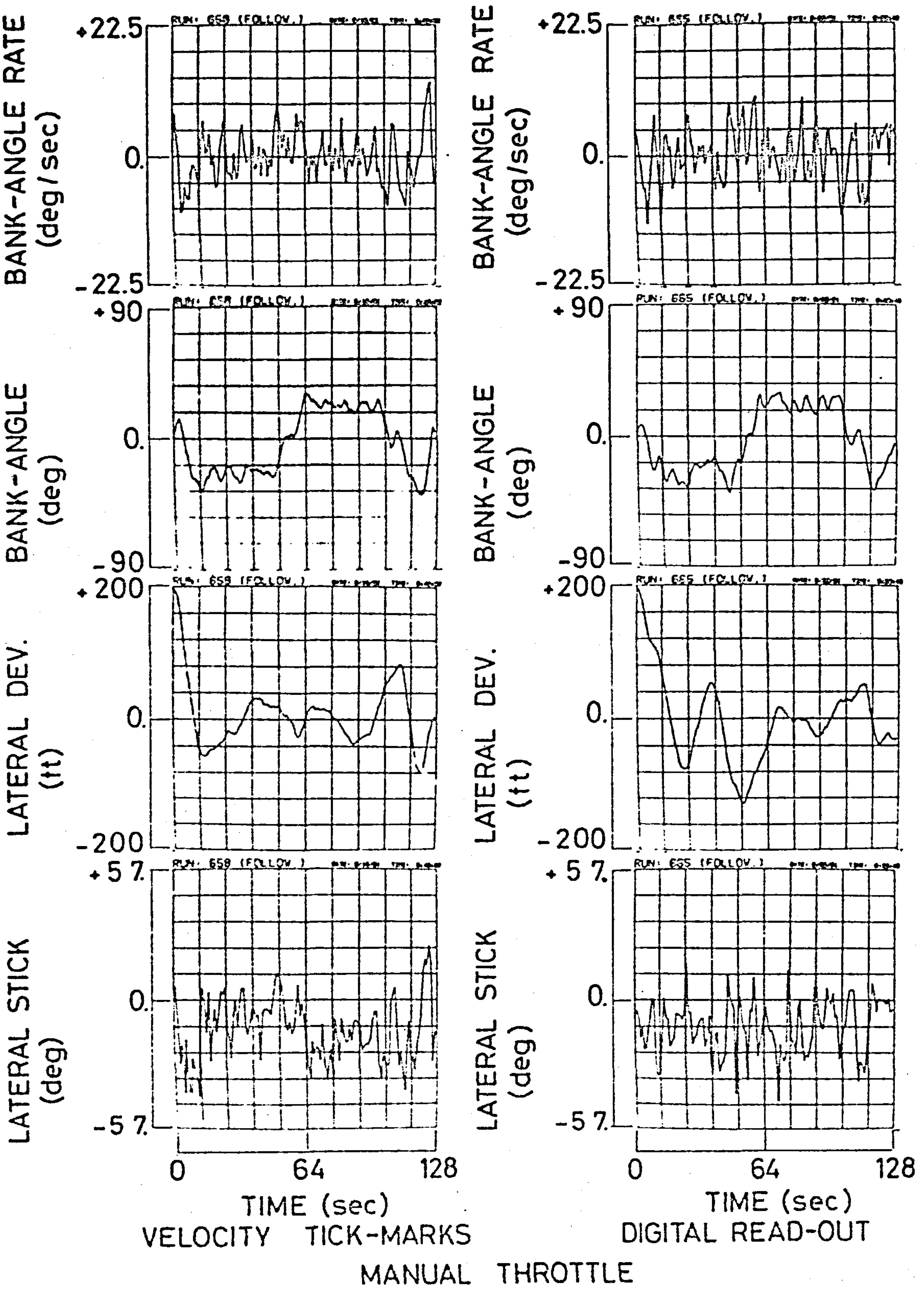

FIGURE 25. TIME-HISTORIES OF LATERAL RESPONSE FOR TRAJECTORY FOLLOWING; VELOCITY TICK-MARKS COMPARED WITH DIGITAL READ-OUT; SUBJECT B.

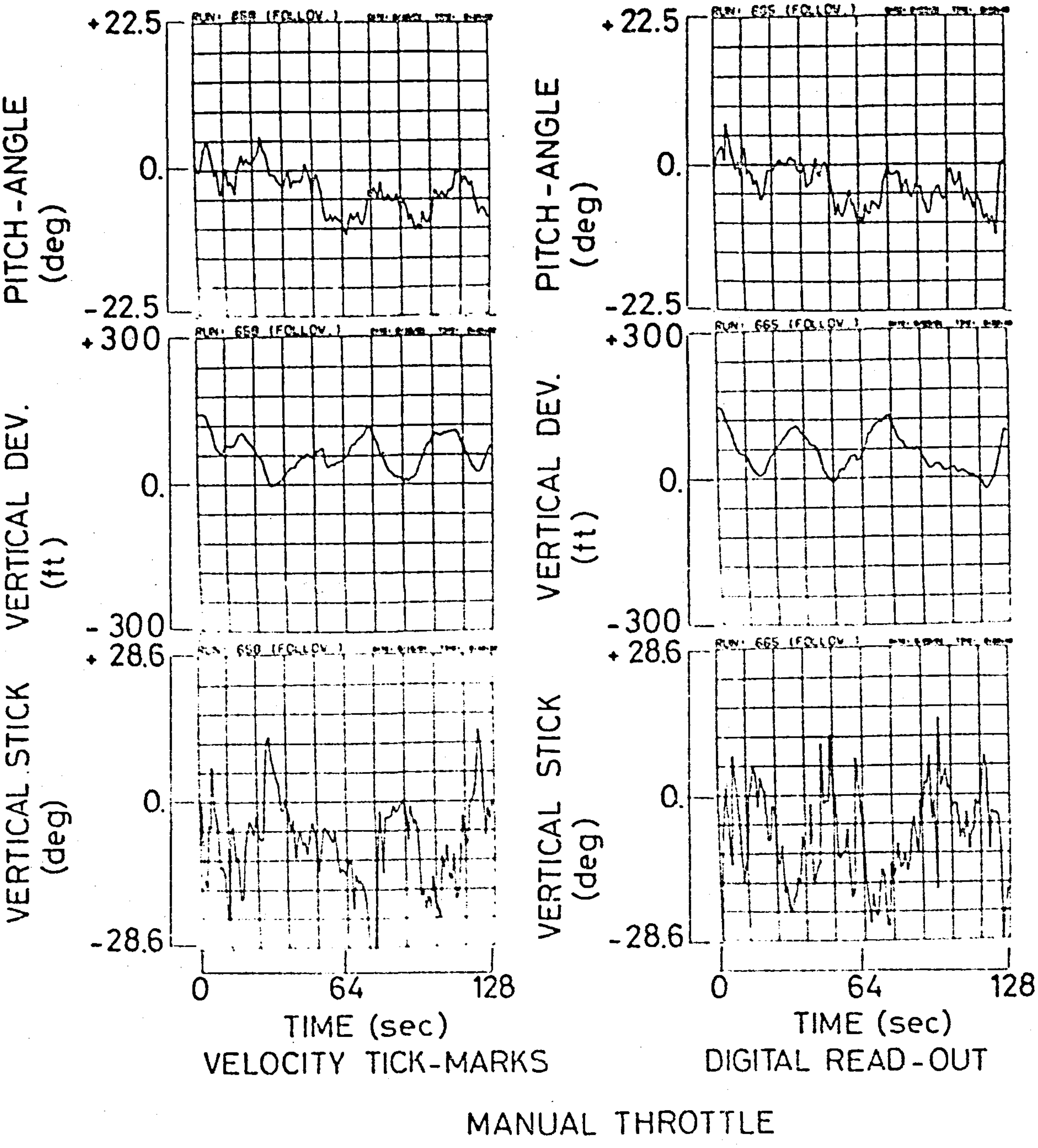

FIGURE 26. TIME-HISTORIES OF VERTICAL RESPONSE FOR TRAJECTORY FOLLOWING; VELOCITY TICK-MARKS COMPARED WITH DIGITAL READ-OUT; SUBJECT B.

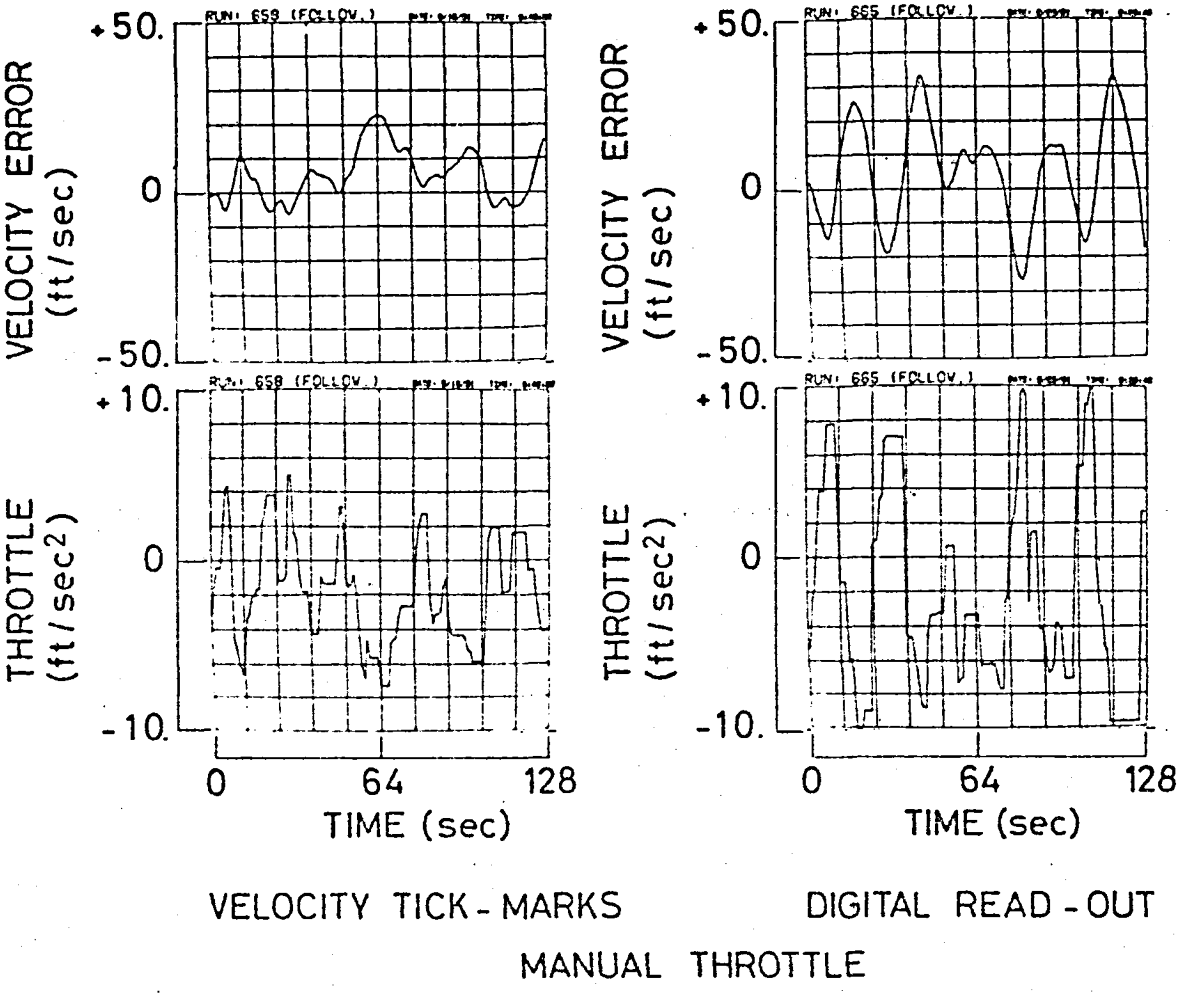

FIGURE 27. TIME-HISTORIES OF VELOCITY ERROR AND THROTTLE POSITION FOR TRAJECTORY FOLLOWING; VELOCITY TICK-MARKS COMPARED WITH DIGITAL READ-OUT; SUBJECT B.

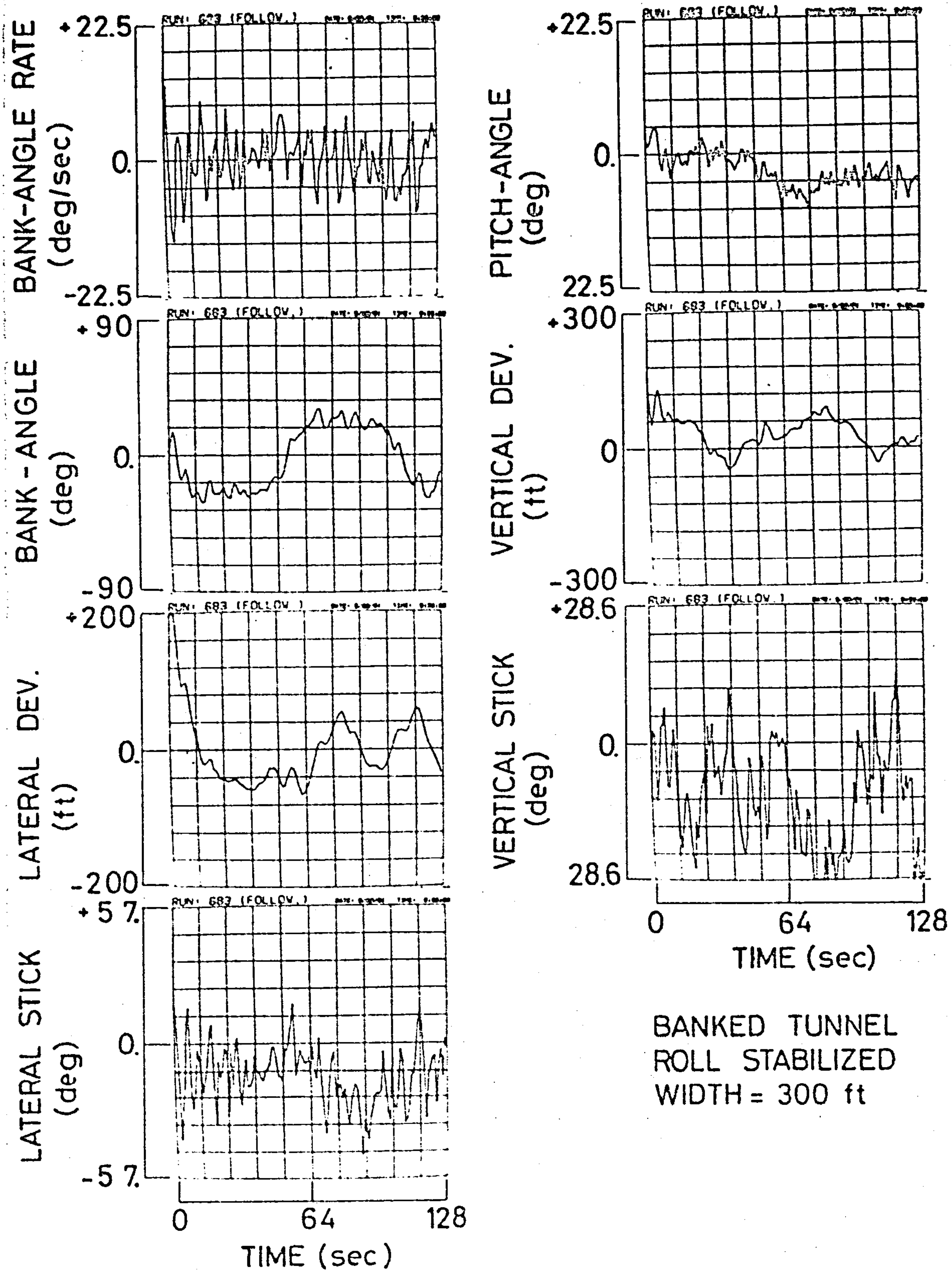

BANKED TUNNEL
ROLL STABILIZED
WIDTH = 300 ft

FIGURE 28. TIME HISTORIES OF TRAJECTORY FOLLOWING; BANKED TUNNEL; ROLL-STABILIZED VERSION; SUBJECT

ORIGINAL PAGE IS
OF POOR QUALITY

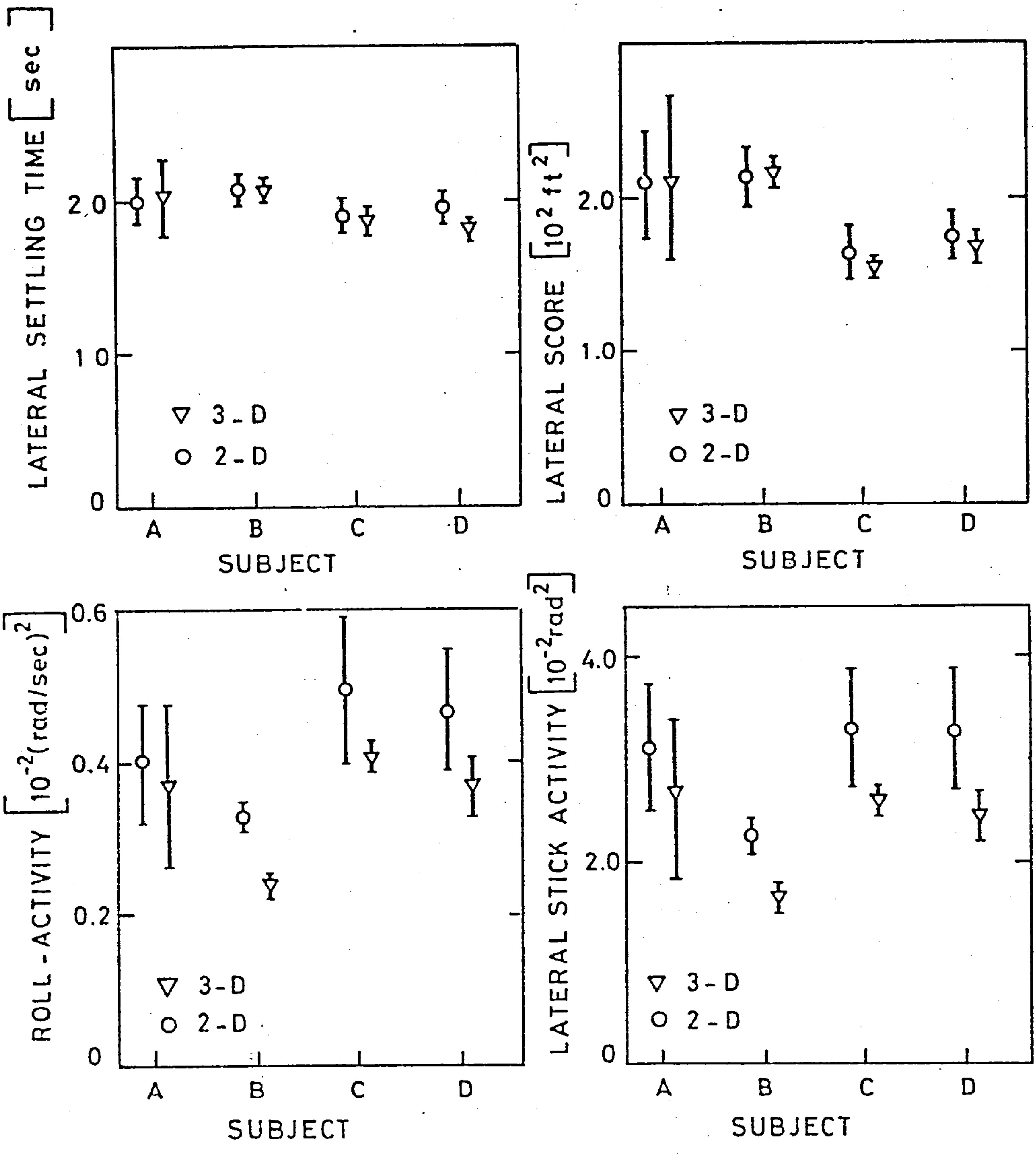

FIGURE 29. Lateral results of trajectory entry.

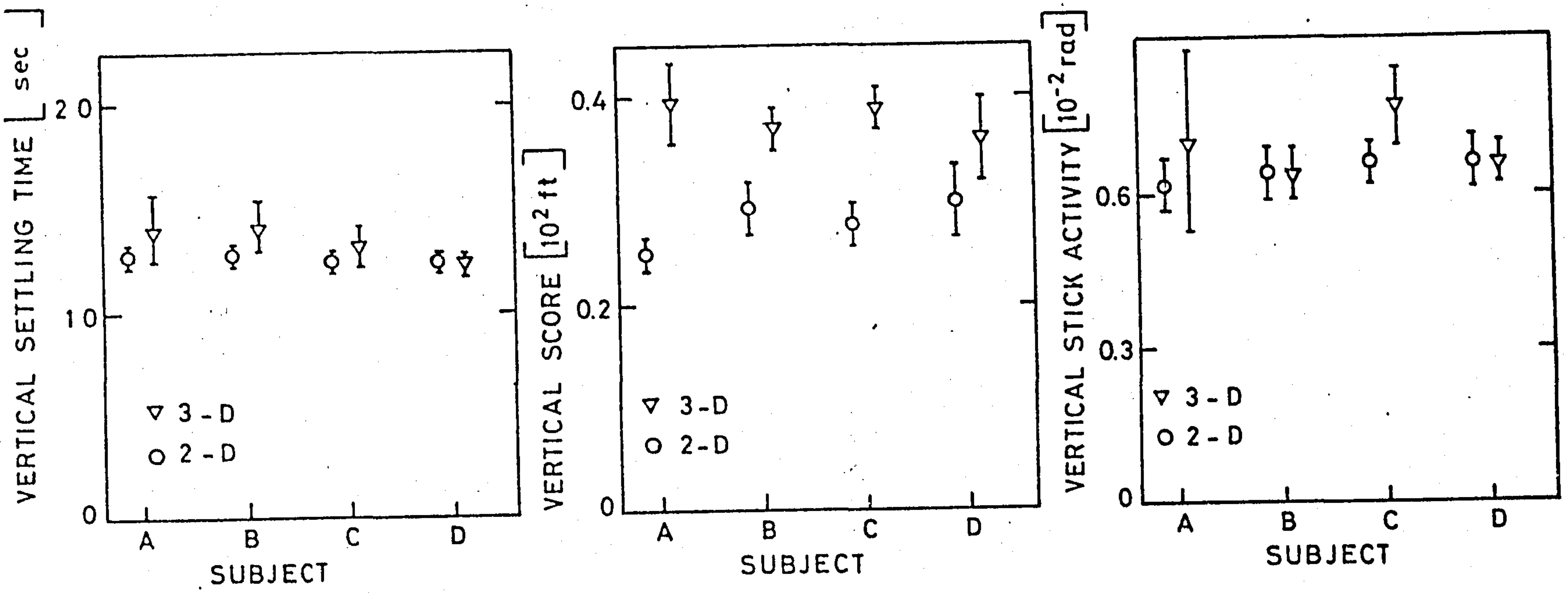

FIGURE 30. Vertical results of trajectory entry.

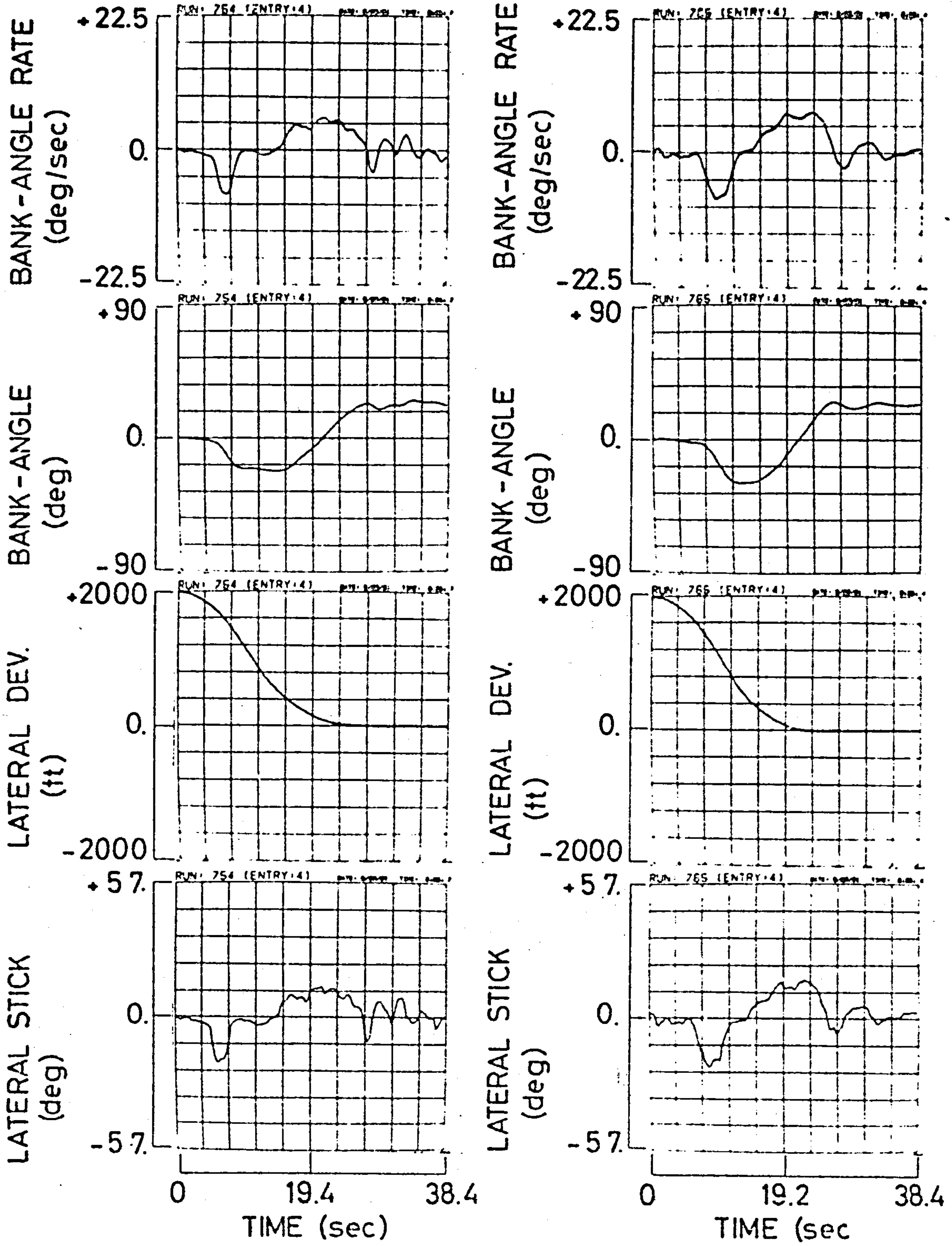

2-D PREDICTOR
D_o = 1500 ft

3-D PREDICTOR
D_o = 1500 ft

FIGURE 31. TIME-HISTORIES OF LATERAL RESPONSE FOR TRAJECTORY ENTRY; 3-D PERSPECTIVE SYMBOL COMPARED WITH 2-D PREDICTOR CROSS; SUBJECT B.

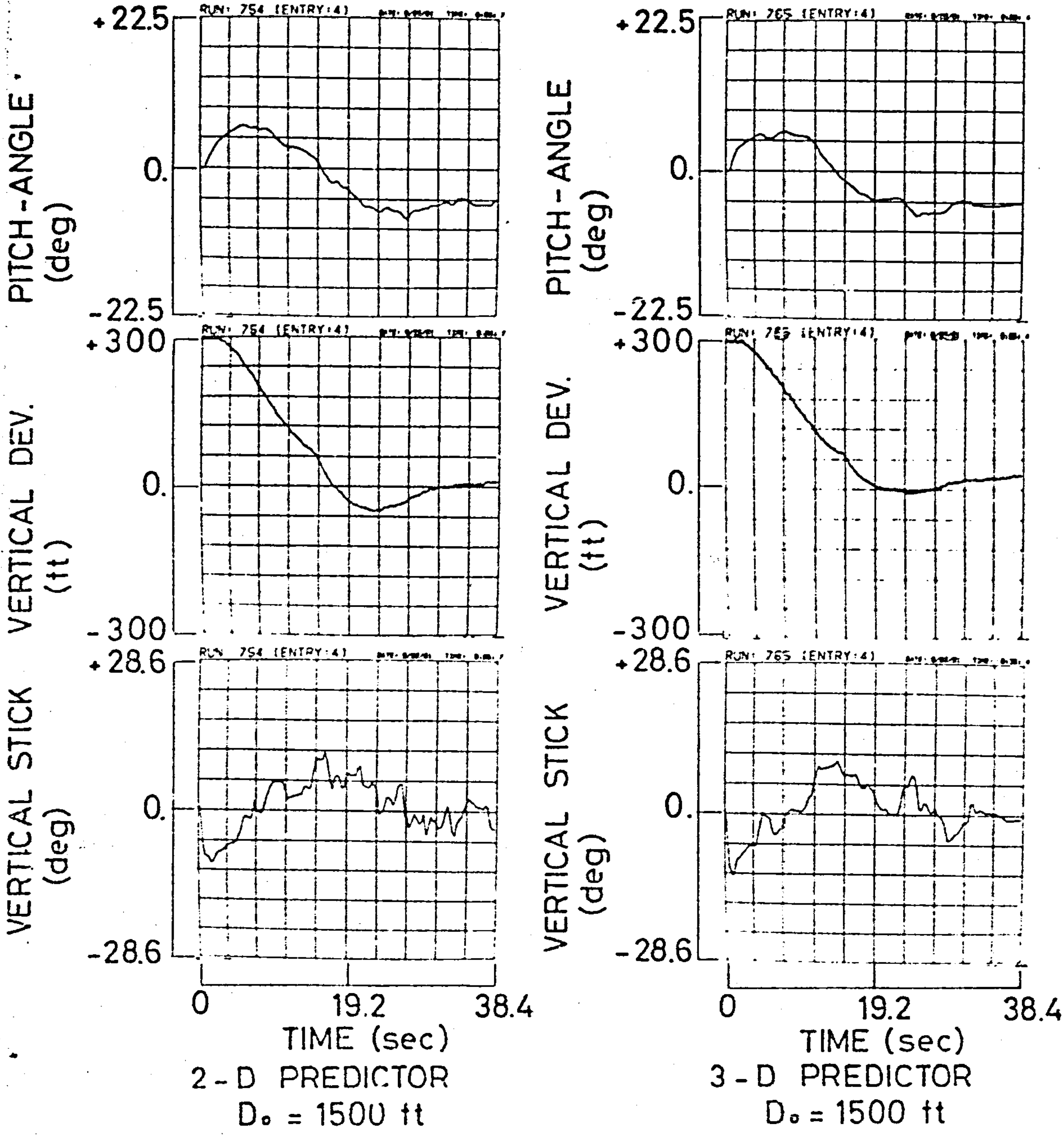

2-D PREDICTOR
$D_o = 1500$ ft

3-D PREDICTOR
$D_o = 1500$ ft

FIGURE 32. TIME-HISTORIES OF VERTICAL RESPONSE FOR TRAJECTORY ENTRY; 3-D PERSPECTIVE SYMBOL COMPARED WITH 2-D PREDICTOR CROSS; SUBJECT B.

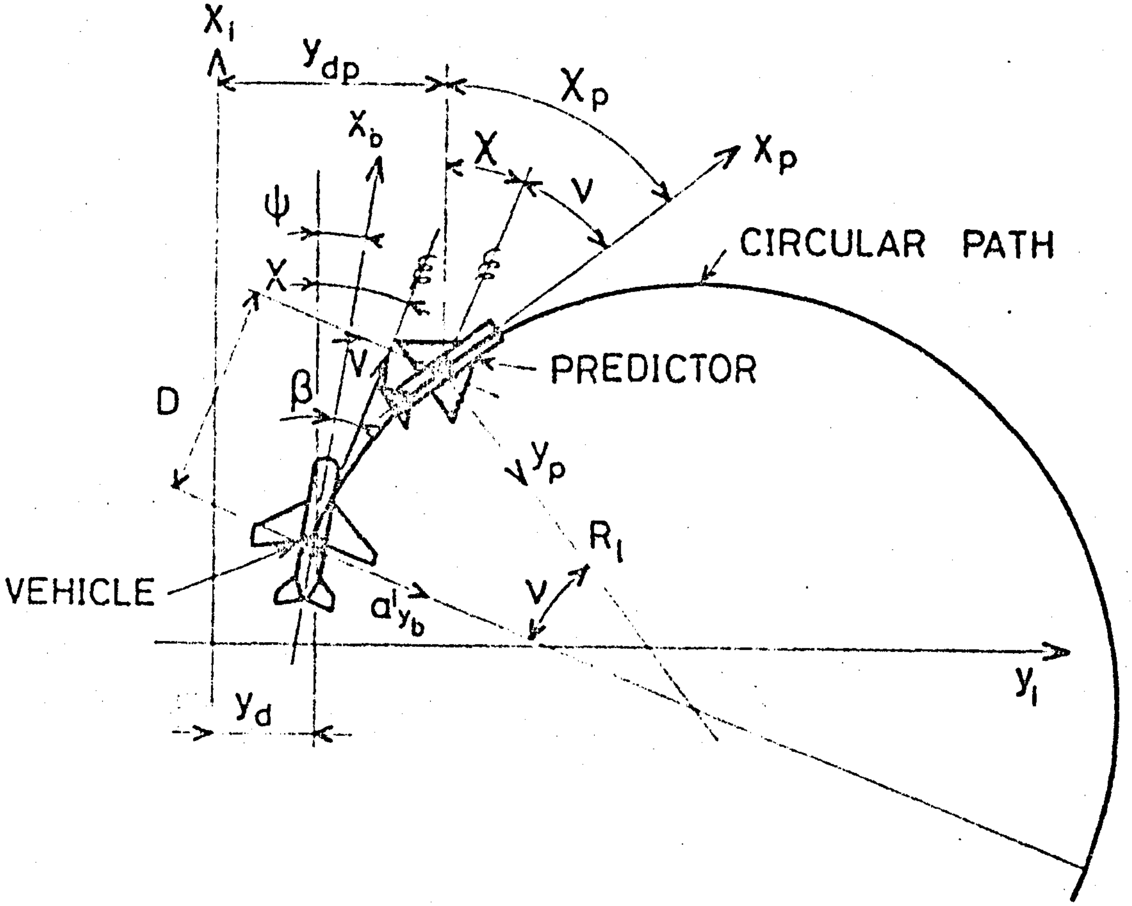

FIGURE 33. Horizontal situation of circular predicted vehicle path.

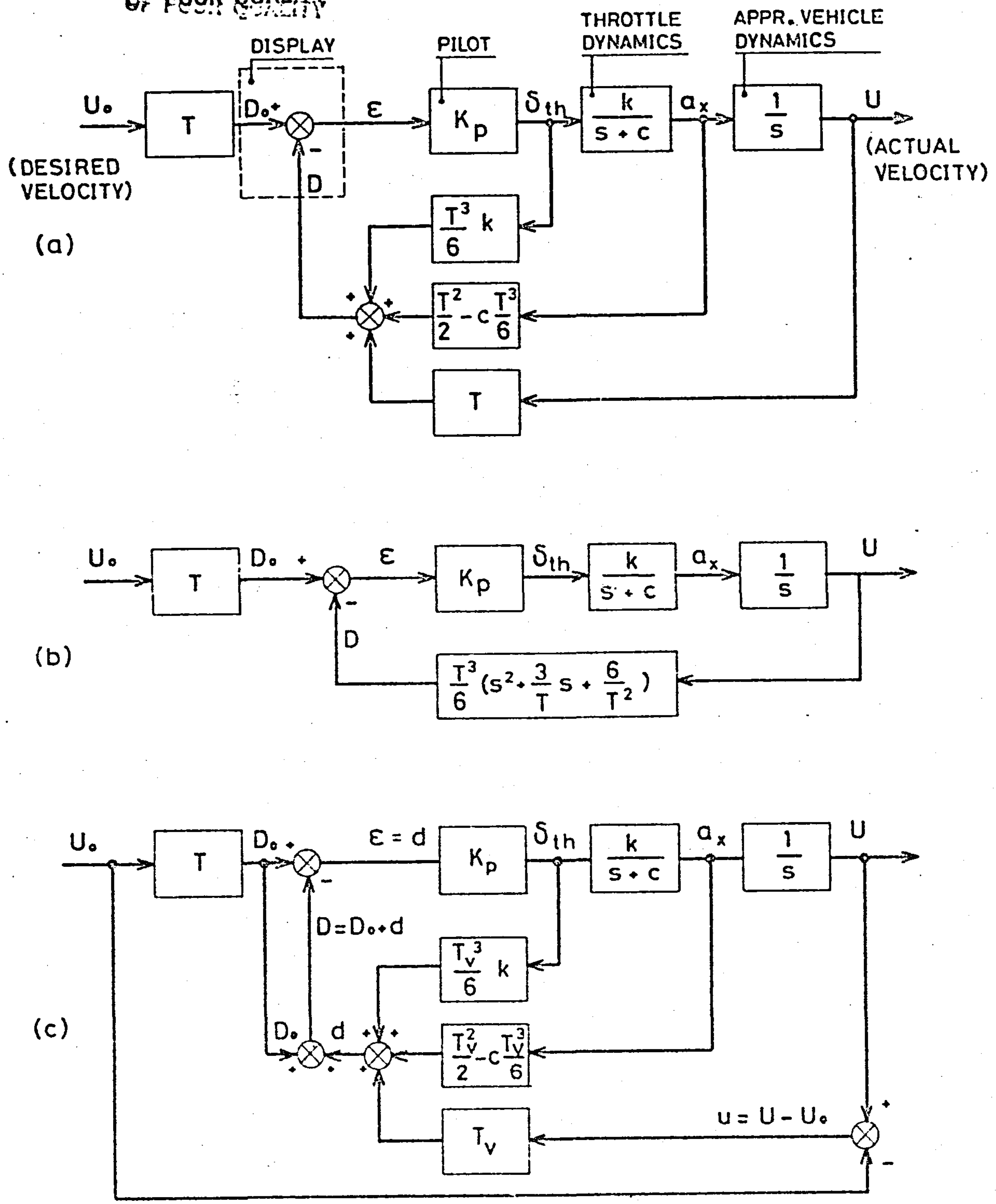

FIGURE 34. BLOCK-DIAGRAM OF FORWARD VELOCITY CONTROL:

(A) BASIC CONFIGURATION;

(B) BASIC CONFIGURATION REDUCED TO SINGLE-LOOP FEEDBACK SYSTEM;

(C) VELOCITY CONTROL WITH PREDICTOR TIME T_v.

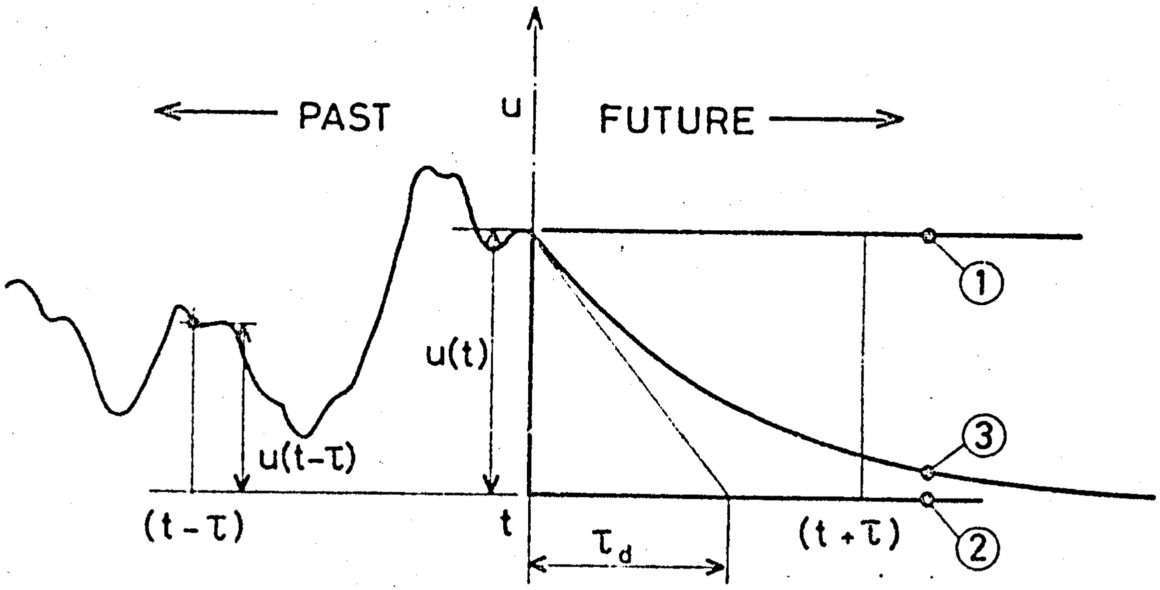

FIGURE 35. Assumptions for future values of control commands.

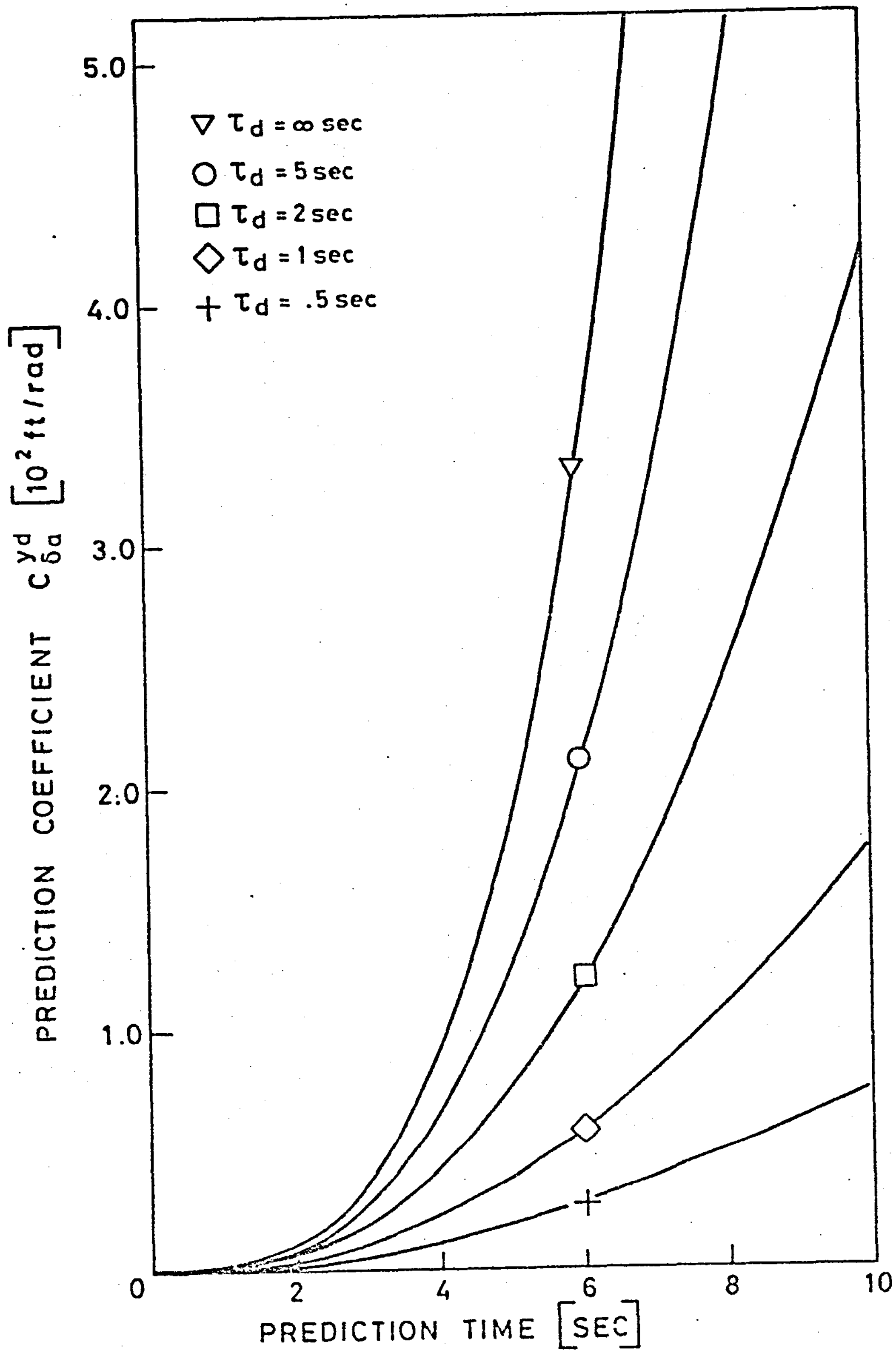

FIGURE 36. Lateral deviation prediction coefficient as a function of prediction time and for various values of τ_d.

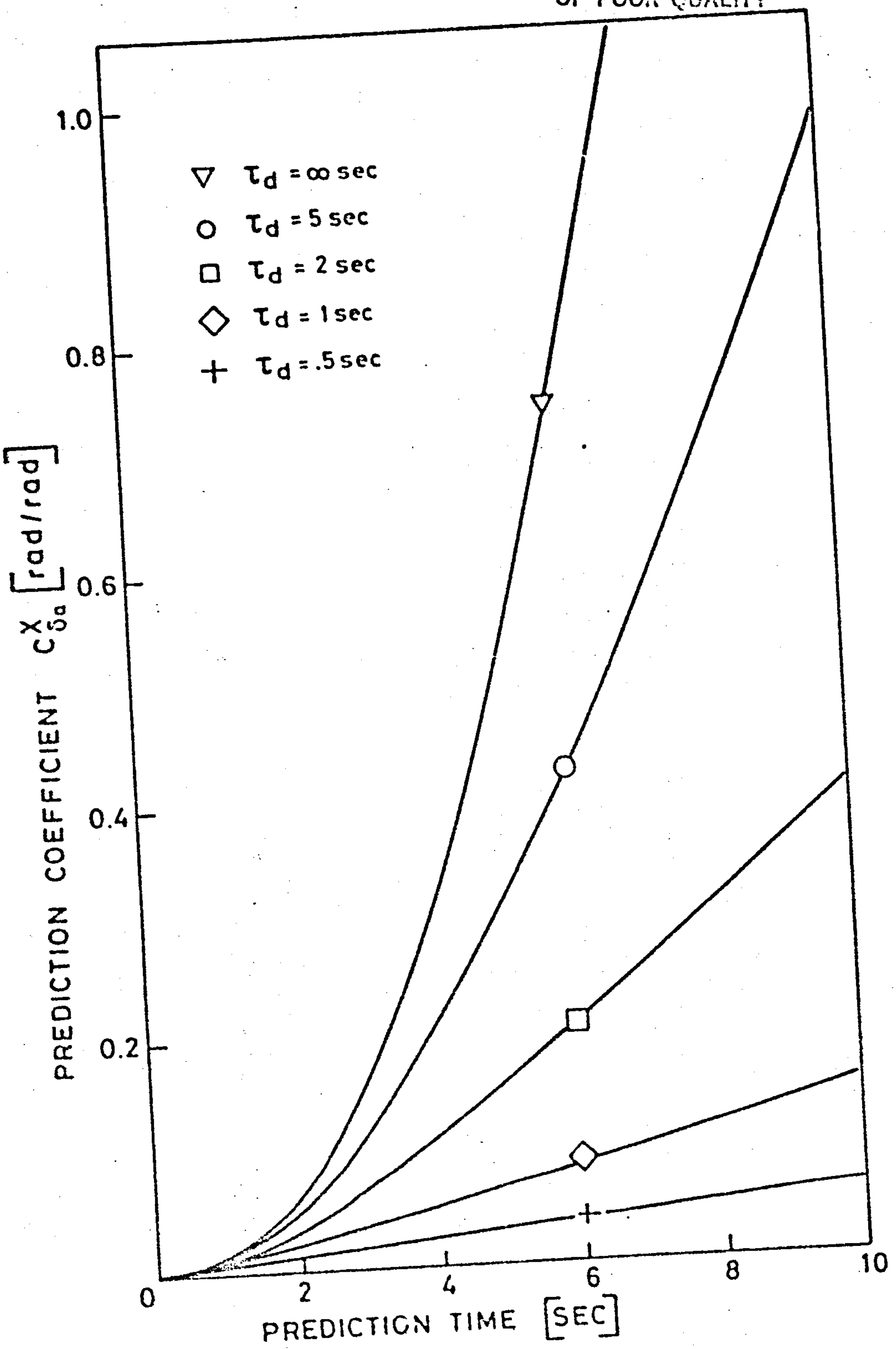

FIGURE 37. Lateral path-angle prediction coefficient as a function of prediction time and for various values of τ_d.

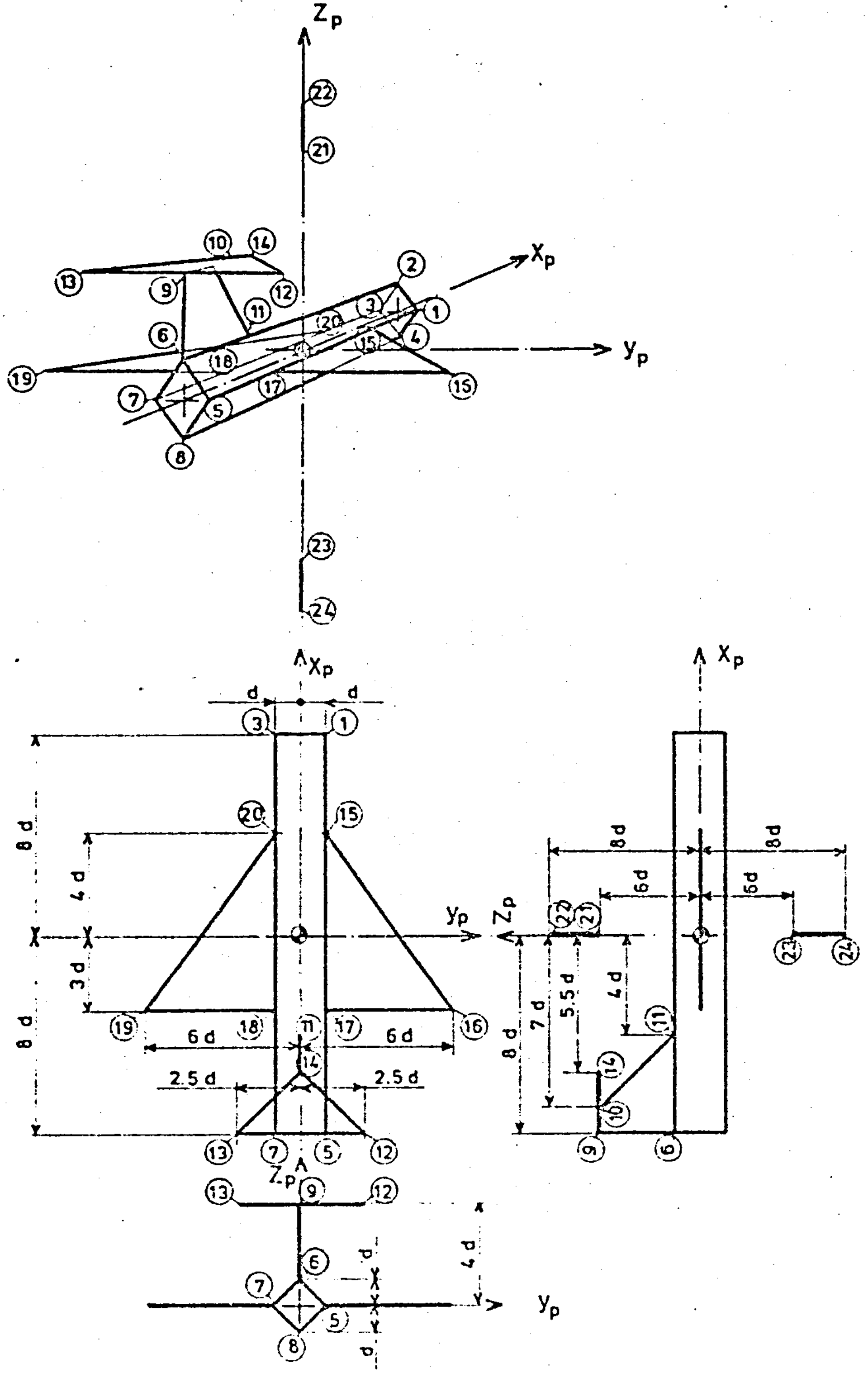

FIGURE 38. BASIC VEHICLE SYMBOL WITH SQUARE FUSELAGE CROSS-SECTION.

ORIGINAL PAGE IS
OF POOR QUALITY

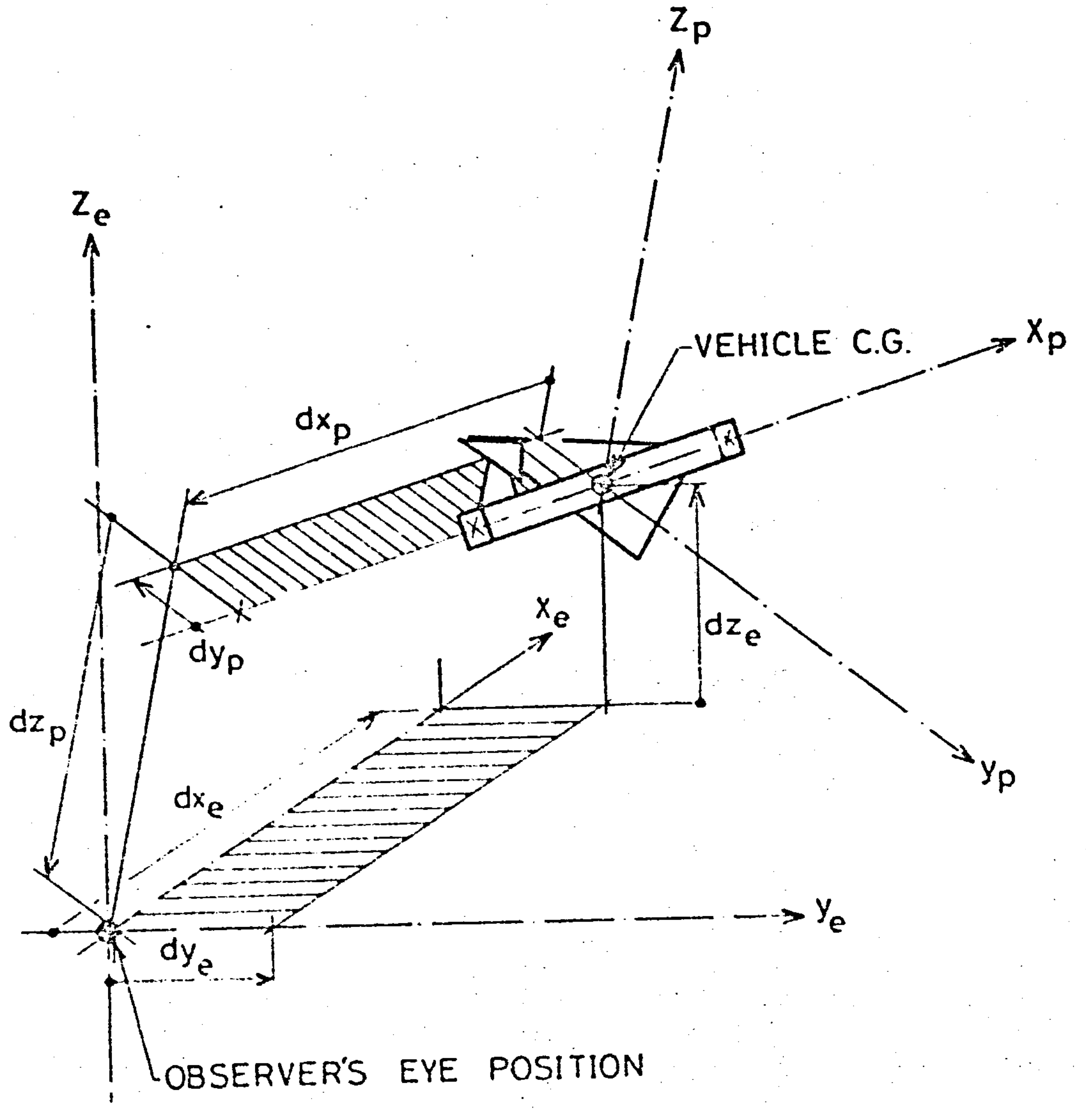

FIGURE 39. Orientation of object coordinate system with respect to eye coordinate system.

ORIGINAL PAGE IS
OF POOR QUALITY

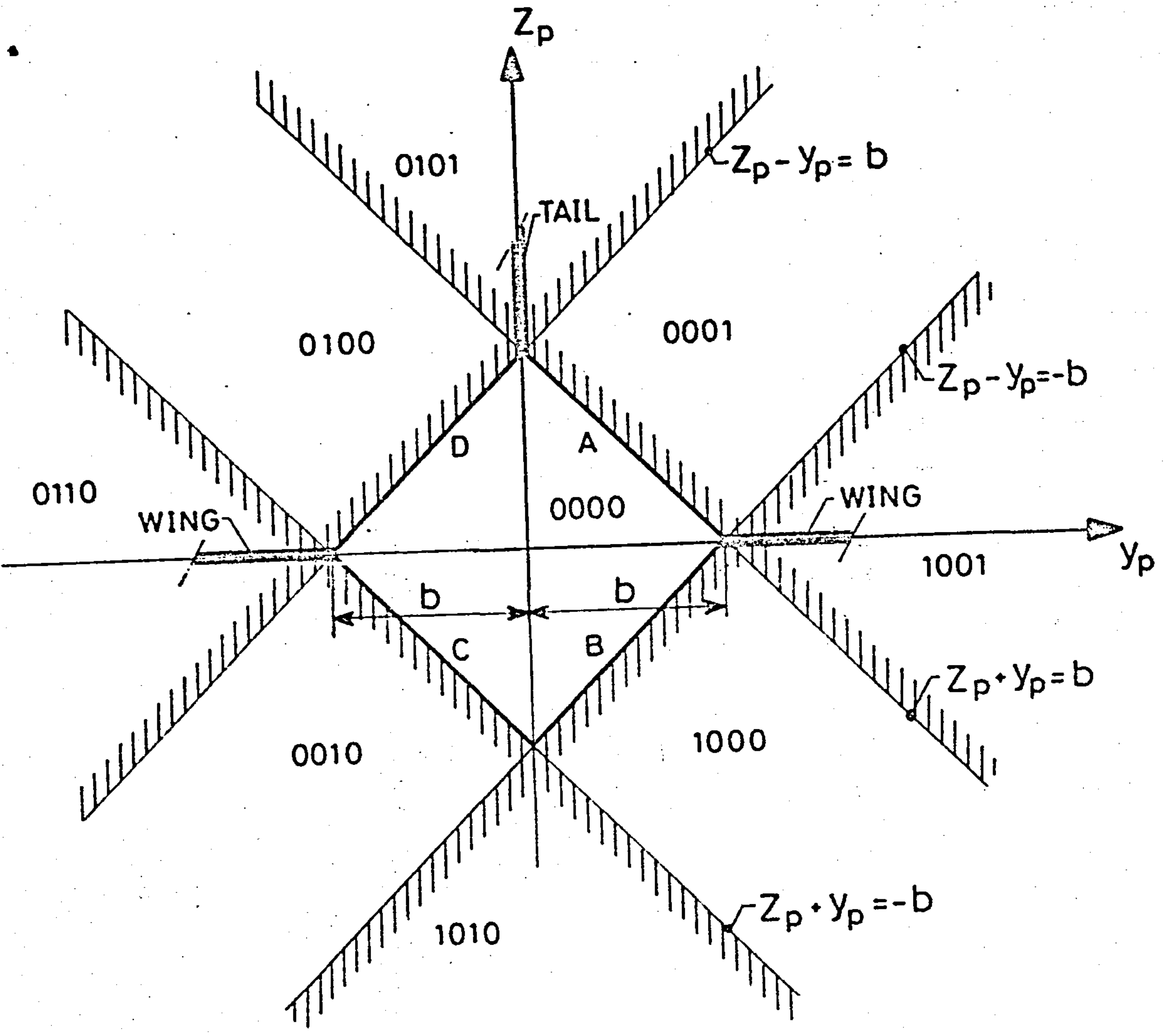

FIGURE 40. Areas in which observer's eye can be located; square fuselage cross-section.

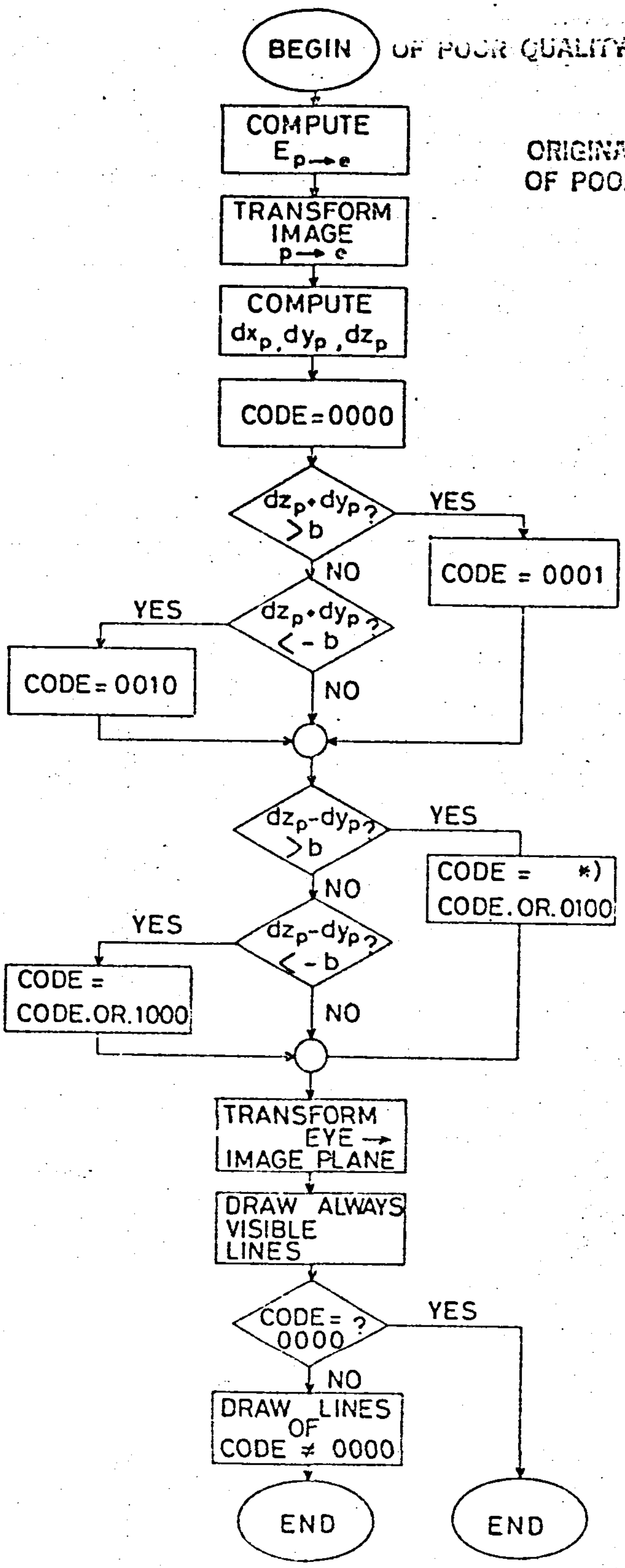

*) BIT-BY-BIT LOGICAL "OR"

FIGURE 41. FLOW CHART OF COMPUTATIONAL METHOD FOR DRAWING PREDICTOR SYMBOL.

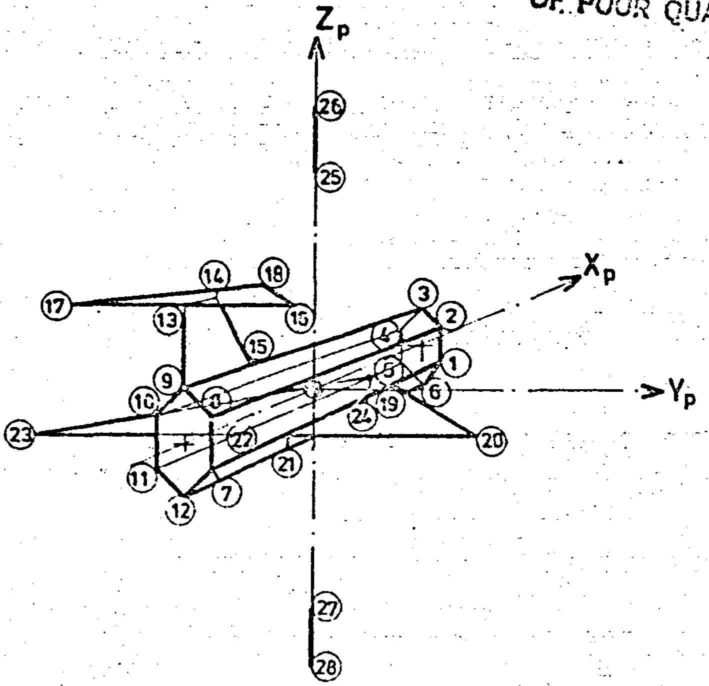
Z_p
26
25
X_p
17
14
18
13
16
3
2
4
15
9
1
5
10
8
19
6
Y_p
23
24
22
20
21
11
7
12
27
28

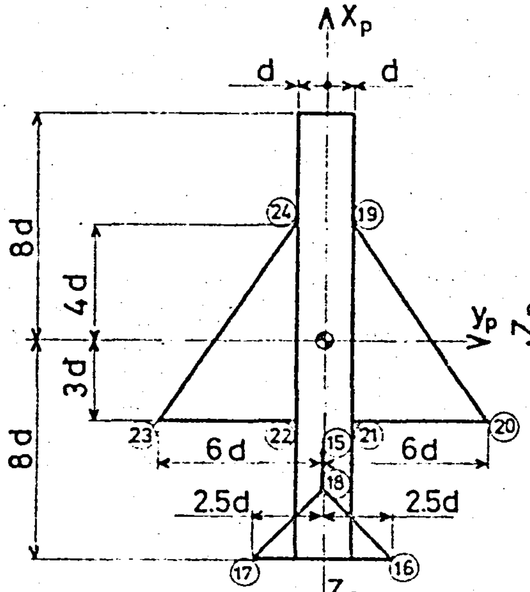
X_p
d
d
8d
4d
3d
8d
24
19
y_p
23
22
15
21
20
6 d
6 d
18
2.5d
2.5d
17
16

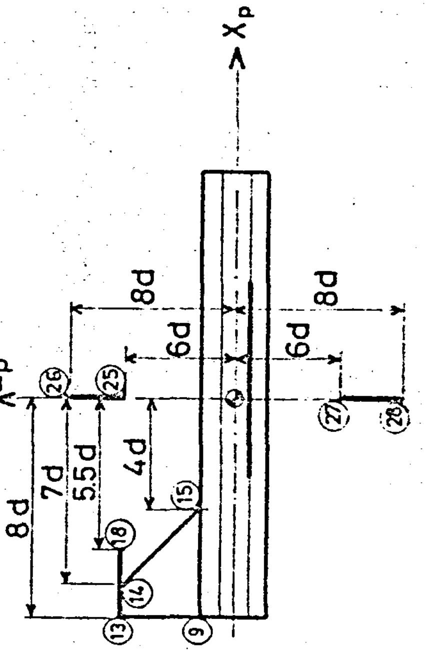
X_p
8d
8d
6d
6d
Z_p
26
25
27
28
8 d
7d
5.5d
4d
15
18
14
13
9

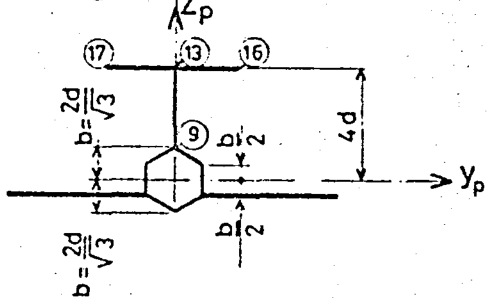
Z_p
17
13
16
b = 2d/√3
9
b/2
4d
y_p
b/2
b = 2d/√3

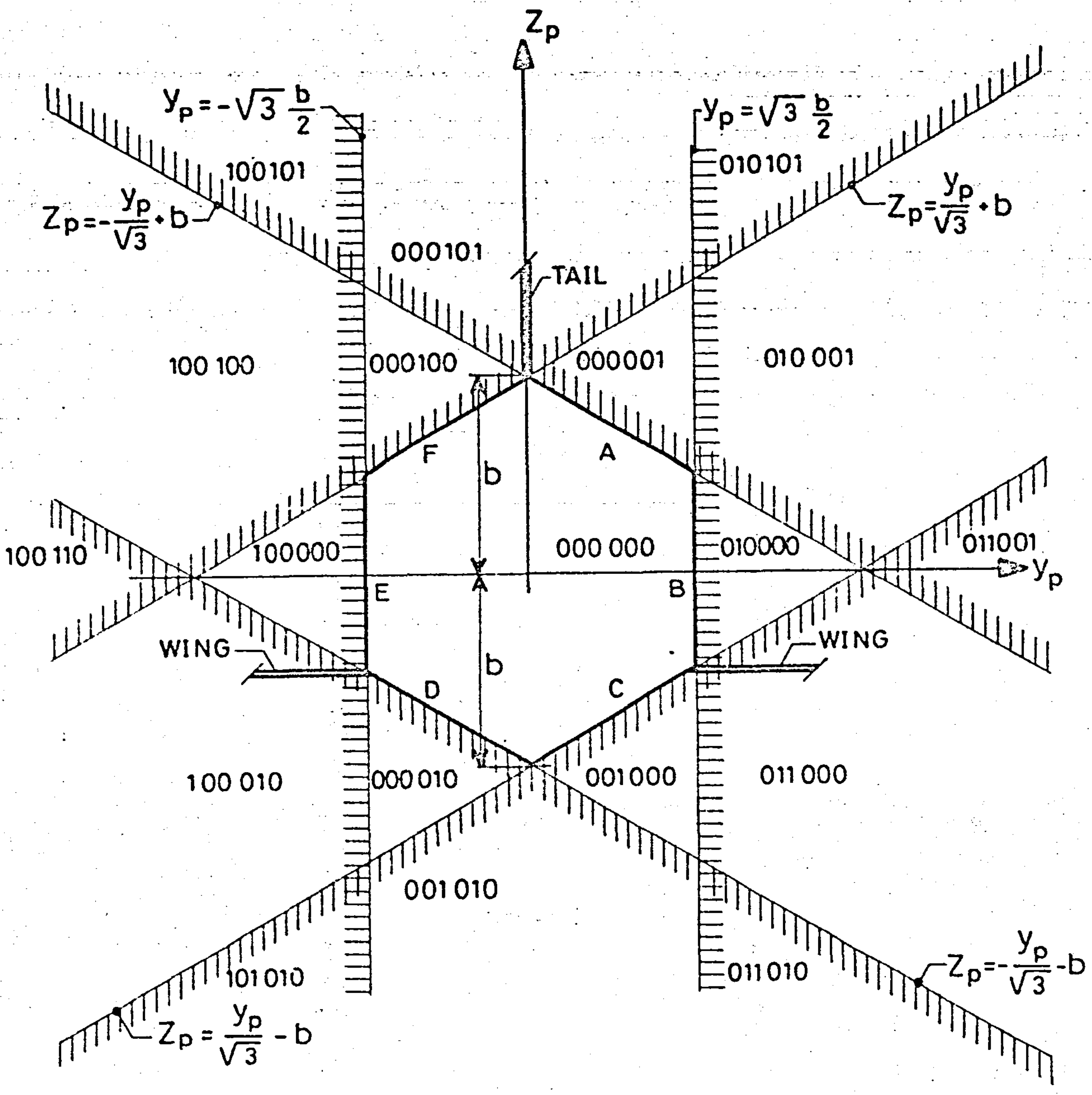

FIGURE 43. Areas in which observer's eye can be located; hexagonal fuselage cross-section.

END

DATE

FILMED

DEC 28 1982